

Electronic Theses and Dissertations, 2004-2019

2013

Peak Power Scaling Of Nanosecond Pulses In Thulium Based Fiber Lasers

Christian Gaida
University of Central Florida

 Part of the [Electromagnetics and Photonics Commons](#), and the [Optics Commons](#)
Find similar works at: <https://stars.library.ucf.edu/etd>
University of Central Florida Libraries <http://library.ucf.edu>

This Masters Thesis (Open Access) is brought to you for free and open access by STARS. It has been accepted for inclusion in Electronic Theses and Dissertations, 2004-2019 by an authorized administrator of STARS. For more information, please contact STARS@ucf.edu.

STARS Citation

Gaida, Christian, "Peak Power Scaling Of Nanosecond Pulses In Thulium Based Fiber Lasers" (2013).
Electronic Theses and Dissertations, 2004-2019. 2977.
<https://stars.library.ucf.edu/etd/2977>

PEAK POWER SCALING OF NANOSECOND PULSES IN THULIUM BASED FIBER
LASERS

by

CHRISTIAN GAIDA
B.S. Friedrich Schiller University Jena, Germany, 2011

A thesis submitted in partial fulfilment of the requirements
for the degree of Master of Optics
in the College of Optics and Photonics
at the University of Central Florida
Orlando, Florida

Summer Term
2013

Major Professor: Lawrence Shah

© 2013 Christian Gaida

ABSTRACT

Thulium based fiber lasers represent a promising alternative for pulse energy scaling and high peak power generation with ytterbium based systems at $1\mu m$. Advantages of thulium arise from the operation at longer wavelengths and a large gain bandwidth (1.8-2.1 μm). Nonlinear effects, such as self phase modulation, stimulated Raman scattering and stimulated Brillouin scattering generally limit peak power scaling in fiber lasers. The longer wavelength of thulium fiber lasers and large mode field areas can significantly increase the nonlinear thresholds. Compared to $1\mu m$ systems, thulium fiber lasers enable single mode guidance for two times larger mode field diameter in step index fibers. Similar behavior is expected for index guiding thulium doped photonic crystal fibers.

In this work a novel thulium doped rod type photonic crystal fiber design with large mode field diameter ($> 50\mu m$) was first characterized in CW-lasing configuration and then utilized as final amplifier in a two stage master oscillator power amplifier. The system generated MW-level peak power at 6.5ns pulse duration and 1kHz repetition rate. This world record performance exemplifies the potential of thulium fiber lasers to supersede ytterbium based systems for very high peak power generation in the future.

As part of this work a computer model for the transient simulation of pulsed amplification in thulium based fiber lasers was developed. The simulations are in good agreement with the experimental results. The computer model can be used for efficient optimization of future thulium based fiber amplifier designs.

ACKNOWLEDGMENTS

I would like to express my sincerest thanks and appreciation to everyone who helped me to accomplish this study.

In particular I want to thank Dr. M. Richardson and Dr. L. Shah for the great opportunity to work in the field of thulium fiber laser development, all the good advice and financial support. I would like to extend my sincerest thanks to Dr. R. Amezcua Correa for all the important discussions about fiber design, fiber cooling and for the help with fiber end facet preparation.

I greatly appreciate the help of Dr. J. Moharam in questions of computer simulation, of Dr. E. v. Stryland, Dr. M. Bass, Dr. A. Schülzgen and Dr. B. Zeldovich for discussions about thulium cross sections, rate equations and time retardation and R. Zotti for building efficient laser cooling parts.

This work would not have been possible without the helpful advice and excellent preliminary work of Dr. Pankaj Kadwani, who developed and optimized the thulium fiber laser, that was used for many experiments in this work. Special thanks goes to C. Jollivet, who conducted important simulation and characterization of the fibers utilized in this work. Furthermore I want to thank Dr. M. Baudalet, N. Bodnar, J. Bradford, A. Chatterton, M. Gebhardt, M. Müller, Dr. A. Sims, A. Sincore, J. Sziliagyi and C. Willis for technical support, proof reading or scientific advice that led to the success of this work. Generally I want to thank all the members of the Laser Plasma Laboratory for helpful advice and sharing experimental equipment.

Many ideas and theoretical advice from the fiber laser group at the Institute of Applied Physics in Jena helped to achieve the experimental and theoretical results in this work. In particular I want to thank Dr. J. Limpert, Dr. C. Jauregui-Misas, F. Stutzki, F. Jansen and H. Otto.

I wish to thank all of the faculty, students and staff for creating a great environment during the time of my study abroad at CREOL, the College of Optics and Photonics, where I have gained valuable knowledge in the field of optics and experimental experience. In this sense, I acknowledge the support of the Atlantis-Master International in Laser, Materials science and Interaction (MILMI) program, that provided the necessary financial support and initiated the joined master program between the Friedrich Schiller University Jena and the University of Central Florida.

Finally, I wish to thank all my friends and family for their ongoing support in my life and career.

TABLE OF CONTENTS

LIST OF FIGURES	ix
LIST OF TABLES	xiv
CHAPTER 1: INTRODUCTION	1
CHAPTER 2: BASICS	4
2.1 Generation and amplification of ns- pulses	5
2.1.1 The laser concept	5
2.1.2 Q-switching	7
2.1.3 Working principle of an acousto-optical modulator	8
2.1.4 Electro-optical modulator for Q-switching	9
2.1.5 Master oscillator power amplifier	10
2.2 Design of optical fibers and mode field scaling	12
2.2.1 Step index fiber	12
2.2.2 Photonic crystal fiber	15
2.2.3 Double clad fibers	18
2.3 Peak power limitations in fiber lasers	19
2.3.1 Self focusing	20
2.3.2 Self phase modulation	21
2.3.3 Four wave mixing	23
2.3.4 Stimulated Raman scattering	25
2.3.5 Stimulated Brillouin scattering	27

2.3.6	Amplified spontaneous emission	29
2.3.7	Optical damage	30
2.3.8	Thermal limitations and waveguide changes	34
2.3.9	Photodarkening	37
2.4	Properties of thulium in silica	37
2.4.1	Energy level structure and pump considerations	38
2.4.2	Cross relaxation and upconversion	41
2.4.3	Rate equations	44
2.4.4	Thermal effects	46
2.5	Advantages of thulium	49
CHAPTER 3: EXPERIMENTS		51
3.1	Thulium doped rod-type PCF	52
3.2	Photodarkening measurement	55
3.3	CW-lasing and ASE	58
3.3.1	Lasing spectra and ASE	60
3.3.2	Lasing slope efficiencies	62
3.3.3	Beam quality	63
3.3.4	Wavelength tuning	64
3.4	CW-amplification	65
3.4.1	Experimental setup	66
3.4.2	Characteristics of the CW-seed source	68
3.4.3	Measurement of the mode field diameter	71
3.4.4	CW-amplification performance	73

3.5	Pulsed amplification	80
3.5.1	Characteristics of the pulsed seed source	81
3.5.2	Amplification to MW-level peak power	84
3.6	Summary of experimental results	88
CHAPTER 4: SIMULATIONS		90
4.1	Outline of the model	91
4.2	Modeling CW-amplification	96
4.3	Temperature in the fiber core	101
4.4	Improved model	108
4.5	Modeling pulsed amplification	112
4.6	Summary of the simulation results	118
CHAPTER 5: SUMMARY AND OUTLOOK		120
LIST OF REFERENCES		123

LIST OF FIGURES

1.1	Peak power evolution over the past 6 years in thulium based fiber lasers with nanosecond pulse duration. [6, 7, 8, 9, 10, 11, 12, 13, 14, 15, 4].	2
2.1	Working principle of CW-lasers [16]	6
2.2	Working principle of Q-switched lasers [16, 17]	7
2.3	Acousto-optical modulator (AOM) for Q-switched operation [16, 17]	8
2.4	Electro optical modulator (EOM) for Q-switched operation [17]	10
2.5	Concept of a MOPA. Isolators prevent feedback to the oscillator or pre-amplifiers	11
2.6	Pulse slicing and picking utilizing an EOM for pulse duration and repetition rate control	11
2.7	Cross section of a SIF (left) and a polarization maintaining SIF (right)	13
2.8	Geometrical beam path in a SIF (side view)	14
2.9	The first PCF with very small air holes in the cladding and a solid core (left); Far-field optical pattern when excited by red and green laser light (right) [29]	15
2.10	Modal sieve concept; different guiding situations of only the fundamental mode (left) and two selected higher order modes (center and right) [29] . . .	16
2.11	Advanced PCF-based fiber designs for MFA scaling: large pitch fiber (left), leakage channel fiber (right)	17
2.12	Index guiding PCF with double clad structure for pump light guidance without (left) and with (right) stress inducing elements.	19
2.13	Spectral broadening by self phase modulation. The dips in the broadened spectrum are caused by interference since all the new frequencies are produced twice at different points in time. [16]	22
2.14	Raman Stokes and Raman anti-Stokes scattering [40]	26

2.15	Summary of reported damage threshold fluences for silica [41]. Large diversity about damage thresholds for ns-pulse durations	32
2.16	Microscope images of damaged fiber facets (NKT Photonics) [48]	34
2.17	Mode field area shrinking due to thermally induced index changes in the waveguide structure of index guiding PCF and LPF [23]	35
2.18	Apparently chaotic power content fluctuations between different modes when a certain average power threshold (in this case 270W) is exceeded [49]	36
2.19	Thulium energy level diagram showing possible pump transitions and important processes for laser emission and energy transfer between two ions [56]. .	39
2.20	Thulium absorption spectrum [57]	40
2.21	Energy transfer between thulium ions for high doping concentrations [56] . .	41
2.22	Temperature dependence of the stimulated emission cross-section in thulium doped silica [63]	48
2.23	The lifetimes for fluorescence of transition ${}^3F_4 \rightarrow {}^3H_6$ of thulium in silica measured for different temperatures [63]	49
3.1	Image of the fiber facet, showing the $80\mu m$ diameter core and part the $220\mu m$ diameter inner cladding.	53
3.2	Theoretical modal analysis performed by Clemence Jollivet, CREOL 2012 [70]	54
3.3	Setup for the measurement of photodarkening in fibers	55
3.4	Image of the fiber end facet at maximum light coupling in the fiber core with and without pinhole (images inverted for better visibility)	56
3.5	Normalized Signal Power divided by HeNe Power	58
3.6	The schematic sketch shows a counter propagating laser cavity. A wedge with 4% reflectivity at $2\mu m$ was used as output coupler. For wavelength tuning the mirror at $2\mu m$ was replaced by a gold reflection grating. The same pump telescope was used for both rods [71].	59
3.7	Spectral analysis of lasing operation and ASE	61
3.8	Slope efficiency for lasing operation and ASE	63

3.9	Investigation of beam quality. Both PCF rods show nearly diffraction limited beam quality	64
3.10	Investigation of the wavelength tunability in rodB	65
3.11	Setups for pulsed and CW-amplification	67
3.12	Schematic Setup of the master oscillator and preamplifier. The AOM can be operated in CW-mode or pulsed mode. The EOM is used as a slicer/ pulse picker and is turned off for CW-operation	69
3.13	CW-performance of the seed system	70
3.14	Self pulsation occurs in master oscillator when AOM is set to CW mode . . .	71
3.15	Measurement of the mode field diameter without amplification	72
3.16	CW-amplification performance of rodB with output powers of $> 18W$	74
3.17	Collimated beam profiles for various output powers. The beam quality fluctuates with changing pump powers.	75
3.18	CW-amplification performance of rodB with output powers of 20W and excellent beam quality [71]	75
3.19	Characterization of rodB as the final amplification stage	76
3.20	Amplification in rodB with more than 250W pump power	77
3.21	Beam profiles for various output powers. The beam quality starts to degrade for output powers $> 30W$ and degrades drastically for output powers $> 40W$	78
3.22	Thermal lensing for output powers $> 20W$	79
3.23	Characteristics of the master oscillator at 670mW average output power and 20kHz repetition rate	82
3.24	EOM utilized as pulse slicer and pulse picker enabling tunability of pulse duration between 6ns-100ns and pulse repetition rates between 1kHz-20kHz.	82
3.25	Characteristics of the flexible PCF output at 250mW average output power and 1kHz repetition rate	83

3.26	Output power over launched pump power for various repetition rates and pulse durations. Also shown are the corresponding slope efficiencies and a beam image at 1kHz, 6.5ns with 7.3W average power [20].	85
3.27	Characteristics of the final amplifier output at 7.3W average output power and 1kHz repetition rate	86
4.1	The fiber is divided into segments with width Δz and the input pump and signal powers in forward and backward direction are propagated to the left and right, respectively, through all L segments at each time step Δt	94
4.2	Schematic summary of the simulation algorithm allowing for transient modeling of pulsed signal and pump input including ASE generation. First the equations for forward and backward propagating pump and signal power are evaluated for each fiber segment of length Δz using equations 4.11 and 4.10. Subsequently the change of population densities is evaluated for a small time step Δt using the rate equations 4.7, 4.6, 4.5.	95
4.3	Simulated signal power evolution with pump power for various seed powers .	96
4.4	Comparison of simulated slope efficiency and gain with experimental results.	97
4.5	Simulated output spectra and signal propagation for 0.2W (blue) and 4W (green) seed signal at 90W pump power	98
4.6	Simulated time evolution of the output signal and pump absorption along the fiber for 0.2W (blue) and 4W (green) seed signal at 90W pump power	99
4.7	Comparison of simulated ASE slope efficiency and spectrum with experimental results	100
4.8	Heat flow mechanisms in an air-clad microstructured active fiber [84]	102
4.9	Radial temperature profile of rodB at 6W seed and 250W pump power. The temperature in the core reaches $\approx 1000K$ when not sufficiently cooled. . . .	106
4.10	Radial temperature profile of rodB at 6W seed and 250W pump power. The temperature in the core is significantly decreased when the cooling conditions are improved.	107
4.11	Radial temperature profile of the fiber tip at 6W seed and 250W pump power for two different cooling conditions.	108

4.12	Emission cross sections at different temperatures calculated with the reciprocity method assuming a temperature independent absorption cross section.	110
4.13	Simulated signal power evolution with pump power for various seed powers including temperature effects in the model.	111
4.14	Comparison of simulated slope efficiency and gain with experimental results including temperature effects in the model.	112
4.15	Simulated stored energy for 10kHz and 1kHz repetition rate at 100W pump power.	113
4.16	Simulated stored energy for 10kHz and 20kHz repetition rate at 100W pump power.	113
4.17	Simulated pulsed average power evolution with pump power for various seed powers, pulse repetition rates and pulse durations.	114
4.18	Simulated maximum peak powers and slope efficiencies	115
4.19	Simulated pulse shape and spectrum at 100W pump power, 1kHz and > 700kW peak power.	116
4.20	Comparison of ASE power and peak power evolution with pump power for different seed conditions.	117
5.1	Peak power evolution over the past 6 years in thulium based fiber lasers with nanosecond pulse duration. In this work MW-level peak power was generated for the first time in thulium based fiber lasers (red marker) [6, 7, 8, 9, 10, 11, 12, 13, 14, 15, 4].	121

LIST OF TABLES

2.1	Radiative decay rates, non-radiative decay rates and cross relaxation upconversion constants [61, 63, 64]	46
3.1	Detailed specifications of the two thulium doped rod-type PCF's	53

CHAPTER 1: INTRODUCTION

Over the last 15 years fiber lasers have experienced an incomparable performance evolution with nowadays more than $10kW$ CW-output power [1] and $\approx 1kW$ average power in pulsed operation [2]. Very high peak powers of more than $4MW$ [3] in the fiber and pulse energies as large as $26mJ$ [4] have been demonstrated for nanosecond pulse durations. All these accomplishments were achieved with ytterbium based fiber laser systems at $1\mu m$ wavelength, which are currently the preferred gain media by virtue of their efficiency [1].

Fiber lasers in general offer excellent beam quality, broad gain linewidth, high gains and efficiencies with often fully fiberized cavities allowing for robust and compact systems. The outstanding thermo-optical properties of fiber lasers are attributed to the large ratio of surface-to-active volume that leads to excellent heat dissipation and very stable beam output [2].

Nonlinear effects, such as self phase modulation, stimulated Raman scattering and stimulated Brillouin scattering limit peak power scaling in fiber lasers. The impressive achievements with ytterbium based fiber lasers primarily result from surmounting nonlinear effects by ultra large mode area fiber designs and from the double clad design that allows coupling and guiding of the pump light in the fiber [2]. Another possibility to increase the nonlinear thresholds is a longer operation wavelength. In fact, a larger operation wavelength has a second advantage. It enables single mode guidance for larger mode field areas and this in turn increases the nonlinear threshold as well.

Thulium as the active dopant in fiber lasers has gained interest in recent years due to the very large gain bandwidth of $\approx 200nm$ and the long operation wavelength at $2\mu m$. To name some examples, the long operation wavelength is of interest for applications in medicine, laser ablation of polymers, light detection and ranging and laser induced breakdown spectroscopy. In addition the long operation wavelength enables the utilization of thulium based fiber lasers for directly pumped

optical parametric oscillators and the realization of high energy mid infrared sources that require high peak power, narrow linewidth pump sources [5].

The main objective of this work is the development of a thulium based fiber laser source with high peak power output and pulse durations in the nanosecond range. Some of the most noticeable achievements in terms of peak power at $2\mu\text{m}$ wavelength over recent years are presented in figure 1.1. Most recently Stutzki et al. reported $> 150\text{kW}$ peak power from a Q-switched oscillator in a thulium doped large pitch fiber with $> 80\mu\text{m}$ core diameter as active medium [4].

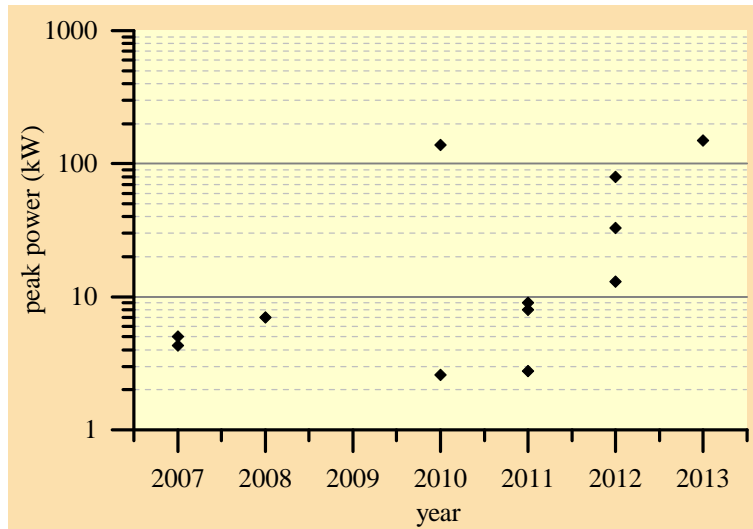


Figure 1.1: Peak power evolution over the past 6 years in thulium based fiber lasers with nanosecond pulse duration. [6, 7, 8, 9, 10, 11, 12, 13, 14, 15, 4].

In this thesis a novel rod-type photonic crystal fiber design is first characterized in CW-lasing configuration and then implemented as final amplification stage in a master oscillator power amplifier system. The work is structured into 4 subsequent chapters. In the beginning the basic concepts of laser engineering, fiber design, peak power limitations in fiber lasers and the properties of thulium doped silica are reviewed. The covered concepts represent the foundation for the experiential and theoretical part of this work. Subsequently the experimental results of a detailed analysis

and characterization of the thulium doped photonic crystal fiber design in lasing and amplification configuration are presented and discussed. The theoretical part of this work deals with the development of a transient simulation tool, that is then utilized for modeling of continuous wave and pulsed amplification. Finally a summary of the presented work and an outlook about possible future perspectives for peak power scaling in thulium based fiber lasers are provided.

CHAPTER 2: BASICS

This chapter reviews basic concepts of general laser engineering, fiber design and nonlinear effects in fiber lasers. The high peak power generation experiments conducted in this work are based on a Q-switched thulium fiber laser with two subsequent amplification stages. The basic concepts of Q-switching for the generation of ns-pulses, as well as the concept of a master oscillator power amplifier are presented in section 2.1.

The laser system in this work utilizes different fiber types, namely a step index fiber as gain medium in the Q-switched oscillator, a flexible photonic crystal fiber as first amplification stage and a rod type photonic crystal fiber as final amplifier. The fundamental guiding concepts in these different fiber designs are summarized in section 2.2. One major challenge of fiber design is the increase of core and mode field area while maintaining single mode guiding. Large mode field diameter are advantageous for peak power scaling in fiber lasers, especially in the final amplification stage, where the highest peak powers are generated. Possible strategies for mode area scaling are additionally discussed in this section.

Section 2.3 addresses common peak power limitations in fiber lasers. It is of outermost importance to know and understand the manifestations of nonlinear effects, e.g. self phase modulation, stimulated Raman- and Brillouin scattering, in order to identify them in the laboratory. Moreover optical fiber damage is a serious threat at the peak powers generated in this work. The experimental reports on fiber damage thresholds are diverse and it is relatively hard to pronounce a general threshold definition. Nevertheless, in this section a short summary of recent experiments is provided and a damage threshold definition is formulated. Not to forget, thermal effects are detrimental for fiber efficiency and an even more serious issue in thulium based fiber lasers that in some cases suffer from a relatively high quantum defect. High temperature gradients can cause mode field shrinking

that is caused by thermally induced waveguide changes. Other mechanisms cause mode instability of the fiber output when a certain threshold average power is exceeded. The thermal load in the fiber has additional effects on emission and absorption processes, decay rates and population of the energy level manifolds. The discussion of these effects is fundamental for the improved simulation model presented at the end of this work and are specifically discussed for thulium doped silica in the final section 2.4.

The final section 2.4 provides specific information about the energy level structure of thulium doped silica, cross relaxation and upconversion effects and presents the rate equations for the selected pumping scheme. Good theoretical insight of the laser and amplification process is necessary in order to understand the physical processes that lead to e.g. The laser efficiency in the experiment. In addition this section provides the underlying theory for the transient simulation of pulsed amplification that is presented in chapter 4. The main focus is set on understanding the cross relaxation and energy upconversion processes and the dependence of decay rates and cross sections on temperature.

2.1 Generation and amplification of ns- pulses

2.1.1 The laser concept

A simple laser consists of at least three parts, namely the resonator, the active medium and an energy source, as shown in figure 2.1a. The pump light absorption increases the number of ions in the upper laser level (excited state) of the active medium. Thus, the pump energy is temporarily stored in the active medium before it is extracted by non-radiative decay, spontaneous emission or the photon field (Φ - number of photons) in the cavity via stimulated emission. Inversion (N) is achieved, when the upper laser level becomes more populated than the ground state. Hereby the

upper energy level lifetime determines the non-radiative decay rate and consequently the required pump rate to achieve inversion. When inversion is reached stimulated emission becomes dominant over absorption and a photon field in the cavity can experience amplification, while the properties of the already existing photons (e.g. wavelength, phase, direction), are exactly copied by the additional photons.

Feedback is required in order to achieve lasing and is provided by the resonator. The lasing condition is reached when the gain through stimulated emission exceeds the losses per cycle in the cavity. The inversion needed to reach this gain level is defined as the threshold inversion N_{th} , that corresponds to a specific threshold pump power P_{th} . For pump powers beyond the threshold, the inversion is not increased further in continuous wave (CW-) laser operation. The additional pump energy is added to the photon field in the cavity and increases the laser output power, as shown in figure 2.1b [16].

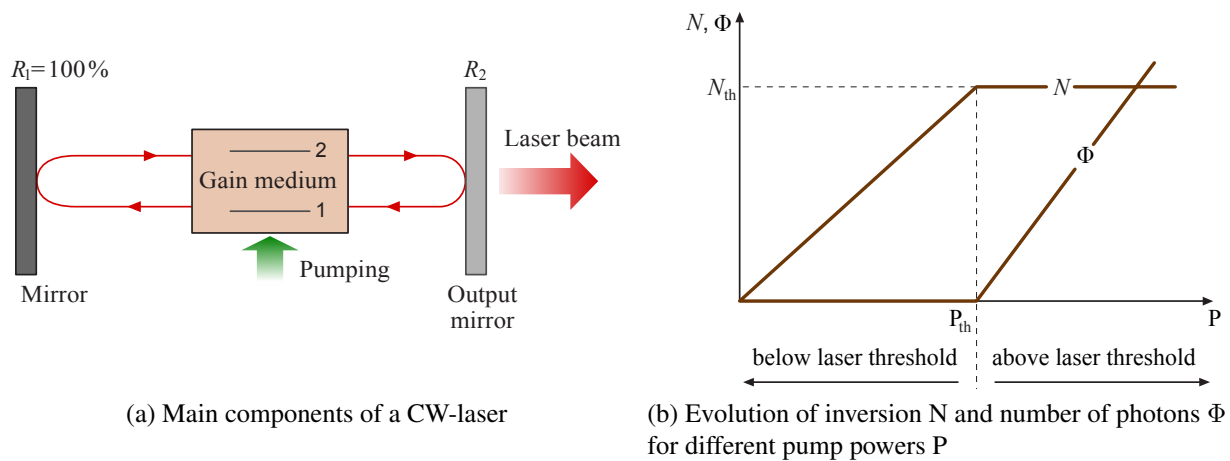


Figure 2.1: Working principle of CW-lasers [16]

2.1.2 Q-switching

A common technique for the generation of high energy pulses is the Q-switching of a laser system with pulse durations ranging from 100ps to ms. The quality factor Q is defined as the ratio of the energy stored in the cavity to the energy loss per cycle. If the loss in the cavity is low, the quality factor is high and vice versa [17].

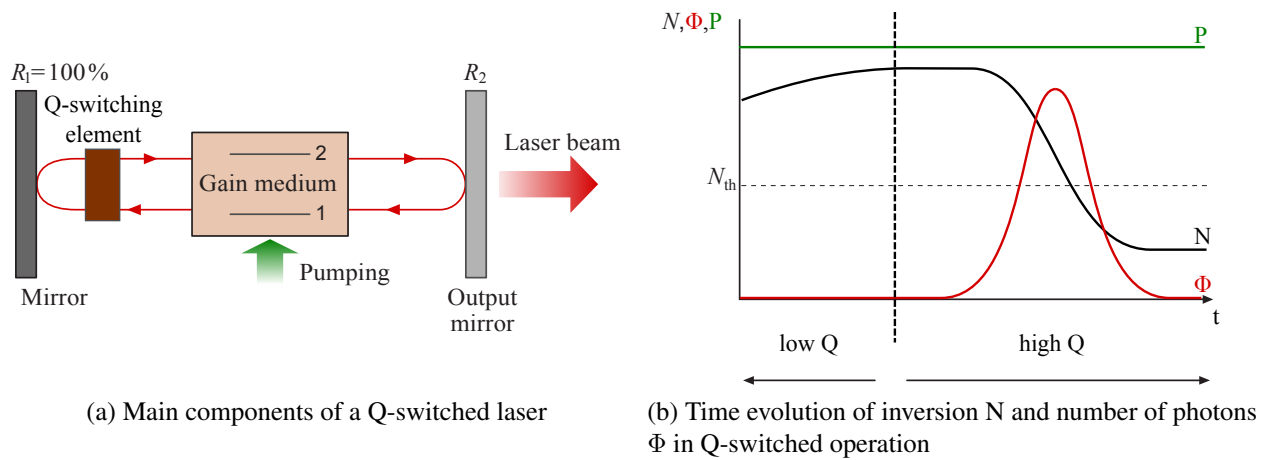


Figure 2.2: Working principle of Q-switched lasers [16, 17]

The idea is based on the temporal control of the losses by a Q-switching element that is added to the cavity as schematically shown in figure 2.2a. Active elements for Q-switching are for example acousto-optical modulators (AOM), electro-optical modulators (EOM) or mechanical switches [17]. Passive Q-switching can be realized by saturable absorbers or saturable absorber mirrors [17]. Figure 2.2b depicts the temporal evolution of the inversion N and the number of photons Φ for low Q (high loss) and high Q (low loss). When the losses are high, the laser threshold is strongly increased and more inversion is required before lasing occurs. As a result, much more energy is temporally stored than in high Q operation. The maximum amount of stored energy is ultimately given by the upper state life time of the laser medium. When the losses are abruptly

reduced, the laser exhibits a gain that greatly exceeds the loss in the cavity and an intense, short laser pulse can be generated during a single round trip in the cavity. The pulse duration depends on the photon cavity lifetime and its minimum is ultimately set by the cavity length.

2.1.3 Working principle of an acousto-optical modulator

An acousto-optical modulator (AOM) exploits the modification of the refractive index by the oscillating mechanical pressure of a sound wave [18]. The modulator, as shown in figure 2.3a, consists of a transparent block of material attached on one side to a piezo-electric transducer and to an acousto-optic absorber on the other side[16]. The transducer produces traveling sound waves in the material. The photo-elastic effect causes local changes of the refractive index in the material. The periodic refractive index modulation induced by the sound wave forms a Bragg grating which is used to diffract the beam.

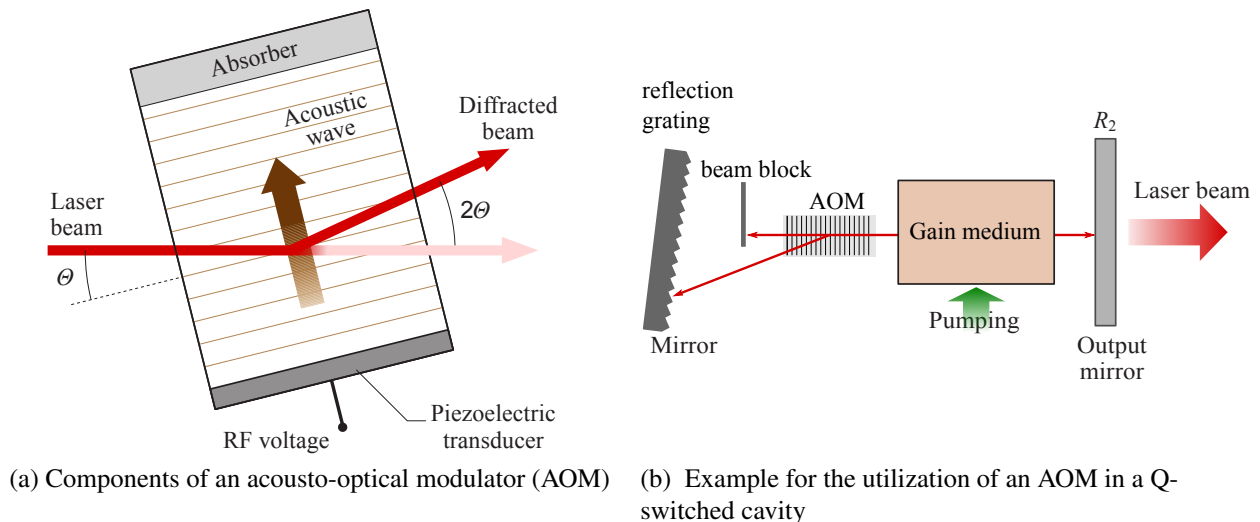


Figure 2.3: Acousto-optical modulator (AOM) for Q-switched operation [16, 17]

The acousto-optic modulator may be implemented as a Q-switch in a high gain system by blocking the zero order in the cavity and utilizing the first diffraction order to form the cavity, as shown in figure 2.3b. A reflection grating may be used for wavelength tuning. Whenever there is no grating formed in the AOM, the cavity losses are high, because the zero order is blocked. When the grating is formed, the first diffraction order can oscillate in the cavity and the losses are reduced.

2.1.4 *Electro-optical modulator for Q-switching*

Electro-optical modulators (EOM) can be utilized for the design of very fast and controlled optical switches. The physical effect exploited by such modulators is the Pockels effect in crystals or liquids. When an external electric field is applied to such materials, birefringence is induced. Depending on the applied electric field strength the EOM or Pockels cell may effectively become a $\lambda/4$ - or $\lambda/2$ -plate. Initially linear plane-polarized light at 45° to the fast and slow axes of the crystal can become circular polarized or rotated by 90° . An optical switch can be realized in both cases with slightly different configurations as shown in figure 2.4 [17].

In the first configuration shown in figure 2.4a a voltage $V_{1/4}$ is applied to the Pockels cell and a linearly polarized input beam becomes circular polarized, is then reflected by the rear mirror and passes again through the Pockels cell. As a result the beam experiences a total rotation of 90° and is rejected from the laser cavity by the polarizer (high loss). When the voltage is turned off the beam polarization is not affected (small loss) [17]. In the second arrangement shown in figure 2.4b a voltage $V_{1/2}$ must first be applied to the Pockels cell to achieve low loss in the cavity. In this configuration the Pockels cell is located between two crossed polarizers. When voltage is applied, the beam experiences a 90° rotation for every pass through the Pockels cell and is not rejected by the polarizers. If there is no voltage applied to the Pockels cell, the beam is rejected by the polarizer closest to the rear mirror and the losses in the cavity are high [17].

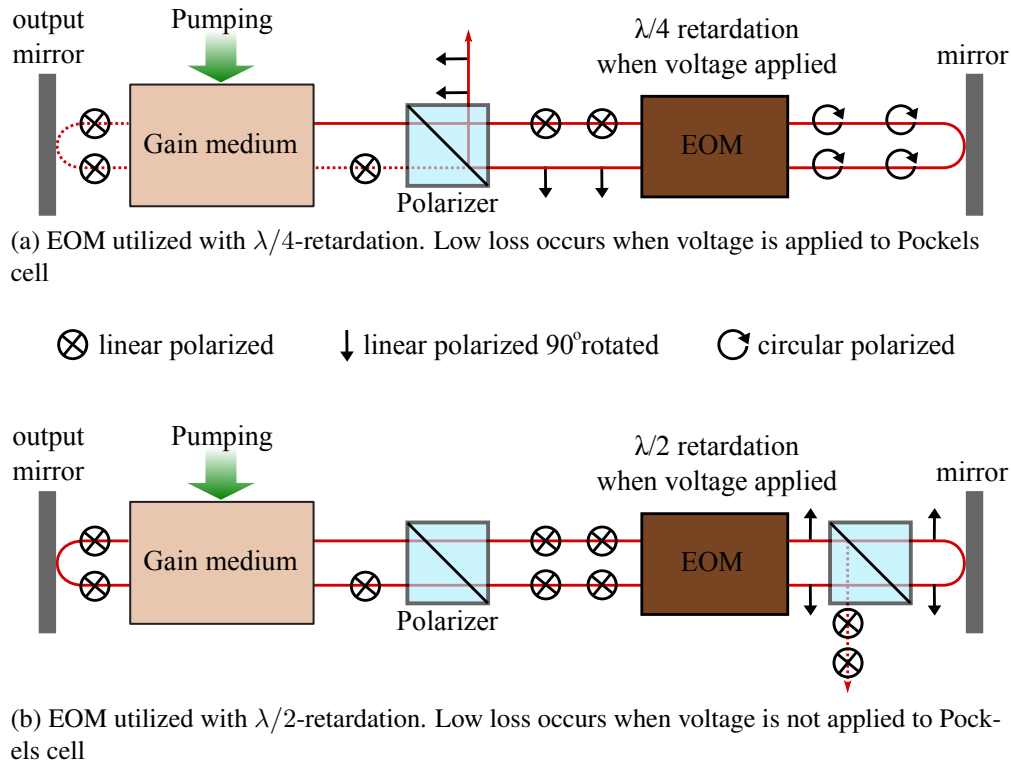


Figure 2.4: Electro optical modulator (EOM) for Q-switched operation [17]

2.1.5 Master oscillator power amplifier

Q-switched laser sources can provide very high energy pulses at relatively short pulse durations. However, a major limitation of Q-switched fiber lasers is often the long pulse duration in the order of 100ns due to the long cavity length. Shorter cavities can be achieved by implementing shorter rod type fibers with enhanced energy storage per length. Very short pulse durations and fiber lengths can be achieved using heavy doped fibers and core pumping. Nevertheless pulse durations shorter than 10ns are hard to achieve in Q-switched fiber lasers. Another disadvantage of Q-switched laser sources is that the pulse duration and the pulse repetition rate can not be independently set [19].

In Master Oscillator Power Amplifier (MOPA) sources a seed laser signal produced by a master oscillator is amplified in one or multiple amplification stages as shown in figure 2.5. Such a configuration allows for separate and independent optimization of the pulse duration and repetition rate. Subsequent amplification allows the generation of high energy and high peak power pulses. Of course the master oscillator is not required to be a fiber laser, even though the subsequent amplification takes place in fiber amplifiers (Master Oscillator Fiber Amplifier, MOFA). Often times fiber coupled semiconductor lasers are used as master oscillators. These lasers have the advantage of active control on the pulse format, including continuous and independent adjustability of pulse duration, pulse shape and repetition rate. The drawback of such seed lasers is most commonly a small pulse energy in the nJ range at sub 10ns pulse duration. This requires the following amplification stages to provide a very large gain and limits the optimization of the amplifier system for highest peak power.



Figure 2.5: Concept of a MOPA. Isolators prevent feedback to the oscillator or pre-amplifiers

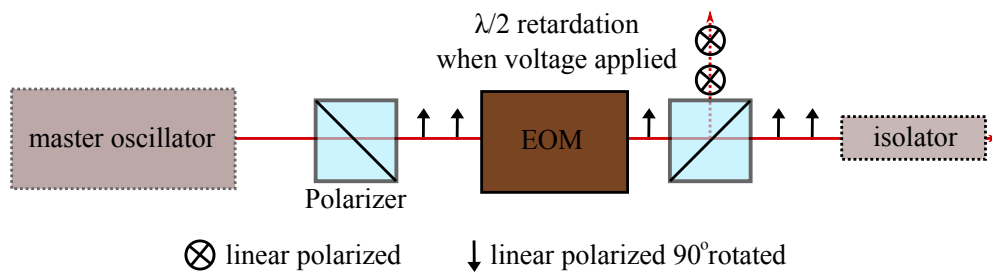


Figure 2.6: Pulse slicing and picking utilizing an EOM for pulse duration and repetition rate control

Another possibility to control pulse duration and repetition rate independent of the oscillator source is the utilization of an EOM as pulse slicer and picker, as shown in figure 2.6. The polarized output of a Q-switched fiber laser source with high energy pulses in the order of $50\mu J$ at 100ns pulse duration can be used as the master oscillator. Sub 10ns pulses with pulse energies in the order of some μJ can be obtained at various repetition rates [20].

2.2 Design of optical fibers and mode field scaling

Optical fibers are wave guiding structures that allow localized and confined light propagation in a particular direction. They are a special case of dielectric waveguides with cylindrical symmetry. Most commonly optical fibers are fabricated from either silica or phosphate-based glass for near infrared wavelengths.

2.2.1 Step index fiber

The simplest optical fiber design is the step index fiber (SIF) with a solid glass core surrounded by a single cladding (Fig. 2.7). The core has a higher refractive index than the cladding and allows for total internal reflection. Mathematically the index structure of a SIF is completely described by $n(r)$ [21].

$$n(r) = \begin{cases} n_{core} & 0 < r \leq a \\ n_{cladding} & a < r \leq a_{cl} \\ n_0 & a_{cl} < r \end{cases} \quad (2.1)$$

The parameters a and a_{cl} represent core and cladding radius, respectively. In most cases $a_{cl} \gg a$

is valid and the boundary of the cladding structure does not affect the guiding properties in the core. An ideal cylindrical optical fiber made of an isotropic material does not show birefringence. Nevertheless mechanical and thermal stress and slight deviations from a perfectly rotational symmetric index distribution cause a small birefringence in a real fiber. Therefore the polarization of an input beam is altered while propagating through the fiber. To prevent this from happening stress rods can be added to the fiber cladding and induce a controlled birefringence. As a result effects due to the inherent small birefringence can be reduced. If the polarization direction of a linear polarized input beam matches the direction of one of the optical axis in the fiber, the polarization of the beam is maintained at the fiber output. Fig. 2.7 shows a polarization maintaining (PM) SIF with the optical axis parallel and vertical to the stress rods [22].

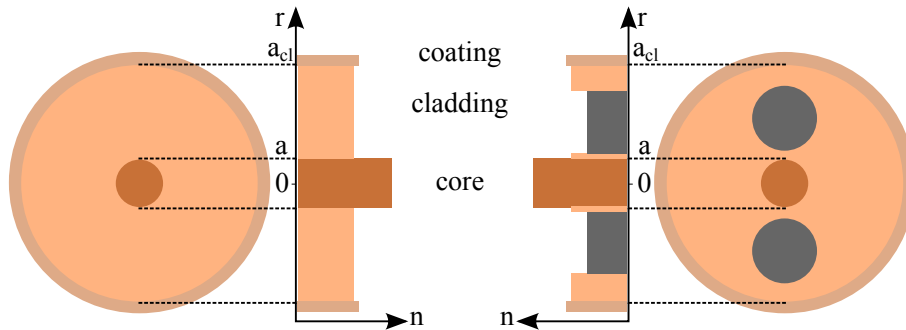


Figure 2.7: Cross section of a SIF (left) and a polarization maintaining SIF (right)

The geometrical beam path with total internal reflection is shown in Fig. 2.8. The maximum angle of the incident beam, that still allows coupling into the fiber, is given by the numerical aperture (NA) of the fiber. Equation 2.2 shows that the acceptance angle ϕ_0 decreases for smaller index differences between core and cladding. Of course the acceptance angle can be made large by increasing the index difference, however the number of guided modes is also influenced by the NA. For step index fibers the well known V-number represents a figure of merit for describing the modal guiding properties and can be evaluated with equation 2.3. Single mode behavior is maintained for $V < 2.405$ [18].

$$NA = \sin(\phi_0) \cdot n_0 = \sqrt{n_{core}^2 - n_{cladding}^2} \quad (2.2)$$

$$V = \frac{2\pi}{\lambda} \cdot a \cdot NA \quad (2.3)$$

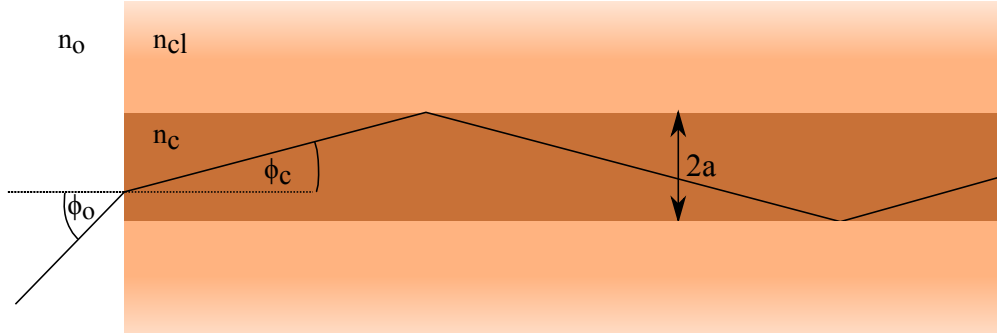


Figure 2.8: Geometrical beam path in a SIF (side view)

In general single mode behavior is desirable for many applications due to the mostly Gaussian like beam qualities. In order to reduce nonlinear effects in fibers, larger core diameters are desirable to reduce the peak intensity while single mode behavior is maintained. The mode field area (MFA) is influenced by the core diameter as well as the NA and corresponds to the area with $1/e^2$ -radius of the intensity for Gaussian beams. A more general expression for the MFA and arbitrary fundamental modes is given by equation 2.4 [23].

$$MFA = \frac{(\int I dA)^2}{\int I^2 dA} \quad (2.4)$$

To compensate for the larger core radius the NA needs to be reduced for a set wavelength in order to maintain single mode operation. Mode area scaling of single mode SIFs is limited to current fabrication technologies (achievable $NA \geq 0.06$) [24]. Consequently the largest possible mode field area (MFA) for such SIFs lies in the order of $200 \mu m^2$ at $1 \mu m$ wavelength. It has been

shown that reasonable single-mode operation can be achieved in fibers that support few modes, if appropriate efforts are made to minimize excitation of higher order modes, e.g. fiber bending and improved coupling, increasing the mode area to roughly $700\mu m^2$ in SIF [25].

2.2.2 Photonic crystal fiber

The idea, that light could be trapped inside a hollow fiber core by creating a periodic lattice of microscopic air holes in the cladding glass, was first proposed in 1991 [26]. All wavelength scale periodic structures exhibit ranges of angle and color where incident light is strongly reflected. In photonic band gap (PBG) materials broad “stop bands” are designed to block propagation of specific wavelengths in every direction [27]. With appropriate design a photonic crystal cladding along the entire length of the fiber can lead to guidance in a hollow core. First attempts of manufacturing such fibers were made in 1995. However, due to manufacturing limits the air holes were too small to create a PBG and guidance in a hollow core would not have been possible and a solid glass core was used instead. This fiber became what is nowadays called a photonic crystal fiber (PCF), although it was initially not clear how light was guided in this fiber [28]. An image of the first photonic crystal fiber (PCF) is shown in figure 2.9.

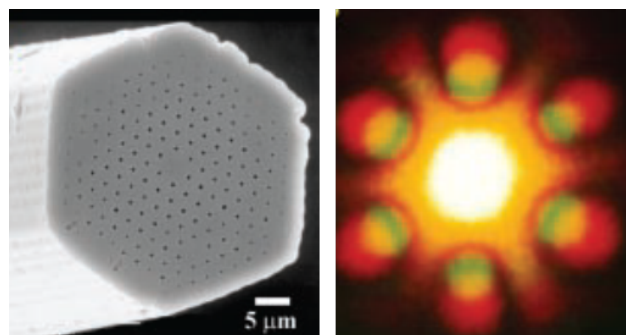


Figure 2.9: The first PCF with very small air holes in the cladding and a solid core (left); Far-field optical pattern when excited by red and green laser light (right) [29]

The intriguing property of this fiber was the single mode behavior for all wavelengths ranging from $458 - 1550nm$. On one hand the guiding mechanism can be understood by the index contrast similar to step index fibers because the effective refractive index in the cladding is lower than in the core due to the air holes. On the other hand there are clear, barrier-free pathways of glass between the air holes along which light could escape from the core. To understand the guiding properties of PCF's in general it is helpful to think of the array of holes as a modal filter or "modal sieve" [28]. In figure 2.10 the schematic cross-section of a PCF is shown for different guiding situations of only the fundamental mode and some selected higher order modes (HOM).

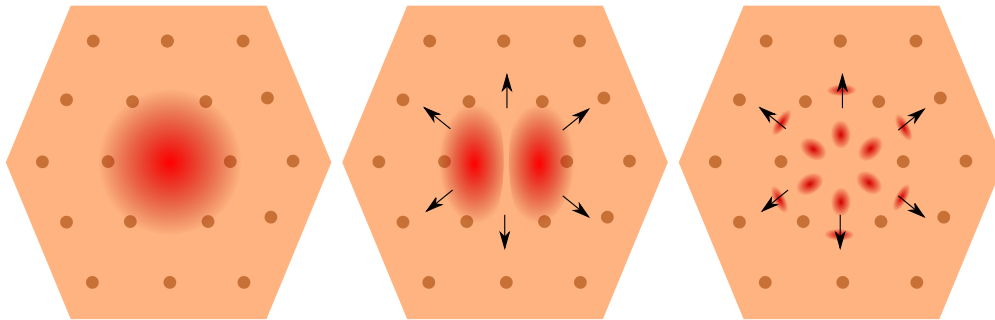


Figure 2.10: Modal sieve concept; different guiding situations of only the fundamental mode (left) and two selected higher order modes (center and right) [29]

Because the refractive index of air is lower than of glass, the light will experience the air hole regions (with diameter d) as a barrier and it will decay evanescently in those regions. However, silica gaps exist between the air holes (spacing Λ between air holes) that allow, under certain circumstances, the light to escape from the core region. The fundamental mode, as shown left in figure 2.10, has only one single lobe and it cannot escape the core region when the spacing Λ between the air holes is too narrow. Higher order modes, as shown in the center and right of figure 2.10, consist of multiple lobes with smaller diameter. Therefore they can slip between the gaps and are not well confined in the core [28]. When the relative hole-size to pitch ration (d/Λ) is increased, more higher order modes are trapped in the core region. For many air holes (small hole size and

small pitch) the guiding behavior becomes very similar to step index fibers and the V-number can be applied as a figure of merit as well. These fibers are often referred to as index guiding PCF's.

One of the major advantages of PCF's in terms of mode area scaling is the design freedom to achieve very small NA and large core diameter while single mode operation is maintained. Nevertheless bending loss becomes a major issue for very large core diameters because small NA's lead to weak guidance in the core. The PCF-rod is a large core fiber design with typically more than 1mm total diameter, which effectively prevents bending. This design enabled large core areas of more than $1000\mu m^2$ at $1\mu m$ wavelength [30].

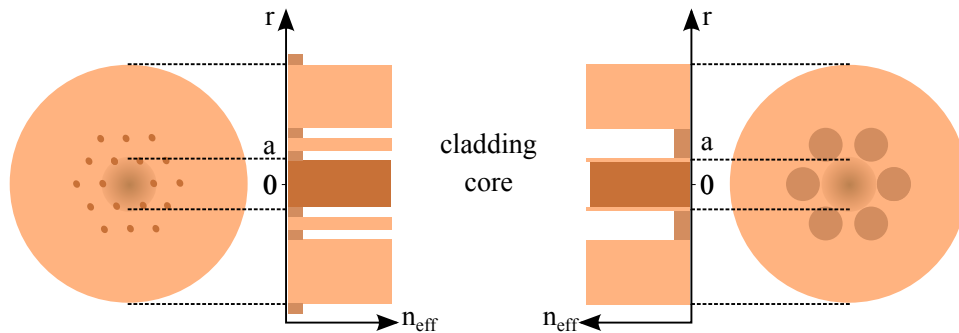


Figure 2.11: Advanced PCF-based fiber designs for MFA scaling: large pitch fiber (left), leakage channel fiber (right)

Another large core area design is the so called leakage channel fiber (LCF) [31]. In contrast to conventional PCF's the first LCF's consisted of only a small ring of very large air holes and accordingly large pitch, as shown in figure 2.11 (right). The basic idea is to introduce more propagation loss to HOM's than to the fundamental mode. The larger mode discrimination of HOM's can lead to effective single mode operation. This concept gives this design a certain bending resistance and enables large core areas while maintaining flexibility of the fiber. Further investigations showed, that designs with two rings of air holes lead to more mode discrimination but at cost of fiber flexibility [32]. To date LCF's reach mode areas of roughly $1500\mu m^2$ when actively doped and more than $8000\mu m^2$ in the passive case.

Significant progress for actively doped fibers was made with so called large pitch fibers (LPF). This fiber design is a PCF with very large pitch between the air holes (distance $\approx 10\lambda$), as shown in figure 2.11(left), and exploits the delocalization of the HOM's [33]. The HOM's experience only little gain compared to the fundamental mode because the overlap with the doped region is small. Furthermore the seed signal in an amplification setup is usually a Gaussian beam. Thus, the power content of HOM's is generally much smaller than the power in the fundamental mode. It is important to understand that the fiber is generally speaking a multimode fiber in the passive case. The very strong preferential gain leads to effective single mode operation with MFA's exceeding $8000\mu m^2$ when actively pumped [33].

2.2.3 Double clad fibers

Fiber amplifiers and lasers are most commonly pumped by diode lasers. Major challenges arise for core pumping schemes because of the small NA and cross section of a single mode fiber. In 1988 Snitzer and collaborators fabricated the first step index double clad fiber [34]. In PCF another ring of air holes surrounding the inner core-cladding structure is added, as shown in figure 2.12. The pump light can easily be coupled into the inner cladding (pump cladding) with much higher NA and cross section than the signal core. All pump rays eventually intersect the doped core region and can be absorbed. However, for radial symmetry, helical or spiral pump modes may not intersect the signal core. In order to achieve best pump absorption asymmetric or non circular (e.g. hexagonal) inner cladding structures can be used. Another way to achieve strong pump absorption is to place the signal core off center. It is clear that the pump absorption over propagation length strongly depends on the overlap of doped core area and cladding area (A_c/A_{cl}). However, decreasing the cladding area reduces the maximum amount of pump light coupled and increasing the core area eventually leads to guidance of HOM's. In conclusion the double clad design allows for the conversion of high power, low beam quality diode laser outputs, to a lower

power, but diffraction limited beam quality. Because of this specific quality fiber lasers are often termed “brightness converters” [22].

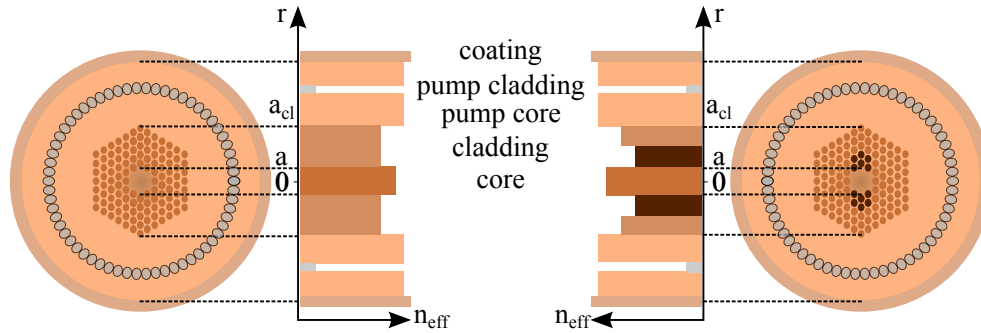


Figure 2.12: Index guiding PCF with double clad structure for pump light guidance without (left) and with (right) stress inducing elements.

2.3 Peak power limitations in fiber lasers

Active fibers as gain media are very attractive for high power lasers mainly due to their outstanding beam quality and their excellent thermal properties. The very good heat dissipation from the active region arises from the effective length of the fiber. In addition fiber lasers combine high efficiencies mainly due to efficient pump absorption (double clad design) and good confinement. However, the fiber geometry itself promotes nonlinear effects, because the light propagates under tight confinement over considerably long distance. In the following paragraphs the most limiting nonlinear effects for peak power and pulse energy scaling are discussed. The lowest order nonlinear effects can be divided into those related to an intensity-dependent refractive index (self focusing, self phase modulation, four wave mixing) and those resulting from stimulated inelastic scattering (stimulated Raman and Brillouin scattering) [35]. Amplified spontaneous emission limits the extractable energy in fiber amplifier, especially when operated at low pulse repetition rates. Moreover a very important constraint for peak power scaling in fiber lasers is the optical damage

threshold of the fiber host material, e.g. the fiber end facet [22]. Furthermore photodarkening and thermal effects are shortly discussed, since they may reduce the efficiency or beam quality of a fiber laser.

2.3.1 Self focusing

Self focusing can occur when very intense light with Gaussian like beam profile passes through a medium. It is a consequence of the nonlinear phase shift that occurs for high intensities and can be described as a $\chi^{(3)}$ nonlinear self effect. The process is always phase matched, because it is a self effect. Equation 2.5 shows the reduced wave equation related to this process for linear polarized light in x direction [36]. As a result we find an intensity dependent refractive index (Equation 2.8) [37].

$$\frac{\partial E_x(\omega)}{\partial z} = \frac{i3\mu_0 c\omega}{8n} \chi_{xxxx}^{(3)}(\omega, \omega, -\omega, \omega) |E_x(\omega)|^2 E_x(\omega) \quad (2.5)$$

$$E_x(\omega) = U_x(\omega, z) \exp(i\phi(z)) \quad (2.6)$$

$$\frac{\partial \phi(z)}{\partial z} = \frac{3\omega}{8nc} \Re [\chi^{(3)}] U_x^2 = k_0 \Delta n \quad (2.7)$$

Using $2I(r) = \epsilon_0 n c U_x^2(r)$ the total refractive index can be expressed as:

$$n(r) = n_0 + \Delta n = n_0 + n_2 I(r) \quad (2.8)$$

If the spatial intensity distribution was Gaussian, the beam would experience a larger nonlinear phase shift in the center than at the wings causing the beam to focus or defocus depending on the sign of n_2 . Interestingly the self focusing threshold does not depend on the peak intensity but on

the peak power. The critical power is given by [19]:

$$P_{cr} \cong \frac{\lambda^2}{2\pi n n_2} \quad (2.9)$$

Assuming linear polarized light the critical power in fused silica is reached at 4MW for $1\mu\text{m}$ and 16MW for $2\mu\text{m}$ wavelength [37].

2.3.2 Self phase modulation

Self phase modulation (SPM) is an effect often encountered when propagating intense light pulses through a nonlinear responsive material and leads to spectral broadening or narrowing. Although the nonlinear refractive index in fused silica is small ($\cong 3.2 \cdot 10^{-20} \text{m}^2/\text{W}$), intense light propagation through fibers is prone to this effect because of the long propagation distance. It can be considered the temporal analog of self focusing as discussed in the previous paragraph. The total phase of an electromagnetic light wave and its first derivative can be written as [37]:

$$\phi(z, t) = k_0 n z - \omega t + k_0 n_2 I(t) z \quad (2.10)$$

$$\frac{\partial \phi(t)}{\partial t} = -\omega + k_0 n_2 z \frac{\partial I(t)}{\partial t} = -(\omega + \delta\omega) \quad (2.11)$$

The temporal nonlinear phase shift causes the light frequency to increase at the frontside and to decrease at the backside of the pulse, as shown in figure 2.13a. For an initially positively chirped pulse (higher frequencies at frontside and lower frequencies at backside of the pulse) this leads to broadening of the spectrum when the intensity is increased, as depicted in figure 2.13b. The dips in the spectrum are caused by interference of the same frequency components that are produced on each side of the pulse. Depending on the temporal delay, the frequency components interfere constructively or destructively. The number of observed spectral peaks M is related to the

maximum phase shift Φ_{max} (equations 2.12 and 2.13) that is anti-proportional to the effective beam area (equation 2.4) and proportional to the fiber length (equation 2.14) [38]. Therefore shorter fiber length and large MFA's are of advantage for the suppression of SPM in fiber lasers and amplifiers.

$$\Phi_{max} = \left(M - \frac{1}{2} \right) \pi \quad (2.12)$$

$$\Phi_{max} = \left(\frac{2\pi}{\lambda} \right) \left(\frac{n_2}{A_{eff}} \right) L_{eff} P_0 \quad (2.13)$$

$$L_{eff} = \frac{1 - e^{-\alpha L}}{\alpha} \quad (2.14)$$

SPM by itself only affects the spectrum of a pulse. However, in combination with group velocity dispersion (GVD) induced chirp effects the pulse shape can be distorted. If this distortion becomes severe it might cause pulse breaking in the time domain [18].

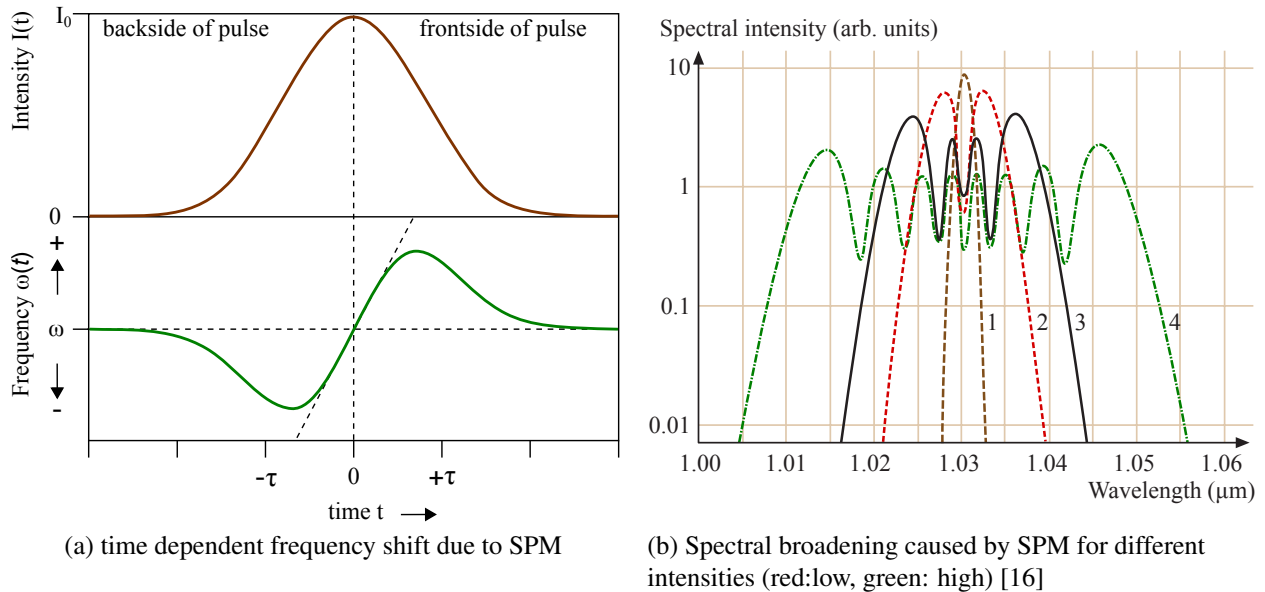


Figure 2.13: Spectral broadening by self phase modulation. The dips in the broadened spectrum are caused by interference since all the new frequencies are produced twice at different points in time. [16]

2.3.3 Four wave mixing

Four wave mixing (FWM) is a third order nonlinear process where energy transfer can occur between four distinguishable beams (E_1, E_2, E_3, E_4). Equation 2.15 includes all relevant terms for this process in the third order nonlinear polarization [36].

$$P^{NL} = \frac{\epsilon_0}{4} \chi_{xxxx} [6E_1^* E_2^* E_3 + 6E_1 E_2^* E_3^* + 6E_1^* E_2 E_3^*] + c.c. \quad (2.15)$$

For simplification only the first term ($6E_1^* E_2^* E_3$) will be discussed in the following. In general FWM only occurs when photons from one or more waves are annihilated and new photons are created at different frequencies while energy and momentum conservation is satisfied. In mathematical terms (ω -frequency, k -wave vector):

$$\omega_1 + \omega_2 = \omega_3 + \omega_4 \quad (2.16)$$

$$k_1 + k_2 = k_3 + k_4 \quad (2.17)$$

In most cases it is difficult to satisfy the above phase-matching condition in optical fibers. However, in the case of $\omega_p = \omega_1 = \omega_2$, where two pump photons ω_p are annihilated and two photons at ω_3 and ω_4 are created, it is relatively easy to achieve phase matching. This specific degenerate case is most relevant for optical fibers and it has similar similarities to stimulated Raman scattering (SRS) [37]. Two sidebands with a frequency shift of $\Omega = \omega_1 - \omega_3 = \omega_4 - \omega_1$ (assuming $\omega_4 > \omega_3$) are formed and are also referred to as Stokes and anti-Stokes bands in analogy to SRS (section 2.3.4).

There are different physical mechanisms in optical fibers that can lead to fulfillment of the phase matching condition. The major contributors (equations 2.18-2.20) are material dispersion Δk_M , waveguide dispersion Δk_W (only in multimode fibers or single mode fibers with large NA) and

nonlinear effects Δk_{NL} (e.g. self or cross phase modulation). In order to realize phase matching one of these contributors needs to be negative.

$$\Delta k_M = \frac{1}{c}[n_3\omega_3 + n_4\omega_4 - 2n_p\omega_p] \quad (2.18)$$

$$\Delta k_W = \frac{1}{c}[\Delta n_3\omega_3 + \Delta n_4\omega_4 - 2\Delta n_p\omega_p] \quad (2.19)$$

$$\Delta k_{NL} = \frac{2n_2\omega}{cA_{eff}}P \quad (2.20)$$

Phase matching can be achieved in birefringent fibers when the nonlinear pump beam is polarized along the slow axis, that is $\Delta k_W < 0$. In multimode fibers it is possible to phase match when the wave guiding contribution Δk_W is negative and cancels $\Delta k_M + \Delta k_{NL}$. In single mode fibers Δk_W is zero and phase matching can only be achieved when $\Delta k_M < 0$ is fulfilled, since the nonlinear refractive index in silica is positive and leads to $\Delta k_{NL} > 0$ [37]. In general this is only possible when the optical fiber shows anomalous dispersion at the nonlinear signal wavelength. At $2\mu m$ wavelength silica fibers are anomalous and FWM can occur due to the interplay of dispersion, self- and cross-phase modulation. Consequently FWM can be of importance for thulium based fiber lasers and amplifiers. The influence of FWM on the amplifier performance becomes enhanced when a fraction of the main beam power is distributed over secondary, closely spaced spectral components, such as multiple longitudinal modes. FWM side bands can become effectively seeded and might set in at much lower peak powers, especially if the initial spectral features are separated by few tens of gigahertz or less [19].

It is worth mentioning that the Stokes peak is usually stronger than the anti-Stokes although in FWM there is no preferred gain for either line. However, often there is an interplay between FWM and stimulated Raman scattering leading to preferred gain of the Stokes line. For highly nonlinear cases the Stokes line becomes as intense as the pump line itself and creates a new shifted line, which then can again produce a new line if the pump power is sufficient. This cascaded FWM

assisted stimulated Raman scattering in combination with self- and cross-phase modulation can be utilized to generate super continua [37].

2.3.4 Stimulated Raman scattering

Spontaneous Raman scattering is a process where one nonlinear signal photon is converted into one lower energy or higher energy Raman photon while the energy difference is either carried away or provided by an optical phonon (lattice vibration). Conversion to a higher or lower energy Raman photon is called anti-Stokes or Stokes process, respectively (see figure 2.14a). The anti-Stokes process is usually orders of magnitude weaker than the Stokes process, particularly at low temperatures. However, strong anti-Stokes light can emerge from four wave mixing if that process is phase-matched (as discussed in section 2.3.3). For intense signal fields and long interaction lengths the spontaneously generated Raman light can act as a seed and amplification can lead to nearly full depletion of the signal beam. This process is called stimulated Raman scattering (SRS).

For CW-operation and pulsed operation with pulse durations greater than 1ns the initial growth of the Raman wave $I_r(\omega_s)$ and depletion of the signal wave $I_s(\omega_s)$ can be described by [37]:

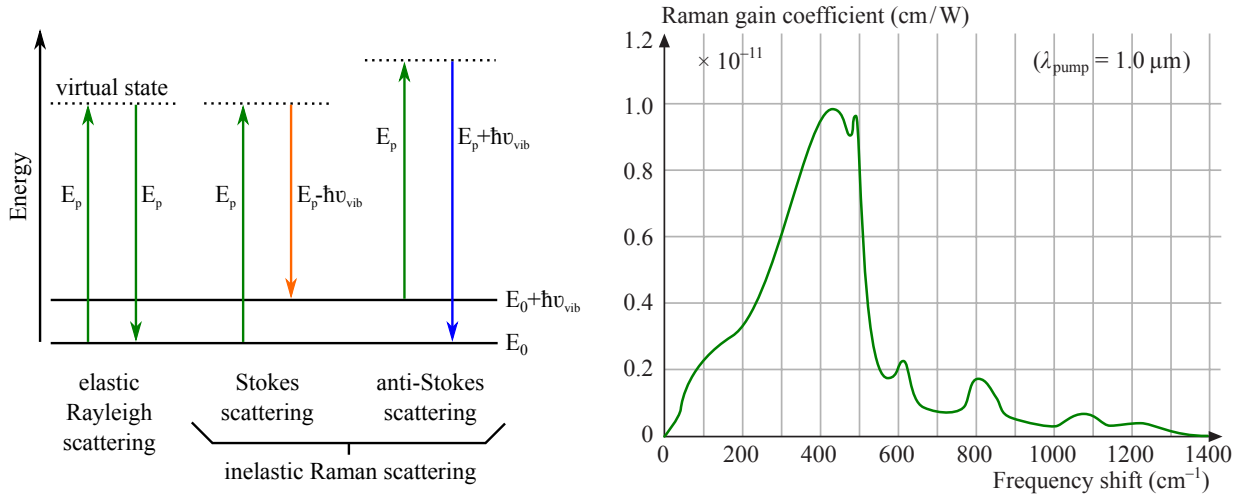
$$\frac{dI_r}{dz} = g_R I_s I_r - \alpha_r I_r \quad (2.21)$$

$$\frac{dI_s}{dz} = -\frac{\omega_s}{\omega_r} g_R I_r I_s - \alpha_s I_s \quad (2.22)$$

Losses of the Raman and signal wave are included by α_s and α_r , respectively, and g_R (inverse proportional to the pump wavelength [37]) describes the Raman gain. The Raman gain spectrum depends on the fiber core and varies with the use of different dopants and host materials. An example of a gain spectrum in fused silica at $1\mu m$ wavelength is depicted in figure 2.14b. Solving the set of coupled differential Equations gives [37]:

$$I_r(L) = I_r(0) \exp(g_R I_0 L_{eff} - \alpha_r L) \quad (2.23)$$

$$L_{eff} = \frac{[1 - \exp(-\alpha_s L)]}{\alpha_s} \quad (2.24)$$



(a) Jablonski diagram representing quantum energy transitions for elastic Rayleigh and inelastic Raman scattering

(b) Raman gain spectrum for fused silica and $1\mu\text{m}$ pump wavelength [39]

Figure 2.14: Raman Stokes and Raman anti-Stokes scattering [40]

The spontaneous scattering process along the fiber and amplification is similar to injection of a seed photon at the fiber input and subsequent amplification. With this consideration the Stokes power P_r can be calculated by integration of the energy equivalent of equation 2.23 over the whole range of the Raman gain spectrum [37].

$$P_r = \int_{-\infty}^{\infty} \hbar\omega \exp[g_R(\omega_s - \omega)I_0L_{eff} - \alpha_r L]d\omega \quad (2.25)$$

Because the main contribution of the integral comes from a narrow region around the peak, the

integral can be approximately evaluated at $\omega = \omega_r$.

$$P_r = P_{r0}^{eff} \exp[g_R(\omega_s - \omega_r)I_0L_{eff} - \alpha_r L] \quad (2.26)$$

Defining the Raman threshold as the point where Stokes power and pump power become equal and assuming $\alpha_s \approx \alpha_r$, the threshold peak power can be found with:

$$P_0 = P_{r0}^{eff} \exp[g_R I_0 L_{eff}] = P_{r0}^{eff} \exp\left[\frac{g_R P_0 L_{eff}}{A_{eff}}\right] \quad (2.27)$$

For a Lorentzian shape of g_R the critical pump power is approximately given by:

$$P_0^{cr} \approx \frac{16A_{eff}}{g_R L_{eff}} \quad (2.28)$$

The equation for the critical signal power was developed assuming continuous wave (CW-) operation. This equation holds for pulse durations larger than 1ns and fiber lengths smaller than 10m. For pulse durations in the ps-range group velocity dispersion effects in the fiber must be taken into account. For even shorter pulse durations ($< 100fs$) the dynamical description of SRS becomes complicated because the response time of the medium has the same order of magnitude.

In conclusion the Raman threshold increases for shorter fiber length and larger effective beam area (MFA). Because the Raman gain is approximately anti-proportional to the wavelength, the Raman threshold will increase for longer wavelengths [37].

2.3.5 Stimulated Brillouin scattering

In the case of Brillouin scattering a pump photon is annihilated while a Stokes photon and an acoustic phonon are created simultaneously. Classically the process can be understood by the

creation of a refractive index grating through an acoustic wave. The pump field generates this acoustic wave via electrostriction. The index grating scatters the pump light similar to the well known Bragg diffraction and the frequency is downshifted due to the movement of the grating at the acoustic velocity v_a (Doppler effect). The main difference between stimulated Brillouin scattering (SBS) and SRS is the phonon type associated with the scattering process (acoustical phonons for SBS instead of optical phonons for SRS). In contradiction to SRS stimulated Brillouin scattering (SBS) occurs mainly in backward direction in a single mode fiber and the Stokes frequency shift is much smaller ($\approx 10\text{GHz}$) than for SRS ($\approx 10\text{THz}$). For the process to occur, both energy and momentum must be conserved for each scattering event (subscripts s and b, for signal and Brillouin photon, respectively) [37].

$$\omega_{vib} = \omega_s - \omega_b \quad \vec{k}_A = \vec{k}_s - \vec{k}_b \quad (2.29)$$

With the Bragg condition, small k_A and assuming $k_s \approx k_r$ an angular dependence of the frequency shift can be found with equation 2.30. The frequency shift is maximal in the backward direction ($\theta = \pi$) and minimal in the forward direction ($\theta = 0$).

$$\omega_{vib} = v_A k_A \approx 2v_A k_s \sin\left(\frac{\theta}{2}\right) \quad (2.30)$$

The threshold condition for SBS can be calculated in a similar manner as for SRS in the steady state CW-approximation.

$$P_0^{cr} \approx \frac{21A_{eff}}{g_B L_{eff}} \quad (2.31)$$

In pulsed operation the threshold is reduced for pulse durations much smaller than the acoustic phonon lifetime of $\approx 1\text{ns}$ and the Brillouin gain drops below the Raman gain. For pulse durations much larger than the acoustic phonon life time ($> 100\text{ns}$) equation 2.31 delivers quite accurate

results. The question of validity becomes more interesting for pulse durations between 1ns and 100ns. Then the spectral width of the signal pulse $\Delta\nu_s$ compared to the Brillouin gain bandwidth $\Delta\nu_B$ needs to be evaluated, especially if $\Delta\nu_s$ exceeds $\Delta\nu_B$ the Brillouin gain is reduced. In such case a corrected version of equation 2.31 should be used [37].

$$P_0^{cr} \approx \frac{21A_{eff}}{g_B L_{eff}} \left(1 + \frac{\Delta\nu_s}{\Delta\nu_B} \right) \quad (2.32)$$

In contrast to SRS the peak value of the Brillouin gain does not change significantly with wavelength. Although the central frequency of the gain peak varies inversely with the pump wavelength, the spectral width reduces quadratically with wavelength. The summation of both effects leads to a more or less wavelength independent peak gain value.

2.3.6 Amplified spontaneous emission

Depending on the number of modes guided in a fiber core a certain amount of spontaneous emission, that is always present when pumping an active medium, is captured in the core and guided in both directions along the fiber. If the pump power is sufficient and inversion exists throughout or in parts of the fiber, this guided spontaneous emission is amplified via stimulated emission. This amplified spontaneous emission (ASE) becomes an issue for pulsed amplification if the interval between pulses is large compared to the upper level lifetime. The energy is stored through pump absorption at times where there is no pulse present. During those times and for relatively high pump powers ASE will build up and reduce the level of inversion. This limits the amount of stored energy and consequently the extractable energy E_{ext} of the amplifier system, which is given by [19]:

$$E_{ext} = GE_{sat} = G \frac{h\nu}{\sigma_a + \sigma_e} \frac{\text{MFA}}{\Gamma} \quad (2.33)$$

In this equation G represents the small signal gain and $\sigma_{a/e}$ the absorption/emission cross section of the active medium. Since light can only be amplified in inverted doped regions, the overlap of mode field area MFA with the doped area needs to be taken into account. This is represented by the fraction of the MFA and overlap integral Γ between mode field and doping distribution [19].

The build up of ASE can have other detrimental effects. Even a small amount of backward propagating ASE can be very harmful to the amplifier front end (e.g. the master oscillator). More dangerous is possible feedback from optical components or fiber end facets that could lead to multiple passes of ASE through the gain medium. Especially for fiber lasers with very large gain this can lead to very fast build up of ASE and parasitic lasing within the amplifier. Parasitic lasing eventually starts in any fiber amplifier of high enough gain, because in-fiber Rayleigh scattering mainly due to impurities of the glass host will be an intrinsic source of distributed feedback, especially in long fibers. This will even occur with the implementation of optical isolators and successful suppression of all external feedback. In some cases parasitic lasing results in very energetic forward- or backward-propagating pulses that are capable of damaging optical components or fiber facets [19].

2.3.7 *Optical damage*

Optical fiber damage is one of the major limitations for high peak power and high energy pulse generation in silica based fiber amplifiers. Unfortunately the literature provides many contradictory and confusing observations of the breakdown behavior of silica and it is difficult to precisely

predict the optical damage threshold for a fiber laser or amplifier. Moreover most of these observations are associated with wavelengths smaller or around $1\mu m$. First this paragraph provides a short overview about observed bulk and surface damage thresholds in silica mainly based on quite recent experiments and simulations by A. V. Smith et al. [41]. Subsequently these results will be compared to observed damage thresholds in optical fibers.

Bulk and surface damage of silica at 1064nm

A common explanation for the bulk damage is the so called electron avalanche driven by the electric field of intense light and subsequent energy transfer of hot electrons to the glass matrix, which is often followed by destructive melting or fracturing. The avalanche process is similar to dielectric breakdown by a DC electric field. Based on this, the threshold irradiance is approximately $5kW/\mu m^2$ for silica. However, many other reports indicate damage ranging 1 to 100 times below $5kW/\mu m^2$. Large discrepancy of reported damage thresholds exists especially for pulse durations in the ns range, as shown in figure 2.15. Smith et al. report a damage fluence of $4.1 \cdot 10^{-5} J/\mu m^2$ at $8ns$ pulse duration and verify the calculated threshold of $5kW/\mu m^2$ with the avalanche electron model [41]. Nevertheless many parameters like pulse duration, focal spot size, stimulated Brillouin scattering, self focussing, color center formation, material densification, impurity inclusions, annealing and cumulative damage when multiple pulses are used can influence the damage threshold and might vary from experiment to experiment. Most importantly in many cases significant differences exist for bulk and surface damage. Surface damage has been reported to be 2 to 5 times lower than bulk damage. However, Smith et al. proved that fine polishing of the surface can increase the surface damage threshold to the same level of bulk damage threshold when the right polishing technique is used [41].

There are still many open questions about the dependence of the damage threshold on wavelength and pulse duration. According to the electron avalanche model the damage threshold should decrease with increasing wavelength, but opposite observations have been made [42, 43, 44] and the prediction of a damage threshold at $2\mu\text{m}$ wavelength is difficult. The scaling of the damage threshold fluence F_{th} with pulse duration τ can be found in various publications to be $F \propto \tau^{0.5}$ [45, 46, 47]. In contradiction to these publications Smith et al. have shown that the threshold increases more dramatically with increasing pulse duration [41].

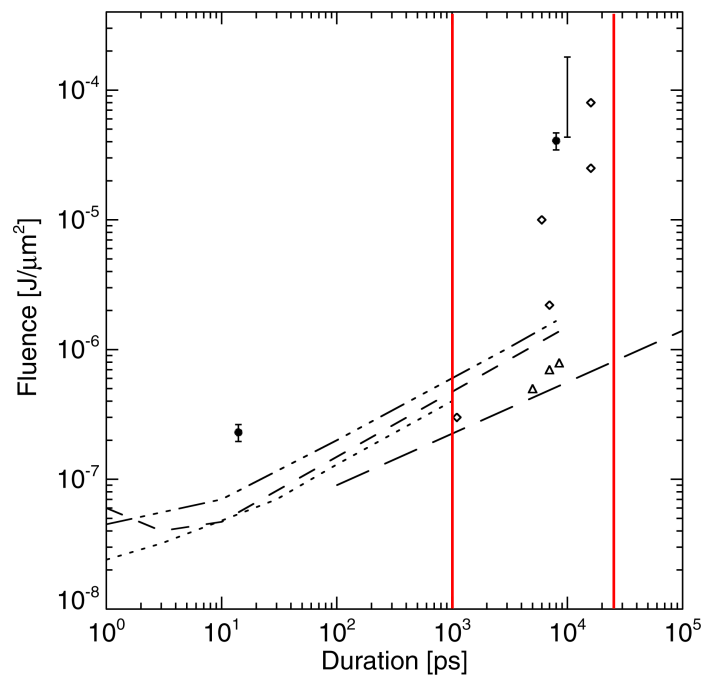


Figure 2.15: Summary of reported damage threshold fluences for silica [41]. Large diversity about damage thresholds for ns-pulse durations

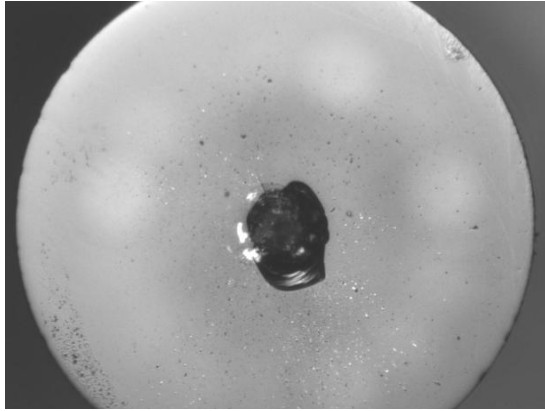
Optical fiber damage

Similar to the previous paragraph reports on optical damage in fibers with pulse durations in the ns range are inconsistent in the literature and sometimes even exceed the threshold value found

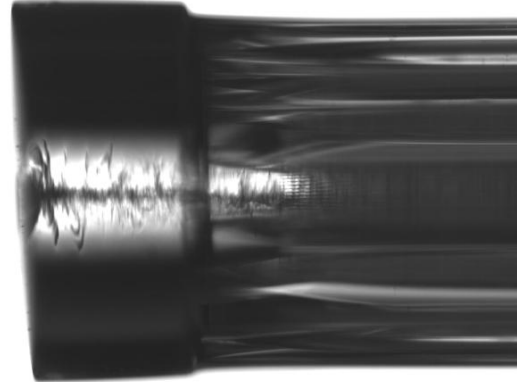
by Smith et al. for bulk silica. More than 4.5MW peak power have been reported before optical damage occurred [3]. This result approaches the expected self focussing limit in silica at $1\mu\text{m}$ wavelength and was achieved by reduction of the peak intensity in the fiber by increasing the MFA of the amplified mode. The exact self focussing limit is not known due to the lack of accurate knowledge about the nonlinear refractive index n_2 .

As mentioned before facets are more fragile and irregularities, roughness or dirt on the fiber facet can significantly decrease the damage threshold. Consequently a proper end facet preparation of the fiber amplifier is of utmost importance for the generation of high peak powers and high pulse energies. A good description for different options of fiber facet preparation is given in an application note by NKT Photonics [48] and parts of it will be discussed in the following.

As discussed earlier an increase of MFA in fibers reduces the peak intensity and lowers the risk of optical damage. However, the MFA cannot be arbitrarily increased if single mode guidance of the fiber is desired. Therefore other damage prevention measures need to be applied in order to achieve best optimal performance. Since damage occurs most likely at the fiber facet it is very important to keep the facet clean. Furthermore it is advisable to collapse the air holes to prevent contamination of the air channels, if a PCF is used. Another way to significantly increase the facet damage threshold is the utilization of silica end caps. End caps can be fused to the fiber end facet and can be polished without risking damage of the wave guiding structure. Moreover end caps allow the beam to expand before exiting the fiber and reduce the peak intensity on the fiber facet. Self lasing can be successfully mitigated up to very high pump powers when the end facets are angle cleaved or angle polished and AR coated. The optical damage of fiber end facets or end caps is often severe and can be seen by viewing the fiber facet in a microscope, as shown in figure 2.16.



(a) End view of a damaged SIF end facet



(b) Side view of a damaged PCF facet on a polished end cap

Figure 2.16: Microscope images of damaged fiber facets (NKT Photonics) [48]

2.3.8 *Thermal limitations and waveguide changes*

Strong heating of the fiber core can occur when the pump energy is not efficiently converted to the laser output. Heating in fibers results primarily from the quantum defect and the quantum efficiency. The quantum defect is defined as the ratio of signal photon energy to pump photon energy. The quantum efficiency accounts for a fraction of excited state energy that is lost via non-radiative relaxations or cross relaxation processes that eventually lead to non-radiative relaxations [22].

The heat deposited in the fiber, especially in the doped region, can affect the lasing threshold, slope efficiency and amplifier gain. Elevated temperatures alter the population distributions amongst the energy levels and change the effective cross-sections of the pump and signal wavelengths. At high temperatures the population is shifted to higher energy manifolds and reduces effectively the number of ions available for amplification in the upper laser level.

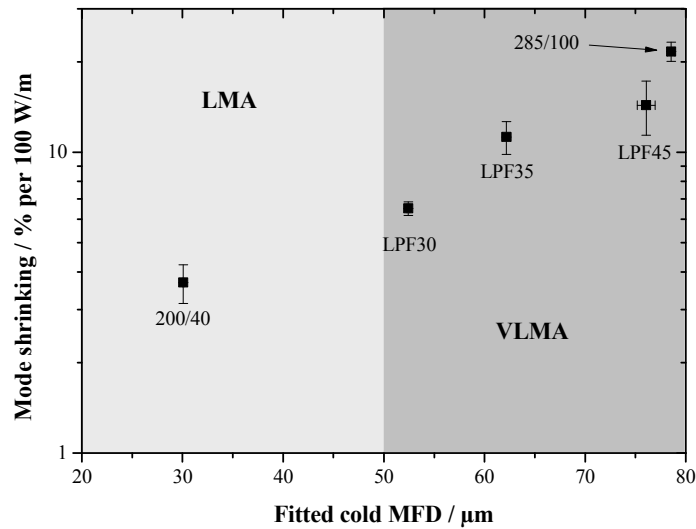


Figure 2.17: Mode field area shrinking due to thermally induced index changes in the waveguide structure of index guiding PCF and LPF [23]

Another thermal phenomenon is mode field shrinking caused by thermally induced waveguide changes in active fibers [23]. This effect occurs in all fiber types but is most noticeable for very larger mode area fiber designs (LPF or rod type PCF with $\text{MFD} > 50\mu\text{m}$). The temperature rise in the core causes a parabolic index profile via the thermo-optical effect which can rise the refractive index by $1 \cdot 10^{-5}/K$ in silica [23]. For high power operation a thermal gradient from the center of the core to the outer rim of several Kelvin is certainly possible. The thermally induced index difference changes the guiding properties of the fiber. The most obvious consequence is the decrease of mode field diameter with increasing heat deposition in the fiber core. Figure 2.17 shows measurement results of approximate mode field shrinking for different fiber types (index guiding PCF's: 200/40 and 285/100 and multiple LPF's) [23]. It can be seen that the mode field diameter may reduce by more than 20% per 100W/m. This reduction of mode field area needs to be considered if nonlinear thresholds are calculated to estimate maximal performance of a fiber amplifier.

Another limitation for average power scaling in single mode high power amplifiers has been observed. An originally single mode high power amplifier shows apparently random relative power content changes of different transverse modes when a certain power threshold is exceeded. This effect is called thermal mode instability [49].

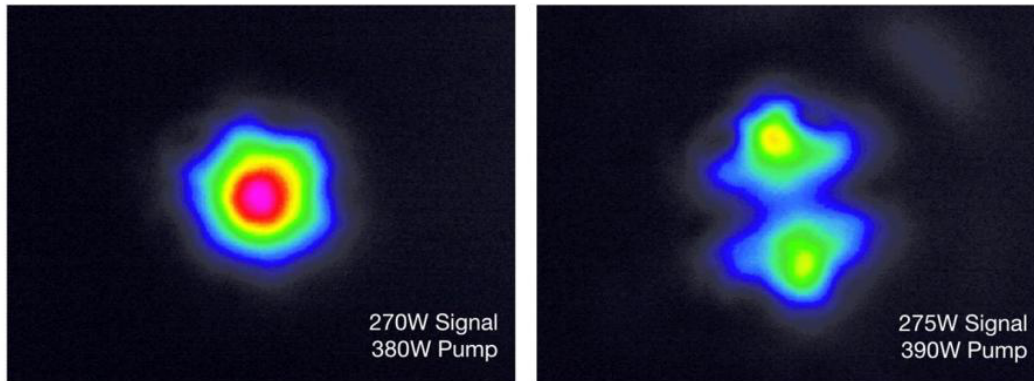


Figure 2.18: Apparently chaotic power content fluctuations between different modes when a certain average power threshold (in this case 270W) is exceeded [49]

Figure 2.18 depicts two beam images, one before the threshold of mode instability is reached and one above the threshold, captured when most of the power was transferred to a higher order mode. Since the discovery of this phenomenon first attempts have been made to physically explain this effect. A numerical model showed, that mode instabilities may be caused by the temporal evolution of a temperature grating in the fiber in interplay with thermally induced non adiabatic waveguide changes [50]. Moreover first mitigation strategies have been successfully tested [51]. To date mode instability seems to be the most limiting factor for average power scaling in ytterbium based fiber amplifiers. This effect has not been reported in active fibers with alternative dopants (e.g. erbium or thulium) mainly because average power scaling there is more difficult than in ytterbium based systems.

2.3.9 Photodarkening

Photodarkening is a phenomenon that causes broad band absorption loss at visible and near infrared wavelengths in rare earth doped silica fibers. Most commonly the absorption becomes stronger over time when the fiber is pumped to high inversion levels [18]. In general losses might be observed in new fibers [52] or grow during operation of a fiber laser or amplifier [53]. It is generally understood that the absorption is associated with clustering effects of the dopants in the core region. The effect seems to be dependent on the doping material, the doping concentration and the fiber fabrication conditions. Co-doping with other materials such as phosphorus, fluorine or aluminum can significantly decrease the photodarkening rate. Although the photodarkening effect appears to be permanent, there have been demonstrations that the effect can be reversed by fiber heating [54] or by irradiation with ultraviolet light [55]. The physical origin of the photodarkening effect is not fully understood and the healing mechanisms can not yet be explained [18].

2.4 Properties of thulium in silica

Neodymium (Nd), ytterbium (Yb), erbium (Er), holmium (Ho) and thulium (Tm) are the most widely used dopants for active fibers. All these different dopants comprise different spectral properties with various advantages and disadvantages with respect to lasing wavelength, efficiency and applications. Nd with lasing wavelength at 1060nm has a very narrow absorption band around 808nm, which requires temperature stabilized diode lasers making the utilization of these fibers for high power applications very difficult. Erbium provides lasing at 1550nm, which is ideal for telecommunication applications due to the extremely low loss of silica fibers at this wavelength. Resonant pumping at 1470nm with novel laser diodes is possible resulting in very low quantum defect and slope efficiencies $> 90\%$. Erbium based high power fiber laser development is currently constrained by low electrical-to-optical efficiency of the diode lasers and clustering of erbium ions

when the doping concentration is increased. Ytterbium has unique properties in terms of simplicity in the energy level structure compared to all other rare earth ions. With an absorption band ranging from 920nm-977nm or 1018nm and lasing wavelengths between 1032nm and 1066nm or 1080nm, respectively, the slope efficiency is usually quite high and can approach 90% [22]. The low quantum defect leads to low heat deposition in the fiber enabling fiber lasers with multiple MW peak power in the fiber and average power greater than 10kW in CW-operation with quasi single mode beam quality [1].

In the following paragraph the spectral properties of thulium as a dopant are discussed in more detail. Subsequently the rate equations of the relevant energy levels are presented and thermal effects on the emission cross section and on the decay dynamics are reviewed. Finally advantages and disadvantages of thulium as a dopant in silica fibers for high power lasers are evaluated.

2.4.1 Energy level structure and pump considerations

In order to understand how high power silica fiber lasers based on thulium can be designed, e.g. what pump schemes can be used and what lasing wavelength can be achieved, it is important to review the energy level structure of thulium in silica. The most important energy levels for thulium fiber lasers are 3H_6 , 3F_4 , 3H_5 and 3H_4 , as shown in figure 2.19.

Typical for rare earth ions in glasses are the splittings of each level into multiple sublevels. The local electric field in the amorphous glass background leads to inhomogeneous broadening. Random inhomogeneities in the glass in interplay with the Stark effect cause different ions to have different energy levels and consequently different transition wavelengths. This effect is the main reason for the broad band emission in thulium from level 3F_4 to 3H_6 . It can be seen that lasing or amplification may occur for wavelengths between $1.8\mu m - 2.1\mu m$, a very broad wavelength range and a unique property of thulium in comparison to other rare earth ions. However, compared to for

example ytterbium the energy level structure and the processes involved, that are important for the lasing or amplification process, are more complex.

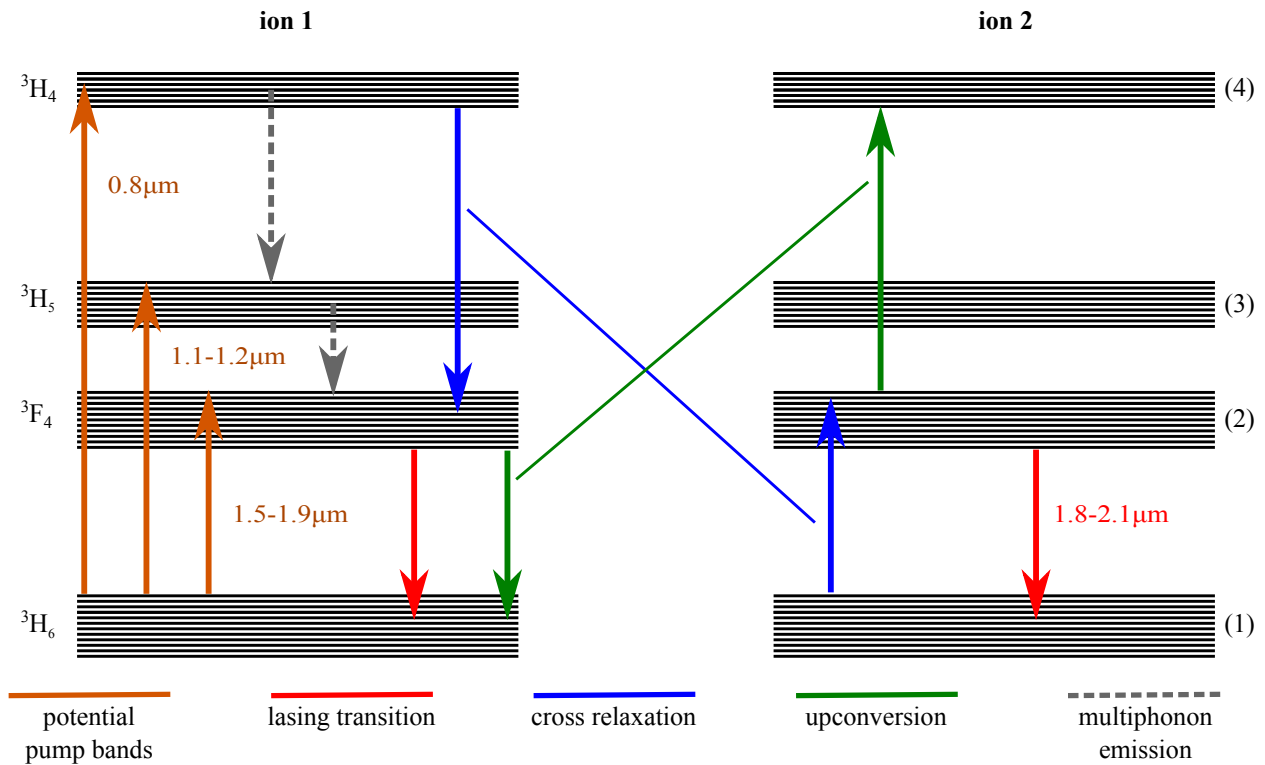


Figure 2.19: Thulium energy level diagram showing possible pump transitions and important processes for laser emission and energy transfer between two ions [56].

Evaluation of the absorption spectrum of thulium in silica in figure 2.20 reveals, there are three possible absorption wavelengths that can be used for pumping thulium. Important parameters for the laser design are the quantum efficiency and the quantum defect. The quantum defect QD is defined as the theoretical loss associated with quantum conversion from one pump photon to one signal photon. The higher the quantum defect, the smaller is the maximum achievable efficiency of a laser and the more pump power goes into heat.

$$QD = 1 - \frac{\lambda_p}{\lambda_s} \quad (2.34)$$

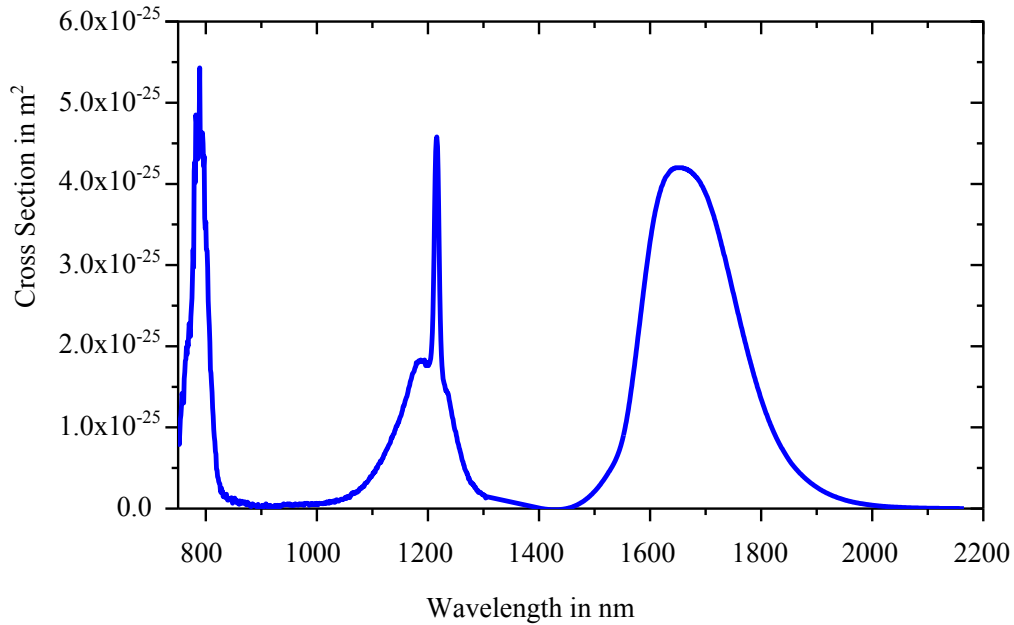


Figure 2.20: Thulium absorption spectrum [57]

In order to minimize the quantum defect it is desirable to pump at wavelengths close to the lasing wavelength. Consequently the first and best choice seems to be the wavelength range between $1.5\mu m - 1.9\mu m$. Unfortunately there are no high power diode pump sources within this wavelength range. It is possible to use erbium fiber lasers at $1.55\mu m$ as pump sources. Often erbium fibers are co-doped with ytterbium enabling diode pumping at 976nm wavelength with electrical to optical efficiencies of $\approx 40\%$. Therefore erbium pumps for thulium lasers are rather inefficient and are mainly used for core pumped thulium fiber lasers. Often the best choice for high power thulium based fiber lasers is the utilization of high brightness multimode diode pumps at 793nm

wavelength. This statement might cause confusion at first, because the quantum defect is 40% for this pump wavelength and efficiencies can be expected to be even smaller due to quantum efficiency (non radiative transitions). However, efficient cross relaxation may reduce the quantum defect to about $\geq 20\%$, making this pumping scheme potentially superior to the others [56].

2.4.2 Cross relaxation and upconversion

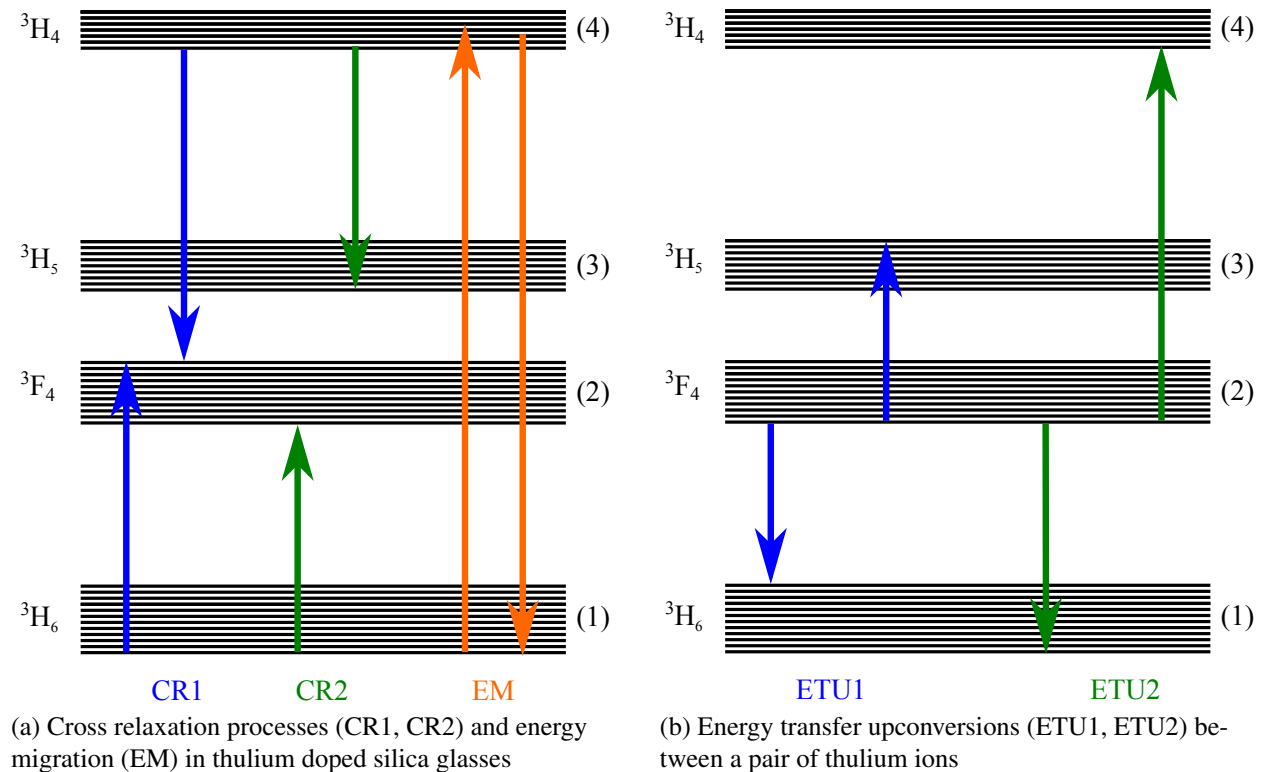


Figure 2.21: Energy transfer between thulium ions for high doping concentrations [56]

In concentrated rare earth doped glasses quenching of the luminescence can occur when energy between one ion is transferred to a nearby ion. It is important to note that such energy transfer can generally be of advantage or disadvantage for the performance of a fiber laser. Processes that are important to the operation of thulium fiber lasers at $2\mu m$ wavelength are those based on cross

relaxation (CR) and energy transfer upconversion (ETU) as already indicated in figure 2.19 and shown in more detail in figure 2.21. These processes include energy transfer between at least two thulium ions, which results in either excitation of an electron from the ground state (1) to an excited state (2) (cross relaxation, CR) or from an already excited state (2) to an even higher state (3 or 4) (energy transfer upconversion, ETU) [56].

Cross Relaxation

The cross relaxation process in thulium can lead to the excitation of two thulium ions to the upper laser level with the absorption of only one pump photon at 793nm. The 793nm pump photon first excites a thulium ion (sensitiser) from the 3H_6 level to the 3H_4 level as sketched in figure 2.19 and again in a little more detail in figure 2.21a. Another nearby ion, still in the ground state (activator ion), experiences a partial energy transfer and is lifted to the excited state 3F_4 , when the sensitiser experiences relaxation to a lower excited state, either 3F_4 (CR1) or 3H_5 (CR2). In silica the 3H_5 lifetime is in the order of a few ns and the final sensitiser states of CR1 and CR2 are effectively the same. Thus, in good approximation both processes can be treated as a single cross relaxation process. Cross relaxation effectively reduces the 3H_4 lifetime (concentration quenching) and increases the integrated fluorescence ratio $^3F_4 \rightarrow ^3H_6$ to $^3H_4 \rightarrow ^3F_4$ and consequently the achievable quantum efficiency (> 1) potentially leading to slope efficiencies of nearly 80% [56]. Currently the highest reported optical to optical efficiency in thulium doped silica fiber is 75% [58].

In general the energy transfer between ions can occur radiatively and non radiatively. However, only the non radiative energy transfer can lead to concentration quenching. One possibility for energy transfer is the overlap of electronic orbitals from sensitiser and activator ions that usually occurs for doping concentrations larger than 4wt.%. For smaller doping concentrations energy

exchange mainly occurs due to Coulombic interactions such as dipole-dipole or dipole-quadrupole interactions with probabilities P_{dd} and P_{dq} , respectively. The total probability for cross relaxation R_{CR} is then given by equation 2.35 (for more detailed calculations compare with [56]) and shows a strong dependence on the distance r between adjacent ions.

$$R_{CR} = P_{dd} + P_{dq} = C_{dd} \frac{1}{r^6} + C_{dq} \frac{1}{r^8} \quad (2.35)$$

Thus, high doping concentrations are desirable to achieve sufficient cross relaxation in thulium doped silica fibers. However, the level of doping concentration is strongly limited by clustering effects that can lead to dominant energy upconversion processes. Co-doping with aluminum has shown to prevent clustering even for relatively high doping concentrations [59]. One additional process that may enhance the contribution of cross relaxation to the slope efficiency is energy migration (EM) as also shown in figure 2.21a. The important feature of energy migration is the allowed electric quadrupole energy transfer process that might enhance the probability of cross relaxations in thulium doped silica [58].

Energy transfer upconversion

Energy transfer upconversion (ETU) occurs only between excited ions and does not involve energy migration. The most important ETU processes for thulium in silica are sketched in figure 2.21b. Considering the energy difference between initial and final states for these ETU processes reveals, that ETU1 is highly endothermic (requires phonon annihilation) and ETU2 is highly exothermic (requires phonon creation). Consequently both processes are temperature dependent and in general exothermic processes are more probable than endothermic processes. It was shown that the ETU2 process leads to quite effective emission of 793nm light from the 3H_4 -level when a thulium doped (200ppm) silica fiber was illuminated with 1586nm light, which populates the 3F_4 -level [60]. At

first the ETU1 process seems to be less important because it involves the transition ${}^3F_4 \rightarrow {}^3H_5$, which lies in the high absorption range of silicate glass. However, if clustering of thulium ions occurs, the ETU1 may contribute significantly to the concentration quenching of the upper laser level 3F_4 and reduces the overall population inversion. Moreover, in highly clustered systems the ion separation is very small and ETU processes may become the dominant ion-ion interactions. Thus, threshold and slope efficiency might suffer from strong ETU in thulium doped systems where clustering is not prevented (e.g. by co-doping with aluminum) [56, 59].

In conclusion thulium doping concentrations and aluminum co-doping need to be optimized to find a trade off between maximization of cross relaxation processes (high thulium concentration) and minimization of ETU processes (low thulium concentration, aluminum doping to prevent clustering) [56].

2.4.3 Rate equations

In this subsection the rate equations for the populations of the 4 major thulium energy levels for the 790nm pumping scheme (${}^3H_6 \rightarrow {}^3H_4$) and the lasing/ amplification in the $1.8 - 2.1\mu m$ wavelength regime are developed, including the role of the previously discussed cross relaxations and energy upconversion processes. The rate equations include terms for the population of the n's level N_n , radiative spontaneous transition rates from the n's level to the m's lower levels R_{nm} , non-radiative emission rates from the n's level to the next lower level Γ_n , stimulated emission rates W_{nm} , stimulated absorption rates W_{mn} and the nonlinear terms for cross relaxation/ energy upconversion $CR_{1,2}$ [61, 62].

$$\frac{N_1}{dt} = \sum_{n=2}^4 R_{n1}N_n + \Gamma_2N_2 - W_{14}N_1 + W_{21}N_2 - W_{12}N_1 - CR_1 - CR_2 \quad (2.36)$$

$$\frac{N_2}{dt} = \sum_{n=3}^4 R_{n2}N_n + \Gamma_3N_3 - R_{21}N_2 + \Gamma_2N_2 - W_{21}N_2 + W_{12}N_1 + 2CR_1 + 2CR_2 \quad (2.37)$$

$$\frac{N_3}{dt} = R_{43}N_4 + \Gamma_4N_4 - \sum_{m=1}^2 R_{3m}N_3 - \Gamma_3N_3 - CR_2 \quad (2.38)$$

$$\frac{N_4}{dt} = W_{14}N_1 - \sum_{m=1}^3 R_{4m}N_4 - \Gamma_4N_4 - CR_1 \quad (2.39)$$

The light induced transition rates for pump and signal intensities $I_{p/s}$ with $\lambda_{p/s}$ as the signal and pump wavelengths, $\sigma_{a/e}$ as the absorption and emission cross-sections are given by [62]:

$$W_{14} = \sigma_a(\lambda_p)\lambda_p \frac{I_p}{hc} \quad (2.40)$$

$$W_{12} = \sigma_a(\lambda_s)\lambda_s \frac{I_s}{hc} \quad (2.41)$$

$$W_{21} = \sigma_e(\lambda_s)\lambda_s \frac{I_s}{hc} \quad (2.42)$$

The cross relaxation and energy upconversion rates are represented by CR_1 and CR_2 , that is [61]:

$$CR_1 = k_{4212}N_4N_1 - k_{2124}N_2^2 \quad (2.43)$$

$$CR_2 = k_{3212}N_3N_1 - k_{2123}N_2^2 \quad (2.44)$$

The parameter k_{ijkl} describe the energy transfer processes $i \rightarrow j$ and $k \rightarrow l$ and depend in general on the thulium ion concentration and clustering effects in the doped silica glass. According to reference [61] the cross relaxation parameters have the following dependence (although clustering effects might change these relations drastically):

$$k_{2124} = 0.084k_{4212} \quad \text{and} \quad k_{2123} = 0.5k_{3212} \quad (2.45)$$

Table 2.1: Radiative decay rates, non-radiative decay rates and cross relaxation upconversion constants [61, 63, 64]

radiative decay rates in s^{-1}	R_{43} 14.61	R_{42} 58.71	R_{41} 716.9	R_{32} 3.89	R_{31} 181.23	R_{21} 1250
non radiative decay rates in s^{-1}	Γ_4 80594.3	Γ_3 $2.93 \cdot 10^7$	Γ_2 2670			
cross relaxation in $10^{-24}m^3s^{-1}$	k_{4212} 78.3	k_{2124} 6.58	k_{3212} 3.00	k_{2123} 1.50		

2.4.4 Thermal effects

The performance of thulium lasers depends strongly on the temperature of the laser material and significant heating of the active medium for high pump powers can be expected due to the large quantum defect [65]. With increasing temperature the population distribution within an energy manifold is shifted from the lower Stark levels to higher Stark levels. In thulium the upper laser level is usually among the lower Stark levels of 3F_4 and the ground level of the laser transition is among the higher Stark levels of 3H_6 . Consequently in the case of high temperature in the active region the available population among the lower Stark levels of 3F_4 will be smaller than for low

temperature. Similarly the higher Stark levels of 3H_6 will be more populated. Both effects will reduce the population inversion that is effectively available for lasing or amplification. As a result lasing threshold and slope efficiency will be reduced for high temperatures. In addition large heat generation in the doped core region of a fiber may lead to thermal lensing at the fiber output and to stress induced birefringence causing degradation of beam quality and output power [65].

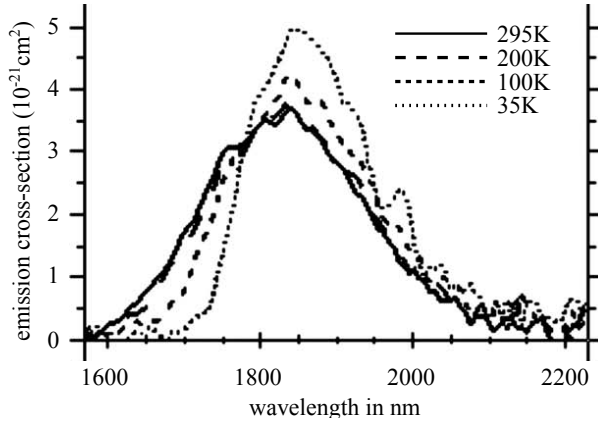
Temperature dependence of the emission cross-section

Generally the luminescence bandwidths tend to increase with temperature as a result of reduced emission and absorption cross-sections for higher temperatures [65]. A comparative study of the temperature dependent properties of thulium was done by Turri et. al [63] and they found that the emission cross-section is indeed dependent on temperature as depicted in figure 2.22a.

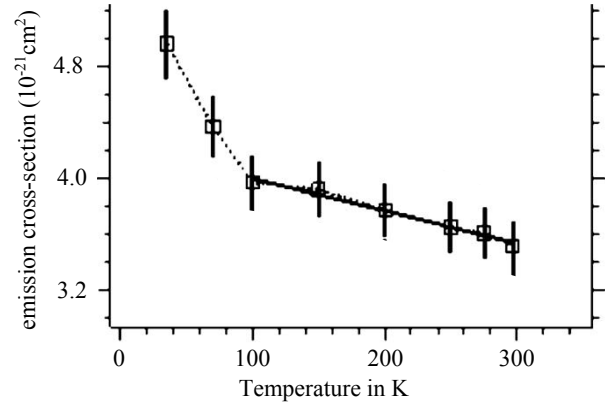
The change of the cross section with temperature is largest at low temperatures. For temperatures above 100K up to room temperature the temperature dependence appears linear for the peak absorption value. In this range the cross-section to temperature dependence can be approximated equation 2.46 while the peak emission wavelength is shifted according to equation 2.47 [63].

$$\sigma_e^{peak}(T) = 5.9 \cdot 10^{-21} cm^2 - 2.3 \cdot 10^{-24} \frac{cm^2}{K} T(K) \quad (2.46)$$

$$\lambda_e^{peak}(T) = 1871 nm - 0.21 \frac{nm}{K} T(K) \quad (2.47)$$



(a) Emission cross-section ${}^3F_4 \rightarrow {}^3H_6$ of thulium in silica measured for different temperatures



(b) Peak emission cross section as a function of temperature

Figure 2.22: Temperature dependence of the stimulated emission cross-section in thulium doped silica [63]

Decay dynamics

As briefly discussed in subsection 2.4.3 the spontaneous decay rates of each level can be separated in non-radiative and radiative decay rates. The non-radiative decay rates tend to increase with growing temperature while the radiative lifetimes are mainly independent of temperature. It is very likely that the cross relaxation and upconversion processes are also strongly influenced by temperature. Unfortunately it is very difficult to estimate how temperature changes in the fiber core affect these two competing processes [65]. However it is possible, to some extent, to describe the temperature dependence for non-radiative decay rates. The non-radiative lifetimes τ_{nr} generally decrease with increasing temperature. For most rare earth doped glasses the temperature dependence can be described by:

$$\frac{1}{\tau_{nr}} \propto (1 + n(T))^p \quad \text{with} \quad n(T) = \frac{1}{e^{h\nu/kT} - 1} \quad (2.48)$$

Unfortunately the situation is more complicated for thulium in silica glass. Turri et al. have shown that the fluorescence decay profile of the 3F_4 has a double exponential behavior for temperatures above $\approx 150K$. They found a fast ($\tau_f = 115\mu s$) and a slow ($\tau_s = 650\mu s$) lifetime at room temperature, as shown in figure 2.23 [63]. In general the decay lifetimes appear relatively constant for temperatures above 200K.

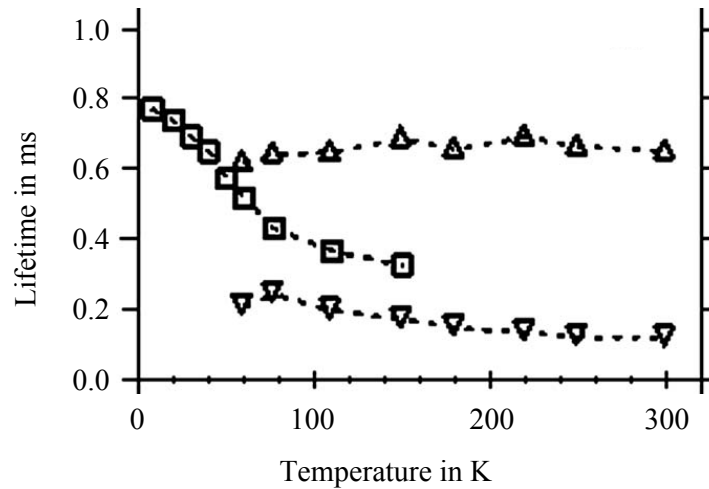


Figure 2.23: The lifetimes for fluorescence of transition ${}^3F_4 \rightarrow {}^3H_6$ of thulium in silica measured for different temperatures [63]

2.5 Advantages of thulium

In general thulium high power fiber laser sources suffer from lower efficiency compared to ytterbium based fiber lasers. Consequently very high average power generation has been limited to 1kW in thulium based systems [66]. Fiber designs that enable sufficient cross relaxation represent one route to address thermal issues. The development of high power laser diodes for in band pumping would enable more efficient thulium fiber lasers as well. Regardless of the rather bad thermal properties, thulium based fiber lasers offer unique features that cannot be provided by other rare earth based fiber lasers.

The $2\mu\text{m}$ emission wavelength of thulium is of particular interest for mode area and peak power scaling. First, the $2\mu\text{m}$ wavelength allows theoretically for twice the mode field diameter while preserving single mode behavior compared to $1\mu\text{m}$ wavelength. This alone may enable peak power scaling in thulium doped fiber lasers beyond ytterbium doped systems, since nonlinear effects in the fiber scale with mode field area. Second, nonlinear effects such as stimulated Raman- and Brillouin-scattering as well as self-focusing are inverse proportional to the wavelength (squared), stressing the potential of thulium doped fiber lasers to generate peak powers beyond the 10 MW-level in the future. An important feature of thulium high peak power fiber lasers is the option of directly pumped optical parametric oscillators (OPO). P. Kadwani et. al have realized directly pumped OPO mid infrared sources utilizing high peak power thulium based fiber lasers [5].

The very broad emission spectrum of thulium compared to all other commonly used rare earth ions may enable the direct generation of fs-pulses in mode-locked thulium based fiber lasers by taking advantage of anomalous dispersion of silica glass at $2\mu\text{m}$ wavelength. High repetition rate, high average power laser sources at $2\mu\text{m}$ wavelength may be of particular interest for high harmonic generation (HHG). Limpert et al. have demonstrated HHG with ytterbium based fiber laser systems at $1\mu\text{m}$ wavelength and generated attosecond-pulse durations at 150kHz repetition rate [67]. The longer emission wavelength of thulium can be of advantage for higher energy cutoff HHG. Another advantage of the long and broad emission wavelengths of thulium are absorption bands in water and carbon dioxide that can be used for many sensing and medical applications. An example for a sensing application is light detection and ranging (LIDAR). A tunable thulium laser can be used to detect absorption resonances of molecules and ranging information can be detected due to reflection. Coherent Doppler LIDAR is capable of detecting horizontal and vertical wind velocities in the atmosphere [68]. Medical applications are possible due to the water absorption band in the range of $1.91\mu\text{m}$ and $1.94\mu\text{m}$. Since water is often the primary constituent of biological tissue, thulium fiber lasers are excellent, robust and flexible sources for tissue ablation or cutting [69].

CHAPTER 3: EXPERIMENTS

The experiments performed in this work focus on the utilization of thulium doped, rod-type, silica based PCF designs. Two different designs have been characterized in a CW-lasing setup and utilized for CW- and pulsed amplification in MOPA configuration. The detailed specifications and a modal analysis, kindly provided by Clemence Jollivet and the fiber laser group of Prof. Axel Schülzgen at CREOL, UCF [70], are presented in subsection 3.1.

Because of the novelty of thulium PCF rods with very large core area, the chemical design as well as the fiber design are not optimized. As discussed earlier it is very important for fiber laser performance, that clustering effects are avoided in the fiber core. To get a sense of the clustering in these novel fiber designs, a photodarkening test was performed and the experimental setup and the results are presented in subsection 3.2.

CW-lasing tests and ASE measurements were carried out for both PCF rods and the experimental details are shown in subsection 3.3. As part of these investigations slope efficiency, maximum output power, beam quality and wavelength tuning range were examined. The results of this work have been published in Optics Letters [71].

The ultimate goal of this work is to maximize peak power, pulse energy and average output power by implementing the PCF rod design as a final amplification stage in a master oscillator power amplifier. The first step to investigate the performance of the thulium doped PCF rod design is the amplification of a CW-signal as discussed in subsection 3.4. In this section the CW performance of the master oscillator and the flexible PCF as first amplification stage are discussed. As part of this section the mode field diameter of rodB was determined and compared to the simulation results of subsection 3.1. Subsequently the final amplification results for the rod type design as well as a characterization of beam quality for different output powers are presented. Thermal effects have

been identified as the main limiting factor for CW-average power scaling.

The last subsection 3.5 presents the results of the pulsed amplification with the afore mentioned two stage MOPA system. The MOPA characteristics for pulsed operation are shortly discussed in subsection 3.5.1. Pulsed amplification experiments were conducted for rodB, that is most promising for peak power scaling due to the large mode field area and excellent beam quality. The final amplification results for various pulse repetition rates and pulse durations are presented in subsection 3.5.2. As part of these experiments MW-level peak power was achieved at 1kHz repetition rate and 6.5ns pulse duration. This world record result has been published in Optics Letters [20].

3.1 Thulium doped rod-type PCF

The advantages of rod-type fiber designs have led to a significant increase of peak power and pulse energy in $1\mu m$ wavelength, ytterbium based systems. Before this work, thulium doped rod-type PCF had not been investigated but as will be shown, the advantages of the rod design also apply at $2\mu m$ wavelength. The first flexible PCF manufactured by NKT Photonics A/S (Denmark) was characterized in 2011 [72] and showed promising results particularly in terms of beam quality and mode field diameter (MFD), which is the main feature for potential pulse energy and peak power scaling in fiber lasers. The slope efficiency achieved in this fiber in lasing configuration was 35%, thus further optimization of the fiber design is required to achieve efficient cross relaxation with maximum efficiencies in the order of 70%. Subsequently a Q-switched oscillator was realized with this fiber design [12] and it was implemented as first amplification stage in a MOPA system [13].

In this work two different thulium doped PCF-rods with $65\mu m$ (rodA) and $80\mu m$ (rodB) core diameters have been characterized. The PCF rods tested were fabricated by NKT Photonics A/S. Figure 3.1 shows an image of the fiber facet of rodB. The rods have an all-glass double clad design

and an inner air cladding with $> 0.4NA$ at $790nm$. The silica glass cores are doped with 2.5% Tm and are co-doped with Al (1:8 Tm/Al ratio) to circumvent clustering.

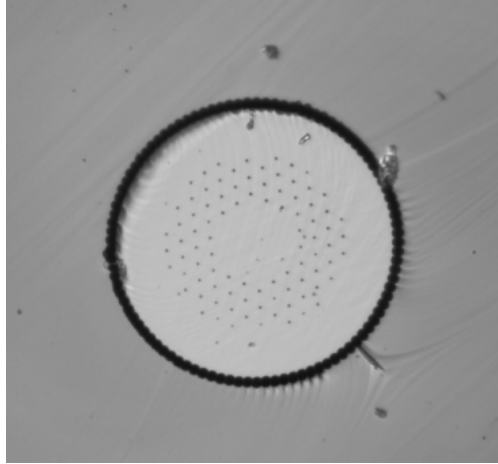
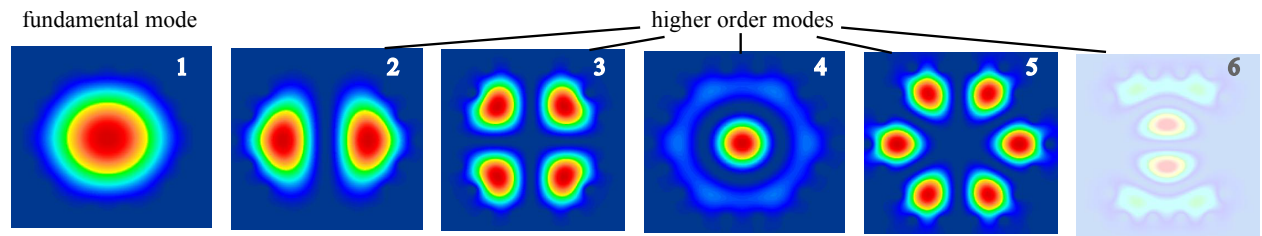


Figure 3.1: Image of the fiber facet, showing the $80\mu m$ diameter core and part the $220\mu m$ diameter inner cladding.

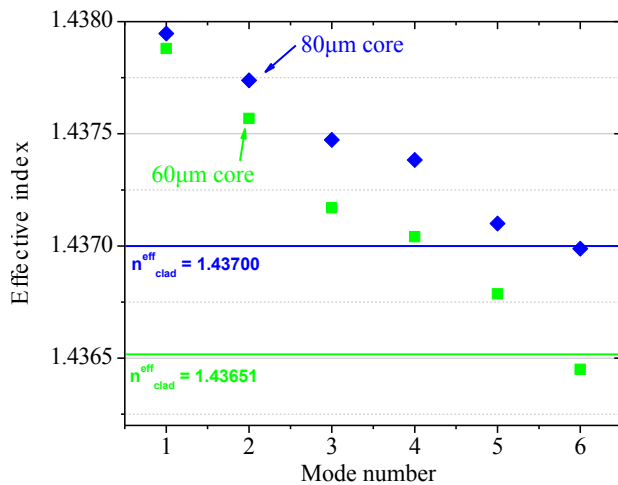
Table 3.1: Detailed specifications of the two thulium doped rod-type PCF's

	RodA	RodB
core diameter	$65\mu m$	$80\mu m$
mode field diameter	$46\mu m$	$56\mu m$
cladding diameter	$180\mu m$	$220\mu m$
hole to hole pitch	$11.2\mu m$	$13.7\mu m$
hole diameter	$2.17\mu m$	$2.62\mu m$
fiber length	$1.27m$	$1.36m$

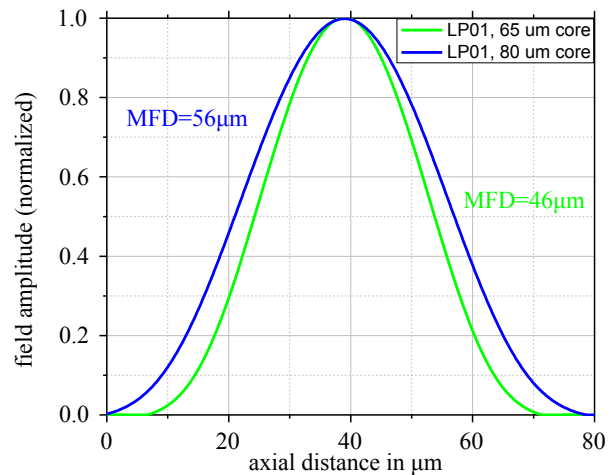
Table 3.1 provides more detailed information about the two different designs. To prevent contamination, the fiber ends were fused to collapse the air holes. Parasitic lasing can become an issue at high pump powers, especially when utilizing the rods as amplifiers. Hence, the fiber ends of the rods were cleaved and then polished at an angle of $\approx 4^\circ$ (done by NKT photonics A/S).



(a) Calculated guided modes of rodB, the modes for rodA are similar



(b) Guided modes cut off for rodA ($65\mu\text{m}$ core) and rodB ($80\mu\text{m}$ core)



(c) Calculated MFD ($1/e^2$)

Figure 3.2: Theoretical modal analysis performed by Clemence Jollivet, CREOL 2012 [70]

The theoretical modal analysis of the two rods was performed by Clemence Jollivet in the group of Prof. Axel Schülzgen (CREOL, 2012/2013) with the FIMMWAVE software (distributed by the company Photon Design) [70]. This software provides a full vectorial finite element mode solver. Using the rod parameters given in table 3.1 and assuming a signal wavelength of $2\mu\text{m}$ the simulation revealed multi-mode character for both rods. The measured value of the refractive index in the core regions is $n_{core} = 1.43808$ and effective cladding refractive indexes of $n_{cladding} = 1.43651$ (rodA) $n_{cladding} = 1.43700$ (rodB) can be obtained by averaging over air holes and solid glass material. Equation 2.2 can be used to find the NA of the fibers with $\text{NA}=0.067$ (rodA) and $\text{NA}=0.056$ (rodB). Figure 3.2a depicts the guided modes of rodB. The first mode has a Gaussian

like profile, while the higher order modes show typical spatial intensity distributions as known from step index fibers, supporting the expected index guiding nature of this PCF rod. RodA has a similar set of higher order modes and a separate presentation is unnecessary. The guided modes cut off is shown in figure 3.2b. The simulation reveals that there are 5 guided core modes for rodA and rodB. Mode number 6 in rodB might be weakly guided, since the effective index of this mode is very close to the cut off index within the range of possible simulation error. By investigating the fundamental mode beam profile the effective mode field diameter can be determined as depicted in figure 3.2c.

3.2 Photodarkening measurement

As briefly discussed in subsection 2.3.9, the photodarkening effect is believed to be related to clustering effects in the core. These clustering effects can significantly reduce laser or amplifier performance. One prevention measure is co-doping with other materials, e.g. aluminum. The aluminum concentration in the core area of rodA and rodB is approximately 8 times the concentration of doped thulium. A possible setup to measure the photodarkening in a fiber is shown in figure 3.3.

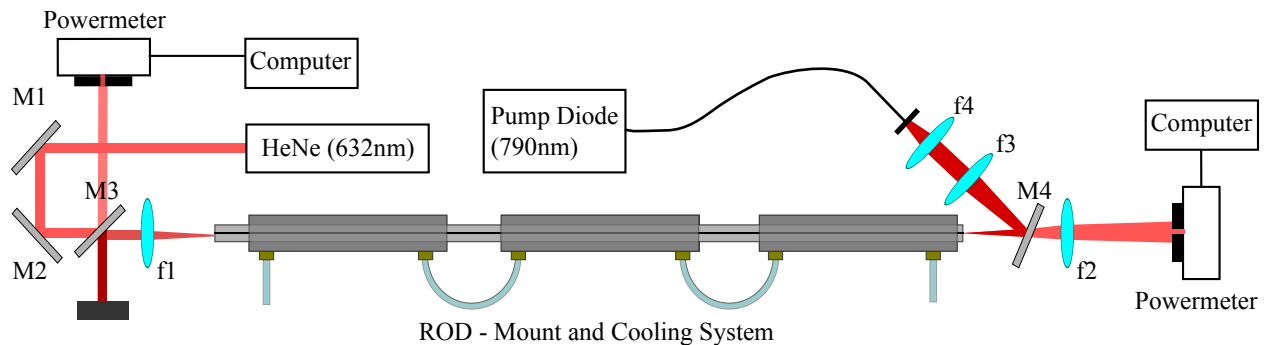


Figure 3.3: Setup for the measurement of photodarkening in fibers

In preparation for the photodarkening and future experiments the rod mount and the cooling system were designed and installed. A metal rail with a centered slit was used to hold the rod under test in position. Six water cooled metal blocks were distributed along the rail and mounted below and on top of it. The pump light was extracted from a pump diode at 790nm (DILAS) with a maximum output power of 100W and coupled to the inner cladding of the fiber using a water cooled imaging system (f3, f4) and a mirror with high reflectivity at 790nm (M4). A Helium Neon (HeNe) laser at 632nm and 5mW output power was chosen to serve as the probe beam. The beam was redirected by two silver mirrors (M1,M2) and coupled into the core of the fiber using a lens (f1) with a focal length of 5cm. Another mirror with high reflectivity at 790nm was used to extract the pump light that was transmitted by the fiber. The partial reflection of the probe beam at this mirror was used to measure possible power fluctuations of the HeNe laser output. The probe beam was imaged and magnified with a lens of 10cm focal length (f2) after exiting the rod. A pinhole clipped the beam before it hit the power meter and was adjusted in such a way, that mostly the center (core) part of the probe beam was transmitted.

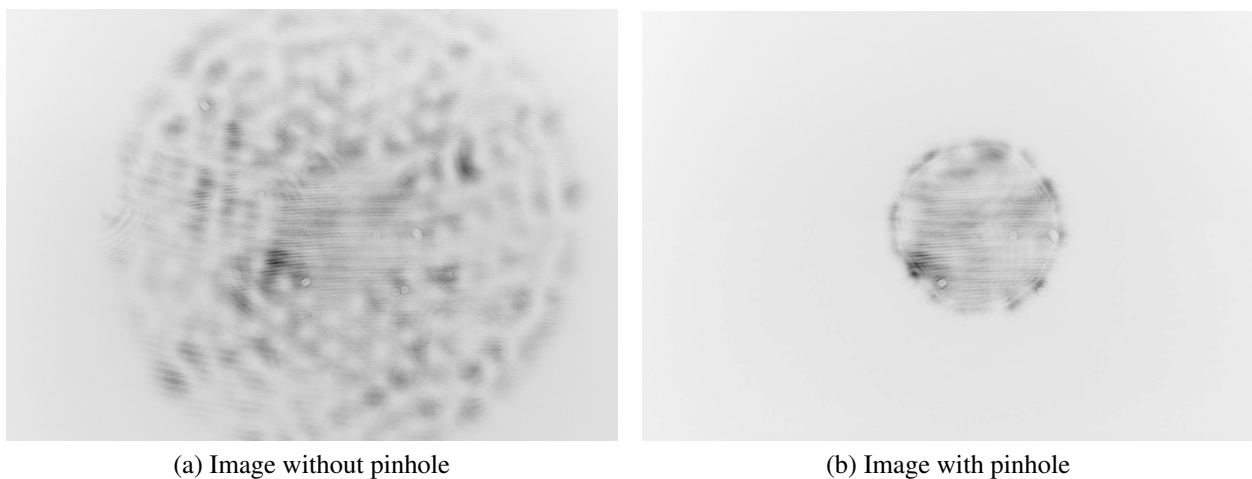


Figure 3.4: Image of the fiber end facet at maximum light coupling in the fiber core with and without pinhole (images inverted for better visibility)

Due to the very small NA of the rod the experimental challenge of this measurement was to couple the 632nm light into the core. Several attempts were made to couple as much light as possible into the core using various lenses (focal lengths from 25mm to 100mm) and different laser sources (green laser diode at 532nm and HeNe laser at 632nm). Best coupling was achieved with a lens of 50mm focal length and the HeNe laser but most of the light was trapped in the cladding. An example of the achieved coupling is shown without pinhole in figure 3.4a and with pinhole in figure 3.4b. However, the light power in the core was rather small ($\approx 100\mu W$) and changed drastically when pumping the rod. The pumping causes thermal gradients within the rod. This generates stresses and causes small movement of the rod influencing the coupling.

In order to realize a photodarkening measurement a long term testing at high power is required. Therefore the power outputs of the HeNe laser and the probe signal were logged over about 9 hours while pumping the fiber rod with about 50W at 790nm. The used power meter software did not allow to log the data parallel at the same computer. This issue lead to the use of two computers and consequently to asynchronicity. To minimize this effect single consecutive automatic measurements have been taken in time steps of 1.5s. However, after 9hours the measurement count differed by about 100 between the two signals. To receive the final plot data, the measured probe power was divided by the HeNe signal and then normalized to the average of the resulting data points. Because of the different measurement counts a previous step was inevitable. The signal with less measurement counts was interpolated to match the total counts of the other signal.

The photodarkening measurement was carried out for rodB only and the result is shown in figure 3.5. It can be seen that the power fluctuates by about $\pm 6\%$ of the average signal. Those fluctuations are due to the thermal gradients in the fiber and environmental effects like air conditioning, ambient light in the laboratory and vibrations of the laboratory table. Furthermore the arbitrary change of the probe signal suggests a rather bad coupling in the core of the rod. There is no indication of a global decrease of signal power with time. However, the effect might not be observable within

the achieved signal to noise ratio. The signal to noise ratio could be improved by achieving a much better core coupling. Additionally stronger pumping and a shorter fiber could lead to strong inversion throughout the fiber and cause faster aging and formation of color centers.

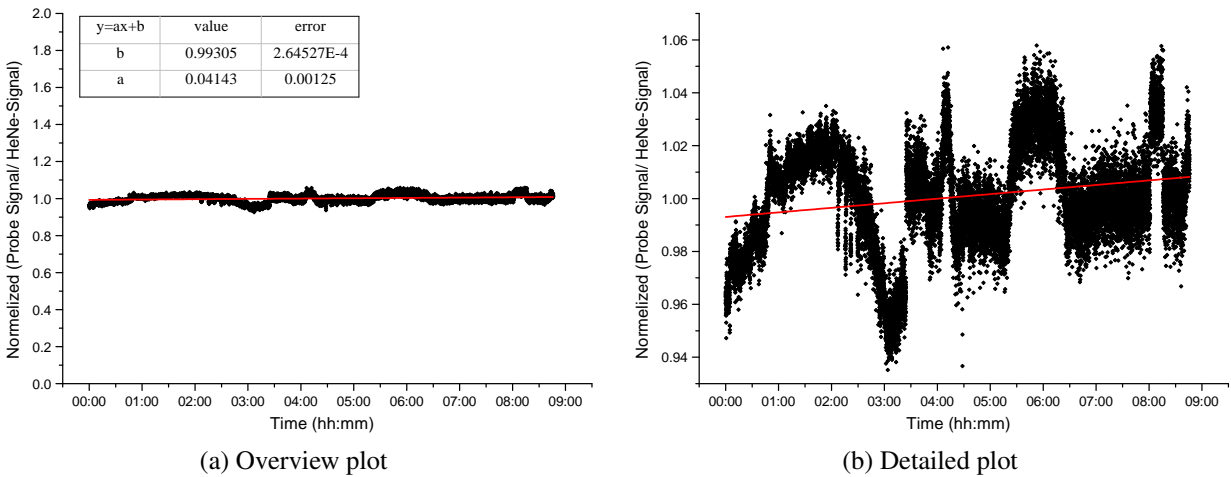


Figure 3.5: Normalized Signal Power divided by HeNe Power

It can be concluded that there was no photodarkening observable with the rod under test. Moreover the rod has been used for several later experiments that required long operation times at high pump powers close to 250W (subsection 3.4) and a drop of efficiency has not been observed.

3.3 CW-lasing and ASE

One way to characterize an active fiber in terms of efficiency, beam quality, spectrum and tunability is testing the performance as an active medium in CW-lasing configuration. A similar characterization was conducted for the first thulium doped flexible PCF in 2011 [72]. This novel design with $> 1000\mu m^2$ mode field area (MFA) provided single-mode, Gaussian like beam quality with $M^2 < 1.15$ and polarized output with a maximum average output power of 4W. The broad spectrum of thulium in the $2\mu m$ range can be exploited in terms of wavelength tunability. Clarksen et.

al have demonstrated a cladding-pumped thulium doped silica fiber laser with wavelength tuning from 1860nm to 2090nm at moderate output powers of $> 5W$ [73]. Likewise McComb et. al have presented a tunable oscillator from 1900nm to 2100nm with output powers $> 10W$ [74]. In this work more than 20W output power and wavelength tunability from 1810nm to 1990nm were achieved in a thulium doped PCF rod and some of the results were published in Optics Letters [71]. Recently a thulium doped, silica based large pitch fiber rod reached $> 50W$ average output power in CW-lasing configuration [75].

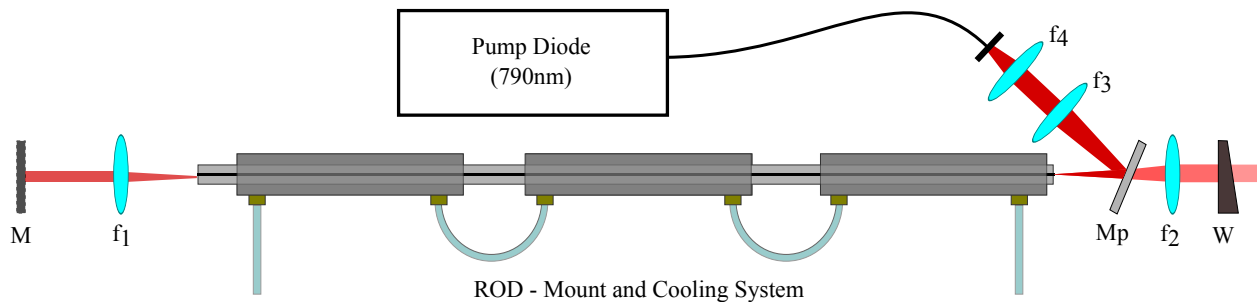


Figure 3.6: The schematic sketch shows a counter propagating laser cavity. A wedge with 4% reflectivity at $2\mu m$ was used as output coupler. For wavelength tuning the mirror at $2\mu m$ was replaced by a gold reflection grating. The same pump telescope was used for both rods [71].

The experimental setup for CW-lasing configuration is shown in figure 3.6. Two metal V-grooves with lengths 1.27m for rodA and 1.36m for rodB were made to support the fiber rods. The V-groove acts as a heat sink and was cooled to $13^\circ C$ by six water-cooled aluminum cuboids. The rods were pumped with a 793nm, 100W laser diode (DILAS). The pump light was delivered by a $200\mu m$ multimode fiber and was subsequently coupled into the rods by an 1:1 telescope with $f = 100mm$ and a dichroic mirror reflecting 793nm light and transmitting light at $2\mu m$. On the side opposing the pump input the beam was collimated by an 26mm triplet with anti-reflection coating at $2\mu m$ wavelength. A high-reflectivity mirror at the signal wavelength reflects the signal light back into the rod. After leaving the rod on the pump coupling side, the signal was collimated by an uncoated 50 mm doublet lens that introduces a signal loss of $\approx 15\%$. The uncoated surface

of a 3° wedge ($\approx 4\%$ reflectivity) was utilized as the output coupler and completed the laser cavity. To investigate oscillator wavelength tunability the high reflectivity mirror M was replaced by a 600 line/mm gold-coated reflection grating [71].

3.3.1 Lasing spectra and ASE

The setup shown in figure 3.6 can not be used for the pure investigation of ASE. Thus, the ASE experiments were conducted without the use of the $2\mu\text{m}$ mirror M and the out-coupling wedge W. Clearly ASE should be observable on both output ends, if the pump power level is sufficient to produce a strong enough signal. Here the ASE was generally weak (in the order of 10th of mW) at the pump coupling side (counter propagating) and very weak on the other side (co-propagating). The output power of ASE is limited by parasitic self lasing effects that occur for relatively high pump powers. The parasitic lasing threshold is mainly determined by the back reflections of the fiber facets or the lenses.

The ASE spectra at 17W pump power are depicted in figure 3.7a. The spectra extend from 1650nm to 2050nm for rodA and and 2150nm for rodB, respectively. The peak wavelength of both spectra is approximately 1900nm. The ASE spectrum of rodA decreases more rapidly for longer and shorter wavelength relative to the peak wavelength than the ASE spectrum of rodB. The flexible PCF that was characterized in [72] showed ASE extending only from 1850nm to 2030nm. The difference of the shorter wavelength edge compared to the rods can be explained by reabsorption and the longer fiber. However, it seems that the longer wavelength edge is influenced by the MFD. The longer wavelength edge increases from 2030nm (MFD = $36\mu\text{m}$) to 2050nm (MFD = $45\mu\text{m}$) to 2150nm (MFD = $80\mu\text{m}$). Possible explanations could be found in the different guiding properties and gain per unit length of the different fibers. With increasing MFD the NA of the fibers decreases and the confinement in the fiber core is changed. A larger MFD increases the ions per unit length and parts

of the larger mode are more amplified than others. An alternative explanation is the temperature dependence of the emission and absorption cross sections. The larger the core diameter, the more ions are present per unit length. Consequently the pump absorption per unit length as well as the temperature per unit length are increased. As discussed in subsection 2.4.4, the emission and absorption cross section become smaller for increasing temperature [65]. This leads to a reduction of peak cross section but to an increase of bandwidth. This is exactly what can be observed in the ASE spectra in figure 3.7a and might indicate that the temperature in the core varies strongly with core diameter. One might argue that the difference of core radius between rodA and rodB is not significant. However, a 1:1 imaging telescope was used to focus the beam from the $200\mu\text{m}$ pump delivery fiber to the rod facet. Consequently the pump absorption in rodA was weaker than for rodB, since the pump cladding diameter of rodA is only $180\mu\text{m}$ compared to $220\mu\text{m}$ for rodB.

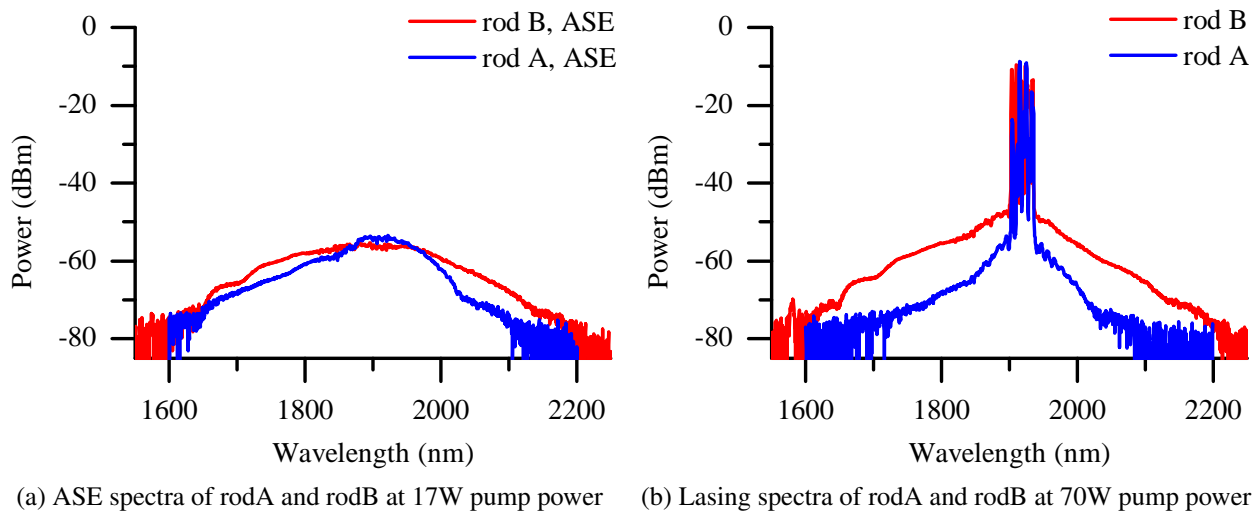


Figure 3.7: Spectral analysis of lasing operation and ASE

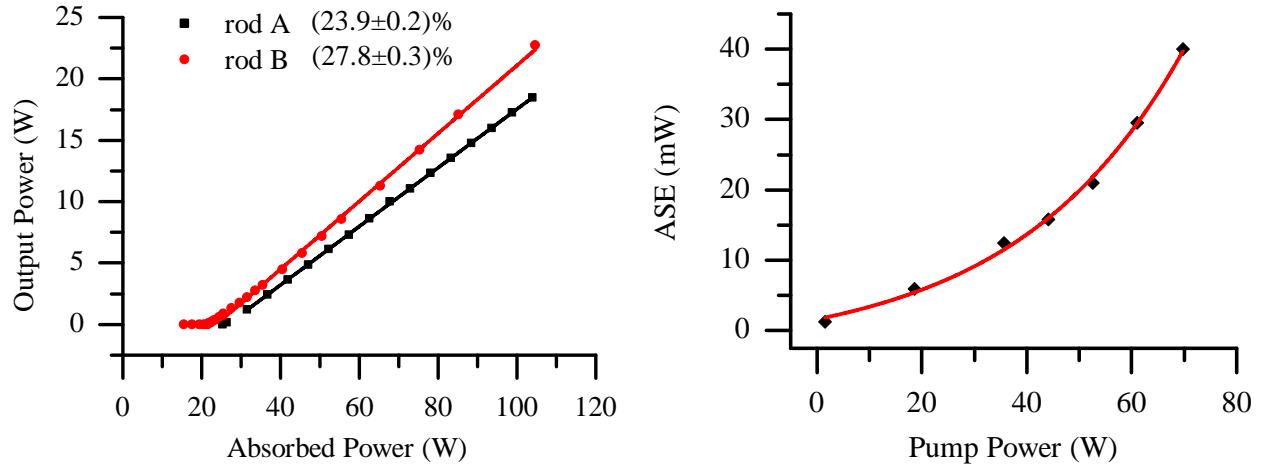
When lasing at 70W pump power, as shown in figure 3.7b, the spectra of the two rods show similar lasing peaks between 1900nm and 1950nm. Surprisingly the ASE does not disappear while lasing in either case. The ASE seems reduced in rodA but nearly unchanged in rodB. Interestingly the

investigation of the flexible PCF in [72] showed no ASE while lasing. The comparison indicates that the MFD might influence the ASE content while lasing. For large MFD the overlap of the fundamental mode with the doped region is smaller than for small MFD. Therefore a relatively large area remains undepleted by the lasing signal and could lead to the larger ASE content. However, the ASE power in all cases is at least 30dB smaller than the spectral power of the lasing signal.

3.3.2 *Lasing slope efficiencies*

The slope efficiencies achieved in lasing configuration were 23.9% and 27.8% for rodA and rodB, respectively and the plots are depicted in figure 3.8a. This is less than the 36% slope efficiency that we achieved using a flexible PCF with the same chemical composition in [72]. The differences in efficiency between the two rods is the result of the different cladding diameters, which makes pump coupling to rodA more difficult and less efficient. In agreement to this explanation the lasing threshold of rodA is 22W absorbed power, which is higher than the 17W for rodB. The absorbed power was calculated from the launched pump power by subtracting pump mirror losses and transmitted pump power. At 100W pump power the maximum output power was limited to 18W and 22W for rodA and rodB, respectively.

An additional experiment was carried out for rodB. The ASE output power over launched pump power was measured at the pump coupling side. The ASE power increases exponentially with pump power. For pump powers approaching 80W parasitic lasing occurred and the output power peaked to hundreds of mW. Below 80W pump power the ASE output power did not exceed 50mW. This result is very promising for pulsed amplification applications, since ASE is an important limiting factor for pulse energy scaling at low repetition rates (subsection 2.3.6). By extrapolating the observed ASE increase with pump power, we anticipate the ASE power does not exceed 150mW.



(a) Slope efficiency for lasing operation of rodA and rodB

(b) ASE slope of rodB, self lasing occurred at 80W pump power

Figure 3.8: Slope efficiency for lasing operation and ASE

3.3.3 Beam quality

M^2 -measurements were performed for both rods with a pyro-electric array camera (Ophir Pyro-Cam III) and revealed nearly diffraction limited beam qualities at 5W output power. The measurement results are depicted in figure 3.9. Even at highest output power, the beam quality was maintained. Our investigations showed that $M^2 < 1.3$ is achieved for output powers up to 18W/22W [76]. It is worth mentioning that readjustment of the cavity mirrors was necessary to achieve these results at highest pump powers. This is related to thermal effects in correspondence with the relatively low efficiency and high quantum defect in these thulium PCFs. Due to the smaller focal spot size of rodA compared to rodB and the limited length of the optical table it was not possible to use the same lenses for the M^2 -measurements. Hence, the beam waist measurements over position show a different divergence angle for rodA and rodB. The different focal positions of the horizontal and vertical beam waists are caused by astigmatism that was induced by the pump mirror at the output.

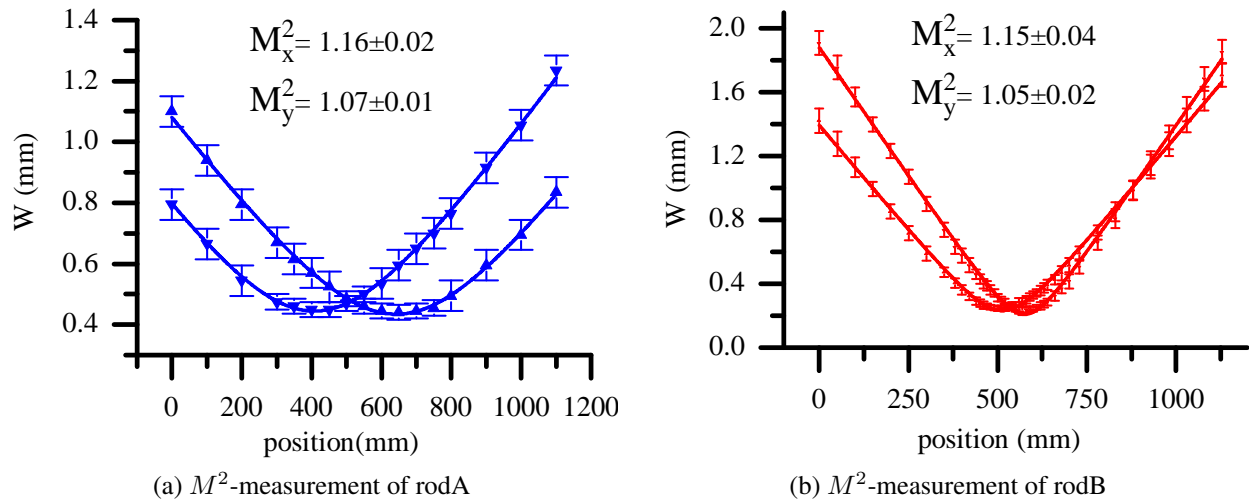


Figure 3.9: Investigation of beam quality. Both PCF rods show nearly diffraction limited beam quality

3.3.4 Wavelength tuning

In order to investigate the tunability of the lasing output in rodB, the high reflectivity mirror of the lasing setup figure 3.6 was replaced by a 600lines/mm gold reflection grating. As shown in figure 3.10b, the lasing wavelength was continuously tuned from 1810nm to 1990nm before parasitic lasing occurred.

The slope efficiencies for selected wavelengths were measured with respect to absorbed pump power and are plotted with respect to wavelength in figure 3.10a. In the same graph the corresponding lasing thresholds are depicted. The slope efficiencies are $> 20\%$ and relatively constant between 1830nm and 1970nm. Compared to the free lasing configuration the slope efficiency is reduced. This effect can partially be explained by different amplification at wavelengths according to the emission and absorption spectrum of the active material. In addition the reflection grating has a reflectivity of $\approx 90\%$ and additional losses are introduced to the cavity. At shorter or longer

wavelengths the slope efficiency drops significantly and the seeding wavelength for amplification should consequently be within this range. The lasing threshold has its minimum at 1920nm, in agreement with the center wavelength of the free lasing configuration figure 3.7b.

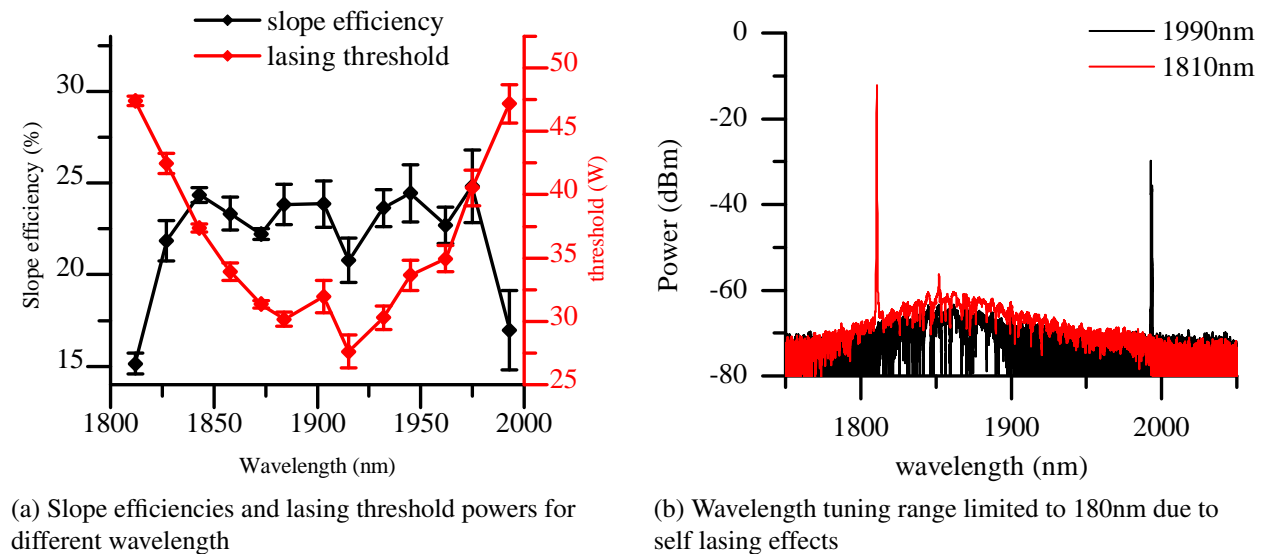


Figure 3.10: Investigation of the wavelength tunability in rodB

3.4 CW-amplification

The master oscillator power amplifier (MOPA) configuration enables much higher average output powers, peak powers and pulse energies than achievable from single oscillators. In addition the MOPA design allows for improved management of ASE generation and nonlinear effects by utilizing different fiber designs and fiber lengths in each amplification stage. However, the complexity is increased and the compactness of the laser system, that is often advertized as a major advantage of fiber lasers compared to e.g. solid state lasers, is significantly reduced. Noteworthy developments at $2\mu\text{m}$ wavelength comprise single amplification stage MOPA's with $> 150\text{W}$ CW output power [74], $> 100\text{W}$ polarized CW output power [77] and a four stage single frequency MOPA

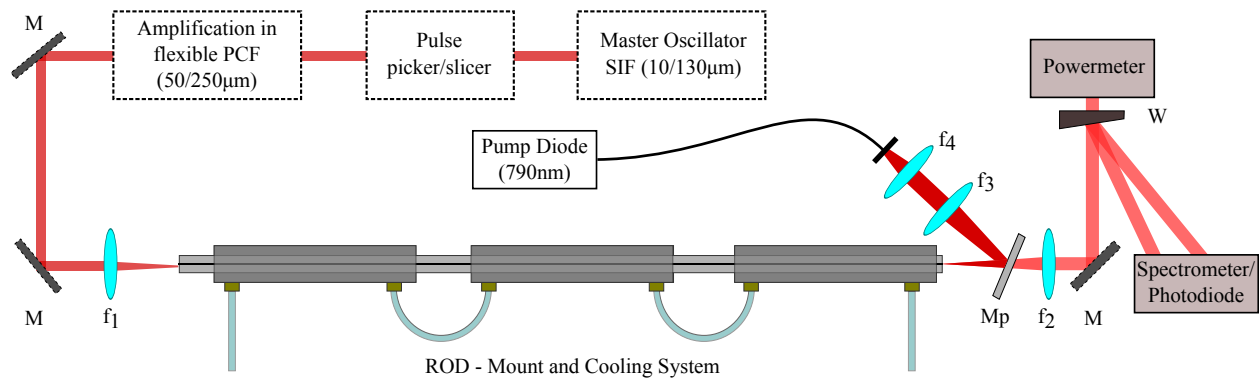
exceeding $600W$ average power [78]. The work presented here enabled medium average powers of $> 50W$ in a two stage MOPA configuration based on rodB as the selected final amplifier.

3.4.1 Experimental setup

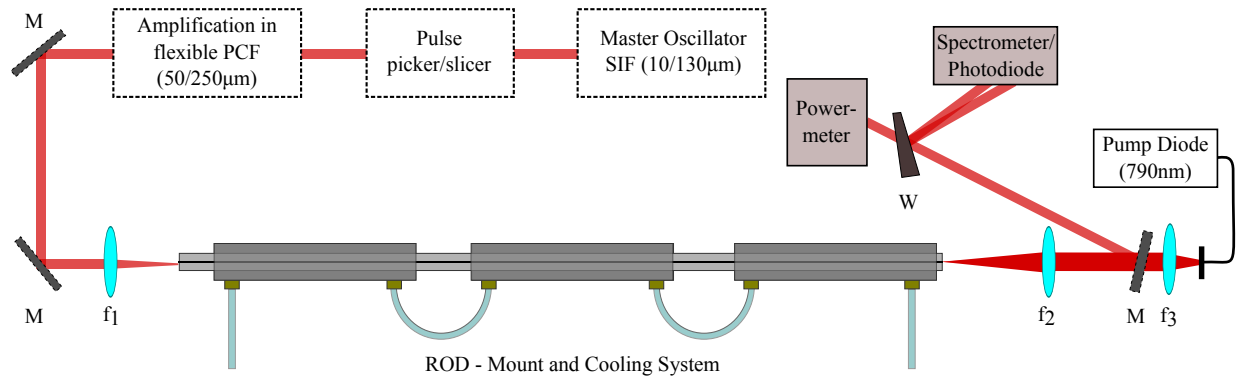
The setup for both, pulsed and CW-amplification, is depicted in figure 3.11. The signal for subsequent amplification is generated in a master oscillator containing a polarization maintaining step index fiber with $10\mu m$ core diameter as active medium, a reflection grating for wavelength tuning and an AOM (compare with section 2.1.3) for Q-switched operation. The master oscillator can be operated in CW mode. For pulsed operation an EOM (compare with section 2.1.4) is used for pulse slicing and picking, providing control over pulse duration and pulse repetition rate. The first amplification stage is a flexible PCF with $50\mu m$ core diameter and $\approx 2.7m$ length. The preamplified signal is then collimated at the PCF output by an Infrasil lens triplet with $25mm$ focal length and subsequently coupled into the final PCF-rod amplifier with another Infrasil lens triplet $f_1 = 25mm$. The amplified output signal is first collimated and then split into multiple beams by one or two glass wedges (depending on output power) with 4% Fresnel reflection. The reflected beams are used for temporal characterization and spectral analysis of the signal with a photodiode and a spectrometer, respectively. The transmitted beam is used for measurement of the average output power [20, 76].

Various experiments have been conducted with two pump diodes that required different pump coupling and signal collimation schemes. The $100W$ pump diode from DILAS utilized a multimode delivery fiber of $200\mu m$ core radius. Efficient pump coupling can be achieved with a 1:1 telescope for rodB with a pump core diameter of $220\mu m$ utilizing BK7 achromatic lenses $f_{3/4} = 100mm$, that are optimized for minimal pump light reflection (figure 3.11a). The pump signal at $793nm$ is reflected by a dichroic mirror, while the signal is transmitted and then collimated with a reflection

coated BK7 lens triplet $f_2 = 50mm$. Higher pump power requires larger delivery fibers with core diameters of $400\mu m$ and a 1:1 imaging system is not suitable for efficient pump coupling. To achieve sufficient pump coupling the focal length of f_3 needs to be reduced by at least a factor of 2. It was not possible to implement such a lens because lens mounts, mirror mounts and the cooling system introduce limitations on the minimal possible focal length in this pump scheme configuration.



(a) “Side pumping” configuration, suitable for 100W pump diode (DILAS) only. Separate lenses for pump telescope and signal output collimation ($f_2 = 50mm$).



(b) “Straight pumping” configuration, suitable for 100W (DILAS) or 300W (LIMO) pump diodes. Lens $f_2 = 40mm$ is simultaneously used for pump coupling and signal output collimation.

Figure 3.11: Setups for pulsed and CW-amplification

Figure 3.11b shows an alternative pump scheme. Here the aspheric lens $f_2 = 40mm$ for signal collimation is simultaneously used for pump coupling. The advantages of this pump scheme are higher pump powers of up to 300W (LIMO pump diode), less astigmatism in the signal beam

and more efficient pump coupling. However, no such lenses are available off the shelf and it is hard to find a lens that has anti-reflection coating for both, pump light (793nm) and signal light ($2\mu m$). The lens chosen here is equipped with an anti-reflection coating ($650nm - 1050nm$) and shows nearly no absorption at 793nm. It is S-LAH64 based and absorbs $\approx 5\%$ at $2\mu m$ wavelength. A major disadvantage is the potentially lower threshold for parasitic lasing since the lens has no anti-reflection coating at the signal wavelength.

3.4.2 Characteristics of the CW-seed source

The master oscillator and the preamplification stage have been characterized and discussed in great detail in the PhD thesis of Pankaj Kadwani [5] and a similar discussion is not within the scope of this work. This subsection provides details on the spectral and temporal characteristics of the master oscillator and the preamplifier in CW-operation. Moreover the maximum achievable output power is of interest for seeding the final PCF rod amplifier because parasitic lasing can be effectively avoided with sufficient seed powers.

The schematic setup of the seed source is depicted in figure 3.12. The active medium of the master oscillator consists of a polarization maintaining step index fiber with $10\mu m$ core and $130\mu m$ cladding diameter [79]. It is spliced to a beam combiner that connects to a 35W pump diode at 790nm. The cavity consists of a reflection grating for wavelength tuning and the 4% Fresnel reflection of the fiber end facet and can be Q-switched by an acousto optical modulator (AOM). The AOM can be operated in CW-mode. The oscillator output is directed through an electro optical modulator (EOM) that can be utilized as a pulse slicer and picker. This device is turned off in CW-mode. After passing through a Faraday isolator the beam is eventually coupled into the preamplifier fiber, a flexible polarization maintaining PCF with $50\mu m$ core diameter and $250\mu m$ cladding diameter [79]. The implemented Faraday isolators prevent backwards propagating light

to affect the amplifier or oscillator. It is worth mentioning that the PCF fiber used here was doped with 3.5wt.%. Part of the characterization in [5] was done at 2.5wt.% doping concentration leading to higher output powers and better performance.

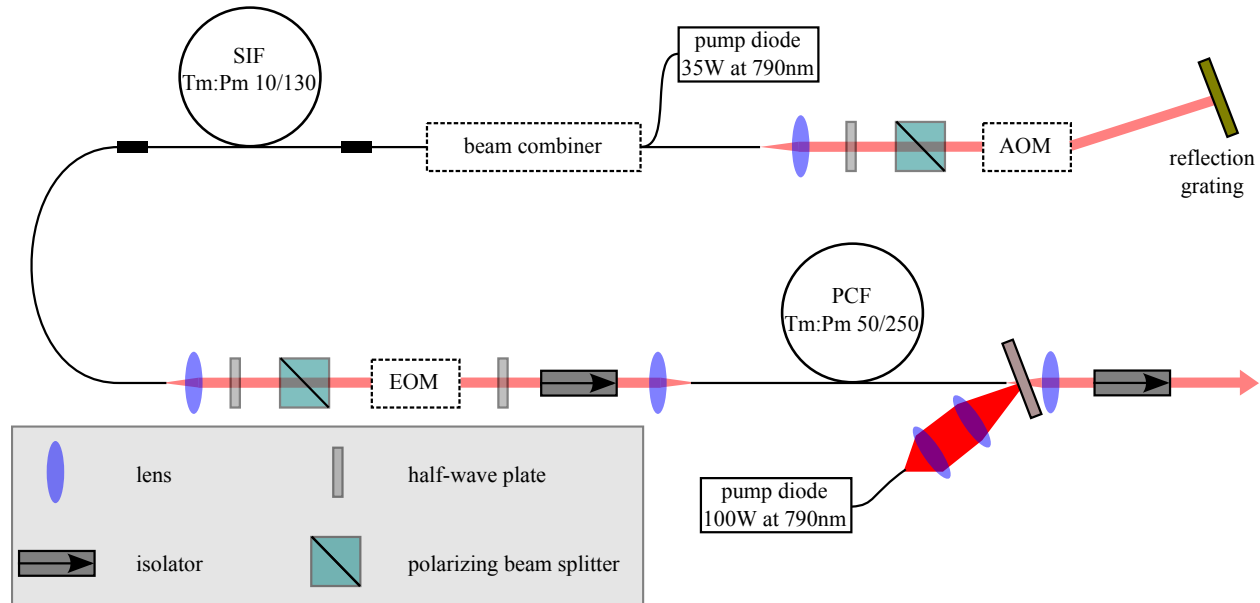


Figure 3.12: Schematic Setup of the master oscillator and preamplifier. The AOM can be operated in CW-mode or pulsed mode. The EOM is used as a slicer/ pulse picker and is turned off for CW-operation

The master oscillator was operated at 650mW CW output power and produced a Gaussian beam with a spectral width of only 0.3nm (10dB width). The measured spectrum and beam profile are shown in figure 3.13a. After passing through EOM and isolator 450mW of CW-power were coupled into the flexible PCF preamplifier. The maximum CW-seed output used for the following CW-amplification experiments was 4W. Figure 3.13b shows the spectrum and the beam shape at 4W CW-average power. The 10dB linewidth is still below 1nm.

An interesting observation was made when the temporal evolution of the CW-signal was investigated with a photodiode. Although the AOM was switched to CW mode, pulses with a repetition rate of $\approx 1.6MHz$ and $\approx 20ns$ pulse duration were formed in the cavity. Measurements of this

self pulsation are shown in figure 3.14. The pulses were not stable in terms of peak intensity as can be seen in figure 3.14a. The stability was strongly dependent on pump power and cavity alignment. This could be self-pulses from the three-level nature of thulium or might involve soliton formation. In case of soliton formation the anomalous dispersion of the silica glass in combination with self phase modulation lead to a stable solution in the fiber cavity.

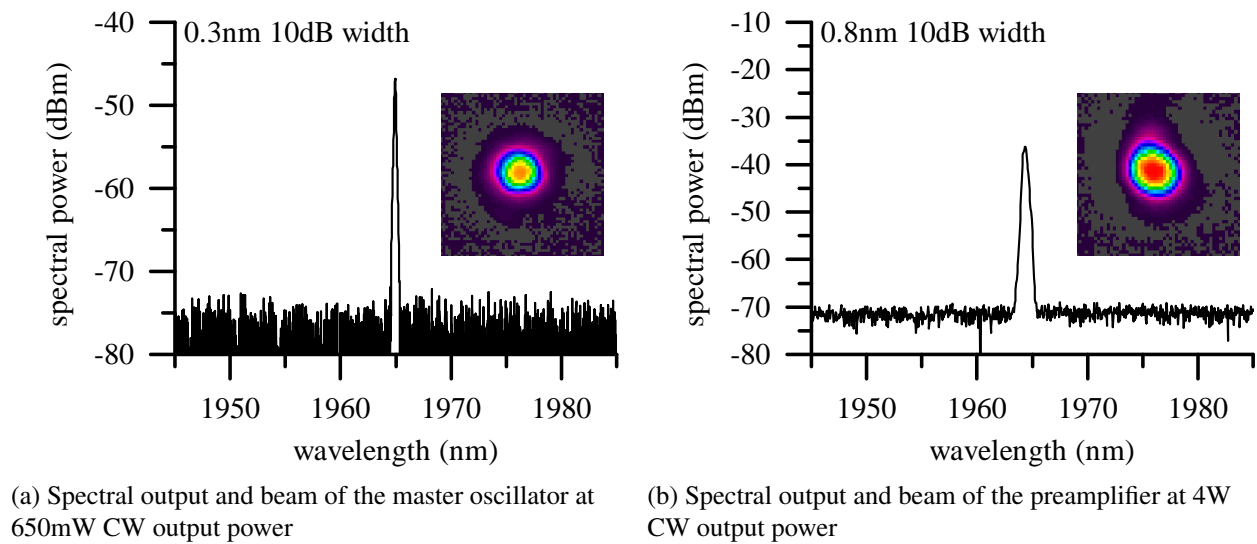
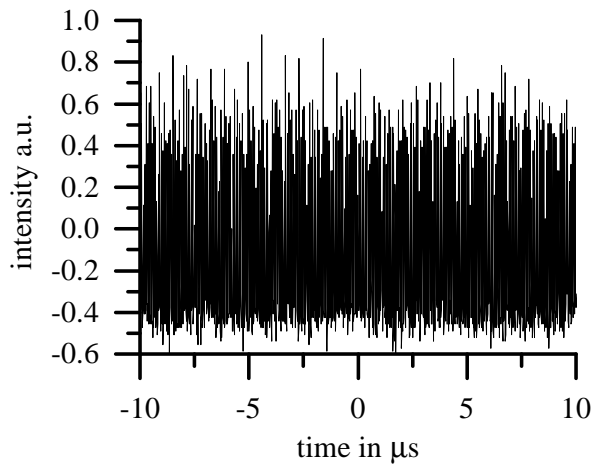
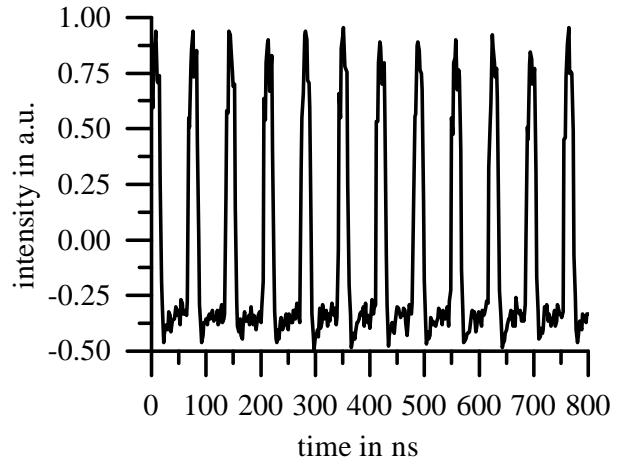


Figure 3.13: CW-performance of the seed system

In conclusion we found that the seed source is not CW and shows self pulsation. The repetition rate of this self pulsation is in the order of MHz. At this repetition rate the performance of subsequent amplifiers is most likely very close to the actual CW-performance. Thus, in the following this type of performance is still called CW-signal or CW-amplification.



(a) Measurement of self pulsation shows peak intensity fluctuations over time



(b) The repetition rate is approximately 1.6 MHz with pulse durations of ≈ 20 ns

Figure 3.14: Self pulsation occurs in master oscillator when AOM is set to CW mode

3.4.3 Measurement of the mode field diameter

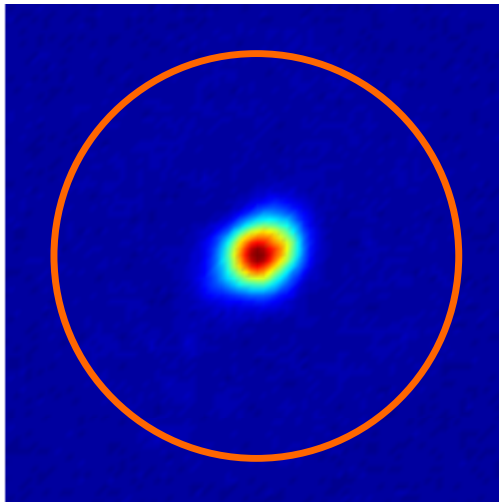
Before the CW-amplification experiments were conducted in the final amplifier, it was of interest to find the actual mode field diameter (MFD) of the PCF rod. An easy way to find the MFD is to couple light into the fiber rod fundamental mode and image the beam output with sufficient magnification (e.g. 20x). Since the pump core diameter is usually known, it can be used as a reference. By slightly detuning the input coupling, it is possible to excite significant amount of light in the pump core. The pump core diameter was determined by counting the camera pixels illuminated in a single line that passes the center of the fiber core. Using the known pump core diameter, the actual image pixel size can be determined.

The measurement was done for rodB only. The beam image with the determined pump core diameter are shown in figure 3.15a. The beam was fitted in Matlab by using a Gaussian function and the MFD's correspond to $1/e^2$ of the intensity. The fits are shown in figure 3.15b. In order to

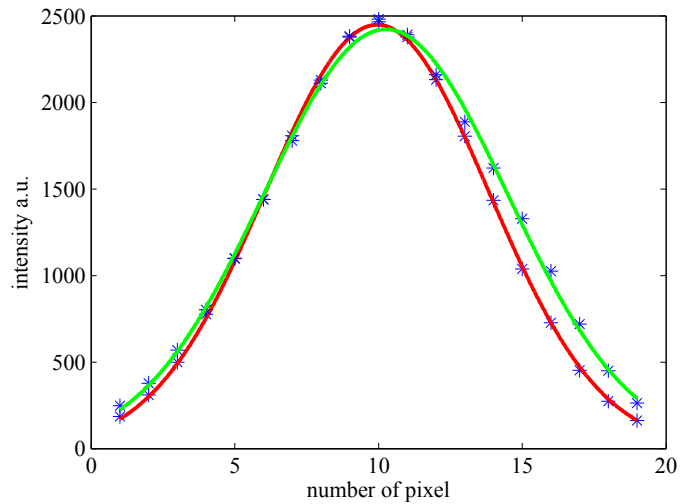
account for small aberrations of the imaging, the image pixel size was calculated for horizontal (x) and vertical (y) direction. The MFD was found to be $\approx 50\mu m$ and appears slightly smaller than the theoretical prediction of $56\mu m$ given in 3.1. Since the measurement was carried out without pumping the rod, mode field shrinking due to thermally induced waveguide changes did not occur. However, it is unclear if interference of the fundamental mode with higher order modes (HOM) could have reduced the actual beam size. Even if the power content in HOM's is small, they can still significantly affect the actual beam shape.

$$1pixel_x \approx (3.10 \pm 0.06)\mu m \qquad 1pixel_y \approx (2.93 \pm 0.05)\mu m \qquad (3.1)$$

$$MFD_x = (48.1 \pm 3.5)\mu m \qquad MFD_y = (49.7 \pm 4.5)\mu m \qquad (3.2)$$



(a) Unamplified beam profile of rodB. The orange circle represents the size of the pump core



(b) Plot and Gaussian fit of beam profile in horizontal (red) and vertical (green) orientation

Figure 3.15: Measurement of the mode field diameter without amplification

3.4.4 CW-amplification performance

The slope efficiencies as well as the beam shape evolution with output power for CW-amplification were characterized for both rods. A M^2 measurement was only carried out for rodB. In the following the results are separately presented for both rods as final amplifiers.

CW-Amplification in rodA

The CW-amplification experiment with rodA was carried out in straight pumping configuration (figure 3.11b) with a 100mm:40mm telescope for pump coupling and a maximum pump power of 100W at 793nm (DILAS). Higher pump powers could not be coupled into the rod, because proper aspheric lenses are not commercially available to focus the 400 μm delivery fiber diameter to the rather small pump core (180 μm).

The slope efficiencies were measured for different seed powers while monitoring the spectral characteristic and beam shape of the output. The results are shown in figures 3.16 and 3.17. The maximum output power achieved was $> 18\text{W}$ for 90W launched pump power. The measured spectrum (figure 3.16b) looks clean and shows no sign of nonlinear effects or ASE. The 10dB spectral width is smaller than 1nm. The slope efficiency increases with seed power and is $\approx 19\%$ at highest seed input. Compared to the CW-lasing result of $\approx 24\%$ the slope efficiency is noticeably reduced. The beam quality was not investigated in detail, e.g. no M^2 characterization was performed. However, images of the beam shape were recorded for various output powers. The intensity distribution fluctuates when the pump input power is changed. Those fluctuations can be compensated by adjustment of the seed coupling. The fluctuations did not severely influence the achievable output power for a set pump power. The beam shape evolution for different output powers depicted in figure 3.17 shows relatively strong fluctuations. The coupling was not optimized

after increasing the pump power. Interestingly the beam deformations seem not related to the total output power, because the beam quality randomly improves or degrades while changing the pump power. For example, it can be seen that at highest output power the beam shape looks quite Gaussian again, although the beam quality seemed to degrade before. Possibly the deformations are the result of thermally induced waveguide changes. Different pump powers cause a different amount of heat to be deposited in the fiber and the index of refraction changes with temperature. This index change affects the guiding properties of the fiber and might lead to guidance of higher order modes. Another possible explanation is thermal lensing of the fiber tip on the pump side. The radial temperature gradient is mimicked by a refractive index change via the thermo-optic effect [23]. Thus, the higher temperature in the core center causes a higher positive index change (in silica) than at the core-cladding transition and the radial index distribution acts like a positive lens.

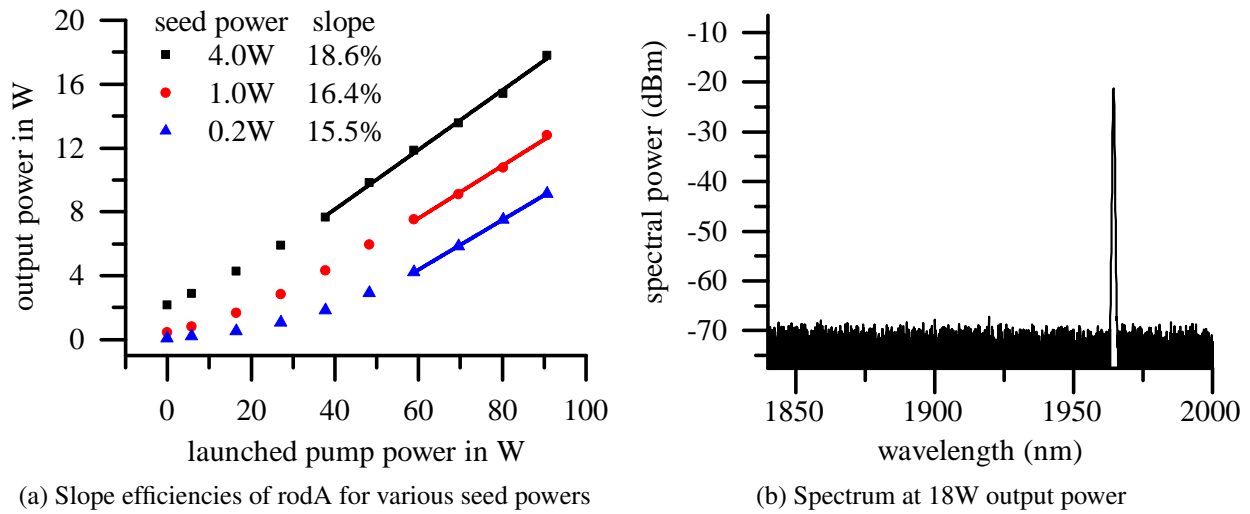


Figure 3.16: CW-amplification performance of rodB with output powers of $> 18W$

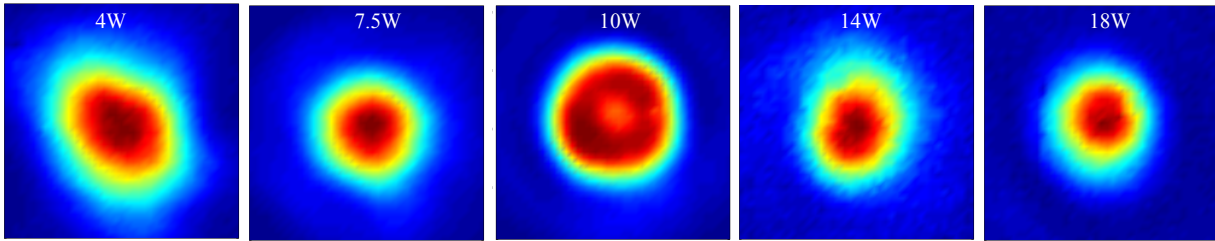


Figure 3.17: Collimated beam profiles for various output powers. The beam quality fluctuates with changing pump powers.

CW-Amplification in rodB

The CW amplification with rodB was realized with both pump diodes. First the 100W DILAS pump diode was utilized in side pumping configuration with a 100mm:100mm coupling telescope, as shown in figure 3.11a. Subsequently the 300W LIMO pump diode was implemented in straight pumping configuration as depicted in figure 3.11b with a 100mm:40mm telescope, allowing to focus a 400 μ m delivery fiber diameter down to < 220 μ m pump core diameter.

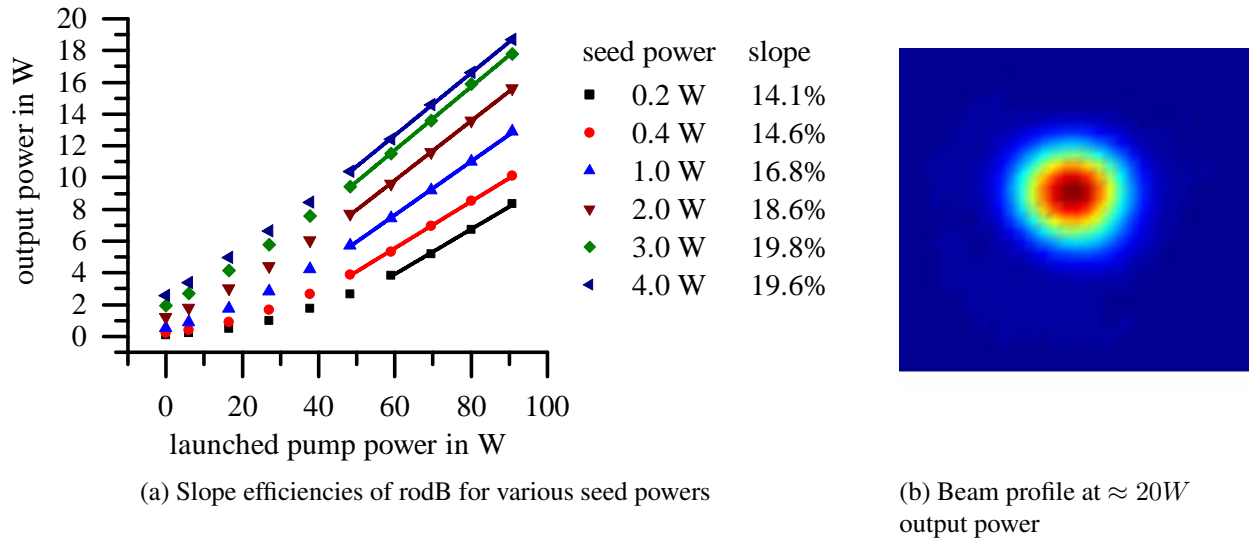


Figure 3.18: CW-amplification performance of rodB with output powers of 20W and excellent beam quality [71]

The results based on the 100W DILAS pump diode are presented in the following paragraphs. In figure 3.18a the output powers with respect to pump power are plotted for various seed powers. The corresponding slope efficiencies were determined with linear fits and are summarized in figure 3.19a. The maximum output power of $\approx 19W$ was achieved with an input seeding power of 4W with excellent beam quality, as shown in figure 3.18b. Three things can be concluded from these systematic measurements. First the slope efficiency increases with seeding power from 14% to almost 20% and remains quite constant for seed powers larger than 2W. The slope efficiency decreased noticeably compared to the measured free lasing slope efficiency of 27%. Furthermore the gain reduces drastically from 16dB (amplification factor ≈ 40) at 200mW seed power to roughly 6dB (amplification factor ≈ 5) at 4W seed power.

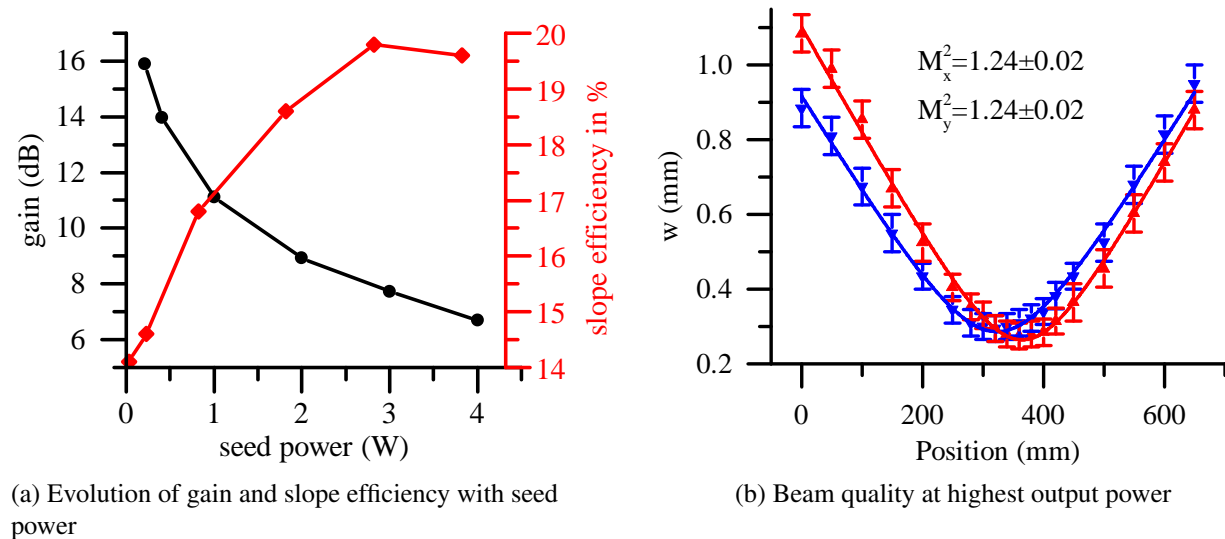


Figure 3.19: Characterization of rodB as the final amplification stage

The beam profile did fluctuate slightly when the pump power was changed. Strong deformations of the beam shape, that occurred for rodA (compare figure 3.17), were not observed at these pump powers. These small deformations can easily be compensated with a change of coupling conditions for a specific pump power and are very likely a result of the changing thermal load. In fact, with

effort to improve the beam quality by changing the coupling conditions, the rod produces nearly diffraction limited beam quality for all pump powers with $M^2 < 1.3$. This is in agreement with the results found in the CW-lasing characterization. Figure 3.19b shows a M^2 -measurement at $\approx 20W$ output power.

The following CW-amplification results were achieved when utilizing the 300W LIMO pump diode. Figure 3.20a depicts the achieved output powers over launched pump power when seeding the rodB with 6W CW-average power. The output power evolution with increasing pump power is linear up to 200W pump power and 40W output power. Within this pump power range the slope efficiency is $\approx 24\%$. Compared to the slope efficiencies achieved with the 100W DILAS pump diode this result is much closer to the slope efficiency in free lasing operation ($\approx 27\%$). Most likely the straight pumping configuration, as well as the different pump optics and the different pump source enabled higher slope efficiency.

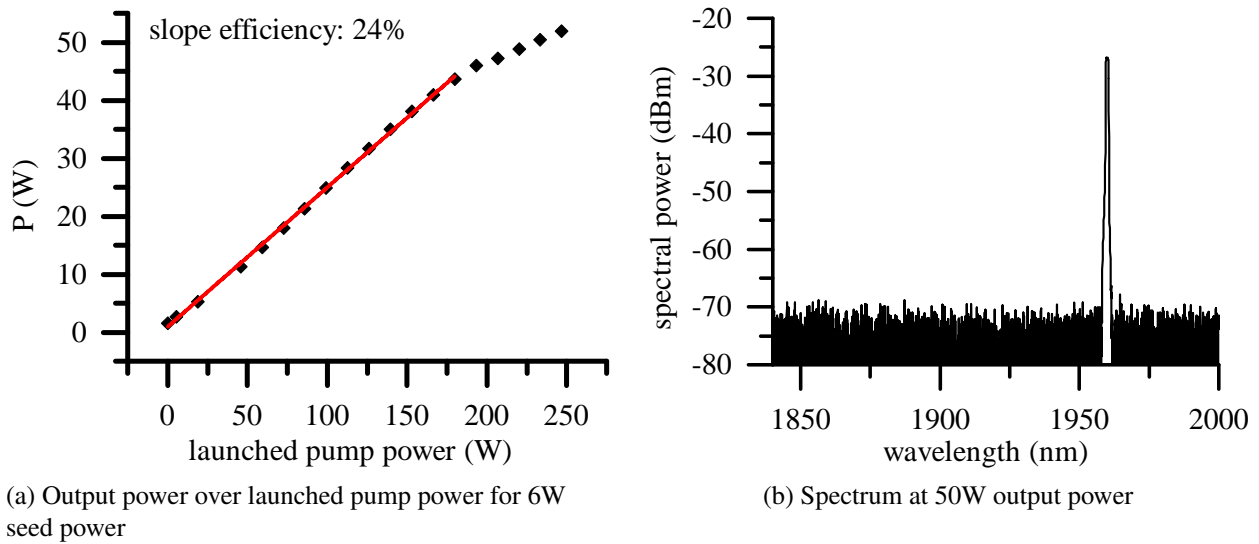


Figure 3.20: Amplification in rodB with more than 250W pump power

The maximum output power was limited by parasitic lasing to 52W at 250W pump power. It is worth mentioning that this CW-amplification measurement was performed after pulsed amplification experiments, where the rod end facet was damaged multiple times. The rod had to be repaired several times by “hand”-cleaving only. Eventually the length of the rod was reduced from 1.36m to roughly 1.0m. The end facets were not sealed or angle polished and parasitic lasing as well as contamination were more likely to occur. At highest output power the spectrum, as shown in figure 3.20b, looked clean without any indication of strong ASE or nonlinear effects.

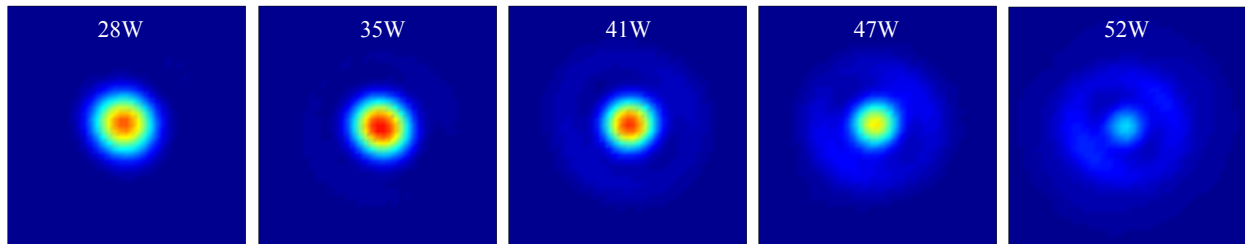


Figure 3.21: Beam profiles for various output powers. The beam quality starts to degrade for output powers $> 30W$ and degrades drastically for output powers $> 40W$

As mentioned before the slope efficiency was significantly reduced when 40W output power was exceeded. This observation coincides with a degradation of beam quality, as shown in figure 3.21. The beam degradation has a different character than the deformations observed in rodA (compare figure 3.17). In the case of rodA and at much lower output powers the beam shape seemed to deform randomly relative to pump power at any power level. In this case the beam deformation is proportional to pump power. First signs of beam degradation can be observed for output powers $> 30W$, when a weak ring appears around the central Gaussian like lobe.

The beam profile is reminiscent of the first higher order mode shown in subsection 3.1. The power of the ring increases more rapidly compared to the central Gaussian like mode when pushing the output power beyond 40W. One possible explanation is transverse spatial hole burning, meaning that the central part of the beam sees reduced gain due to saturation, while the much weaker

outer part of the beam is still strongly amplified. Consequently the slope efficiency is only partly reduced due to spatial transverse saturation effects. However, when the experiment was conducted, the coupling conditions were changed at the rod input and no significant change of the beam profile was observed. Multiple modes lead to a beam profile, which is determined by interference. When the input coupling is altered, the phase accumulation and power in the fiber, as well as the modal power content is changed and the beam profile should deform as well. Instead the stability of the output profile suggests, that the HOM content is rather small. Thus, it is possible that the beam profile is changed by thermal lensing effects, especially at the fiber output facet. Since the fiber core is hottest at the center, the thermal lens is stronger in the center. Consequently the central part of the Gaussian like beam is more focused than the wings. In combination with interference effects this could result in the ring like pattern observed. However, this explanation leaves unclear, why the slope efficiency was drastically reduced, when the beam deformation started to be clearly visible. Possibly the pump power level is close to saturation of the fiber. However, slow roll off is an expected manifestation of gain saturation, rather than a sudden drop of slope efficiency.

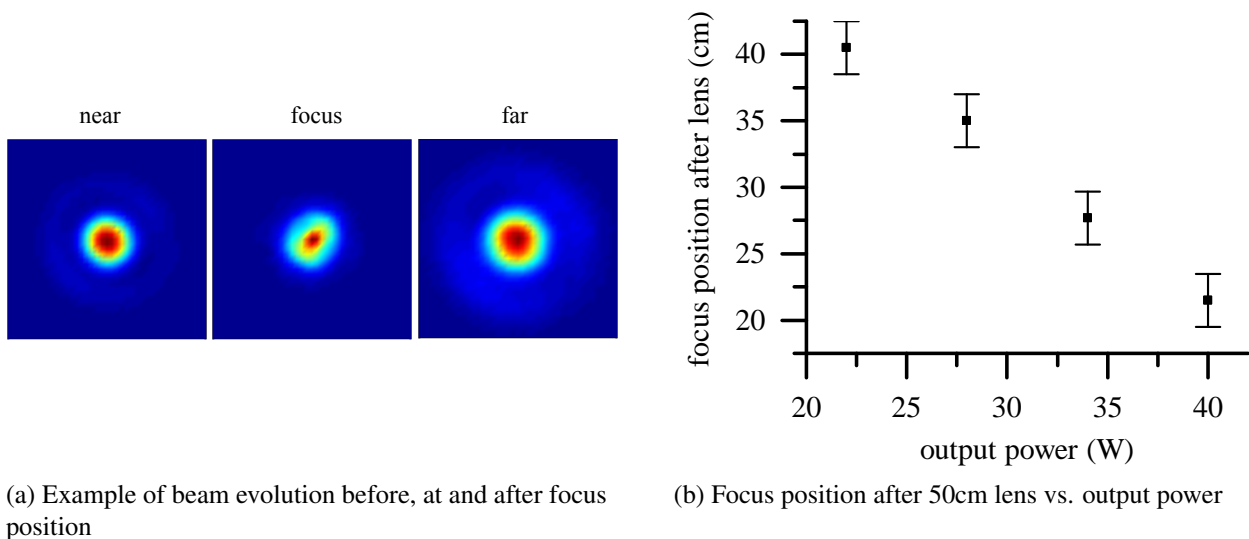


Figure 3.22: Thermal lensing for output powers $> 20W$

All the beam deformations were recorded with collimated beam and similar camera positions for all images. An additional measurement was done later. Instead of looking at the collimated beam, the beam was focused with a 50cm lens and then recorded right behind the lens (near), in the focus and after the focus (far). An example of all images is given in figure 3.22a at 40W output power. We found that the focus position is significantly shifted towards the focusing lens as depicted in figure 3.22b. This is an indication that thermal lensing caused strong focusing at high powers.

3.5 Pulsed amplification

Fiber lasers generally offer relatively high average power with high spatial beam quality and efficient thermal management. Pulsed laser performance is typically constrained by energy extraction and peak power limitations. High peak powers can be achieved by decreasing the pulse duration or by reducing the pulse repetition rate, if the maximum achievable average power is reached. Low repetition rate increases the energy extraction per pulse in the amplifier, if the time between subsequent pulses is smaller or in the order of the upper level life time. For very low repetition rates the energy extraction saturates and ASE builds up between the pulses instead. Nonlinear effects, such as SPM, FWM, Raman- and Brillouin-scattering, as well as fiber damage represent serious peak power limitations and have been discussed in detail in subsection 2.3.

Thulium as the dopant in active fibers has a twofold advantage. First, the $2\mu\text{m}$ wavelength compared to $1\mu\text{m}$ wavelength allows theoretically for twice the mode field diameter while preserving single mode behavior. This alone may enable peak power scaling in thulium doped fiber lasers beyond ytterbium doped systems, since nonlinear effects in the fiber scale with mode field area. Second, nonlinear effects such as stimulated Raman-scattering and self-focusing are inverse proportional to the wavelength, stressing the potential of thulium doped fiber lasers to generate peak powers in the fiber beyond 10MW.

The experimental setup for the generation of high peak power and multi mJ pulse energy ns-pulses is similar to the CW-amplification setup presented in 3.5 and is shown in figure 3.11a. Compared to ytterbium based fiber lasers, thulium based systems reach significantly lower average power and thermal management is more important. Nevertheless, by reducing the pulse repetition rate and pulse duration it is possible to generate several 100kW peak power at average powers in the order of 10W [20, 4].

Direct Q-switching of a laser cavity is the easiest way to generate ns-pulses with a doped fiber as active medium. A rod-type ytterbium-doped PCF with $70\mu m$ core diameter produced sub-10ns pulses with up to 2mJ pulse energy when actively Q-switched with an AOM [80]. The MOPA configuration enabled further power and energy scaling. ytterbium based systems incorporating very large MFA PCF rods have generated ns-pulses at near diffraction limited beam quality with more than 4MW peak power [3] and 26mJ pulse energy [81]. To date, some of the most notable achievements are the generation of Q-switched ns-pulses with up to $270\mu J$ energy with a thulium-doped double-clad silica fiber [62] and a high average power Q-switched Tm-doped large pitch fiber oscillator with 2.4mJ pulse energy [4]. A thulium based MOPA all fiber single frequency system produced ns-pulses with over 78kW peak power [14]. In this work we achieved MW-level peak power with a two stage MOPA and a rod type PCF as the final amplifier. The results have recently been published in Optics Letters [20].

3.5.1 Characteristics of the pulsed seed source

The AOM was set to pulsed operation at 20kHz repetition rate. With this setting the master oscillator produced polarized $\approx 100ns$ (FWHM) pulses at an average power of 670mW, $> 30\mu J$ pulse energy and 335W peak power. The pulse shape as well as the spectrum at this performance level are depicted in figure 3.23. The 10dB bandwidth of the output at this power level was 0.7nm

and is increased compared to the CW-case shown in figure 3.13a. Higher output peak powers are possible but lead to broader spectra and ultimately to instability of the output signal due to self phase modulation and modulation instability.

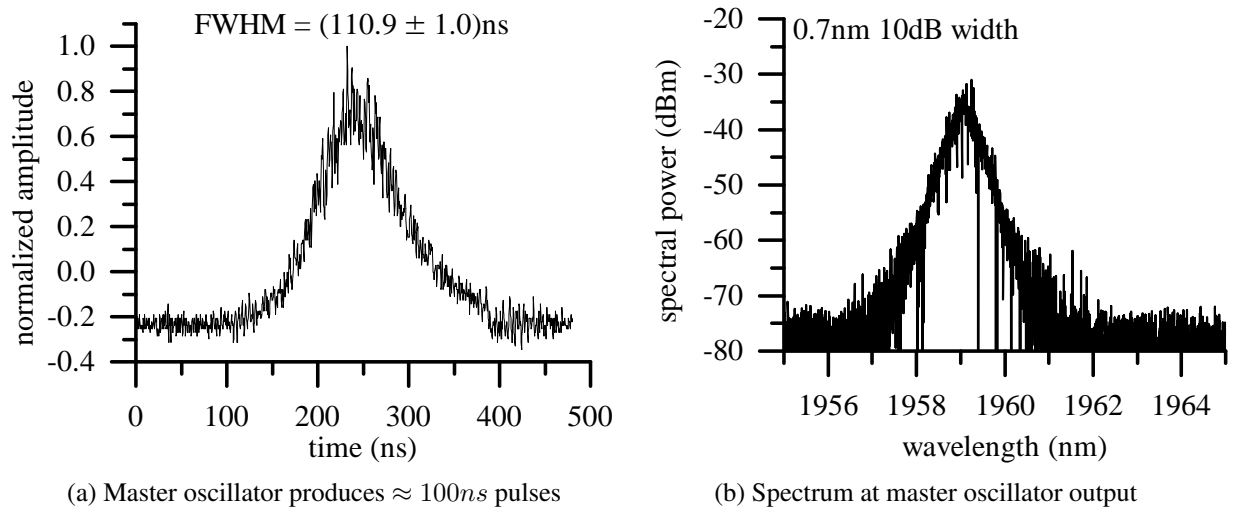


Figure 3.23: Characteristics of the master oscillator at 670mW average output power and 20kHz repetition rate

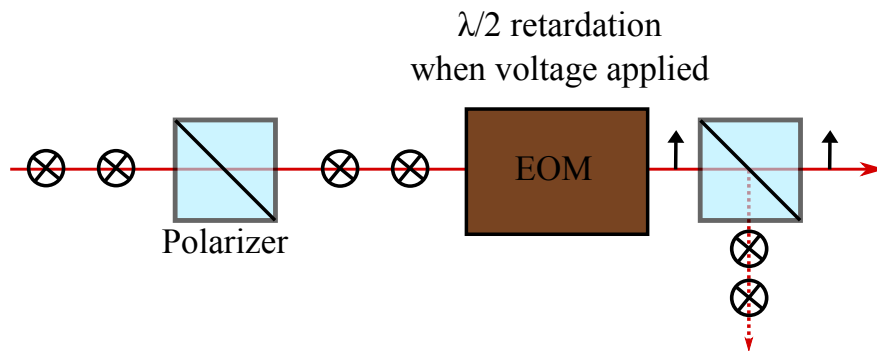


Figure 3.24: EOM utilized as pulse slicer and pulse picker enabling tunability of pulse duration between 6ns-100ns and pulse repetition rates between 1kHz-20kHz.

To achieve control over both, repetition rate and pulse duration, an EOM (compare with subsection 2.1.4) was utilized as a pulse slicer and picker. The working principle is schematically shown in

figure 3.24. The EOM rotates the linear polarized input by 90° when voltage is applied and the signal passes through the subsequent polarizing beam cube and is coupled into the flexible PCF amplifier. When no voltage is applied, the signal is reflected by the beam cube and absorbed by a beam blocker. Repetition rates below 1kHz and pulse durations as low as 6ns can be generated with this technique.

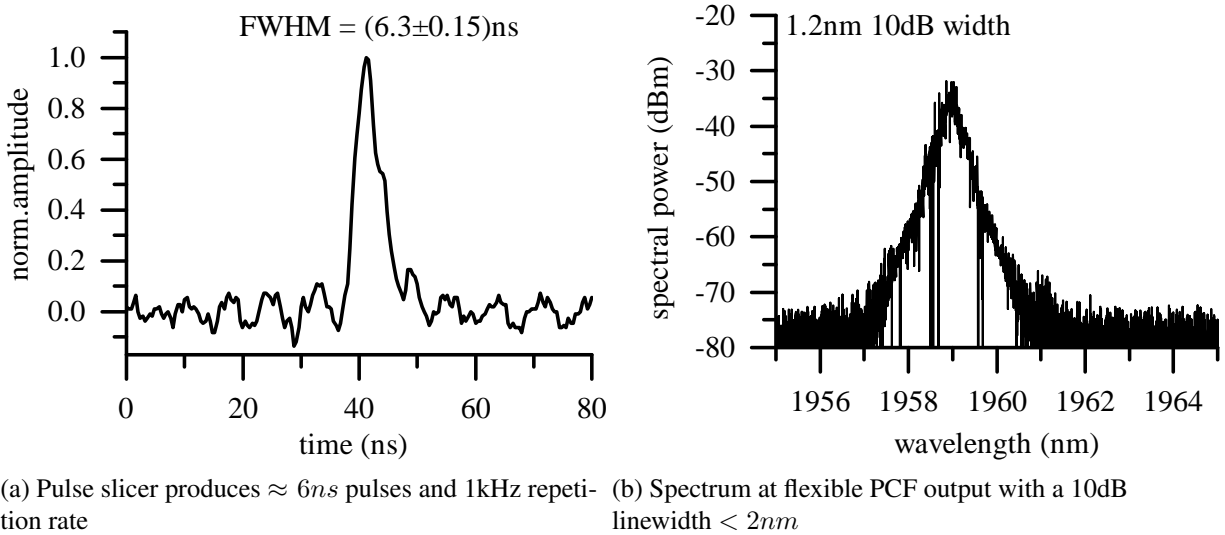


Figure 3.25: Characteristics of the flexible PCF output at 250mW average output power and 1kHz repetition rate

The seed signal was varied in repetition rate and pulse duration in order to characterize the effects on the performance of the final rod amplifier. One amplification experiment was carried out at 1kHz repetition rate and was optimized to achieve maximum peak power in the final amplification stage with rodB. The flexible PCF amplification stage enabled amplification of 6ns pulses at 1kHz to a maximum of 500mW average power. This corresponds to $\approx 500\mu\text{J}$ pulse energy and 80kW peak power. However, the spectrum becomes significantly broadened beyond 2nm (10dB width) and small amounts of ASE are noticeable at the output. In order to minimize ASE and to achieve narrow linewidth of the signal, the output average power was reduced to 250mW ($\approx 40\text{kW}$ peak

power). Another EOM was implemented as a pulse picker after the flexible PCF output in order to characterize ASE content between subsequent pulses. The output was basically free from ASE at an average power level of 250mW. The EOM was removed before the final amplification experiment was conducted, because the additional optical elements (beam cubes and EOM) caused significant losses in the signal ($\approx 20\%$). Spectrum and pulse shape at this performance level are depicted in figure 3.25.

3.5.2 Amplification to MW-level peak power

Pulsed amplification experiments were conducted with rodB. The larger mode field diameter of $\approx 56\mu m$ for rodB compared to $46\mu m$ for rodA was chosen for the generation of high peak powers. The pulsed amplification in rodB was carried out for 20kHz/10kHz at 100ns pulse duration and 10kHz/1kHz at 6ns pulse duration. The respective final output powers and slope efficiencies are depicted in figure 3.26.

The highest average output power of $\approx 20W$ was achieved at 20kHz repetition rate and 100ns pulse duration with 4W seed power. The determined slope efficiency is smaller than 20%, which was similar in CW-operation at the same average input power. At 10kHz and 100ns pulse duration the seed power was 2W and the slope efficiency dropped even more significantly compared to the equivalent CW seed power with a slope efficiency of 16.8%. It is clear that both, reduction in seed power and the reduction in duty cycle affect slope efficiency. The input pulse energy for these experiments was kept at $200\mu J$ and indicates that the primary effect on slope efficiency was the duty cycle of the amplifier.

The amplification experiments at 6ns pulse duration revealed an even stronger reduction of slope efficiency. At 10kHz repetition rate the seed power was 660mW. At this average power level a slope efficiency of $\approx 15.5\%$ can be expected in CW-operation (compare with figure 3.19a). The

achieved slope efficiency of $\approx 11\%$ is the result of both, pulse repetition and significantly shorter pulse duration. Similar arguments account for the relatively small slope efficiency of $\approx 9\%$ at 1kHz.

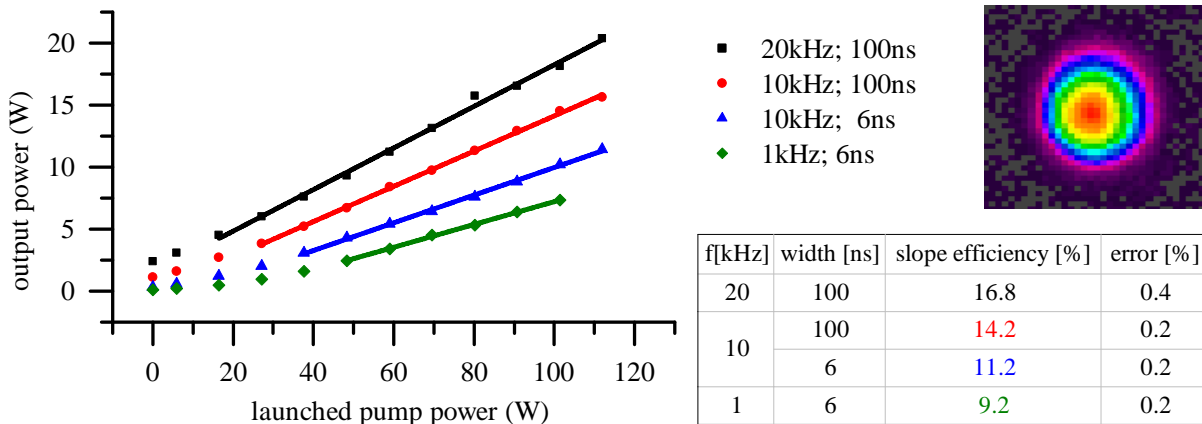


Figure 3.26: Output power over launched pump power for various repetition rates and pulse durations. Also shown are the corresponding slope efficiencies and a beam image at 1kHz, 6.5ns with 7.3W average power [20].

Although the slope efficiency and average output power reduce noticeably with lower repetition rate, the highest pulse energies are achieved at relatively low repetition rates of ($\approx 1kHz$). At this repetition rate the time gap between the pulses is already larger than the upper state lifetime and the build up of ASE must be considered. Moreover possible ASE seed content can significantly reduce the energy in the amplified pulse. Consequently the seed signal needs to be of high quality and should ideally contain pulses without any CW-content. The short length of the fiber rod is of advantage, since the ASE threshold scales with fiber length. For a given pulse energy the peak power can be maximized by decreasing the pulse duration. In this experiment high peak powers were generated at 1kHz and 10kHz with $\approx 6ns$ pulse duration.

At 10kHz repetition rate a maximum average output power of 10.2W was achieved. Assuming Gaussian pulse shape and 5% cladding light this corresponds to a pulse energy and peak power of

$\approx 0.9mJ$ and $\approx 140kW$, respectively. An even more conservative calculation for 1kHz repetition rate results in a record peak power of $\approx 890kW$, by assuming 10% cladding light, 97% of the energy in the pulses and 500mW ASE content in the output signal. It must be pointed out here, that the amount of cladding light and the ASE content are strongly overestimated in this calculation. However, a pulse energy measurement was not performed when conducting these experiments and the peak power calculation is an estimation only [20]. Nevertheless, this peak power result represents a tremendous increase of peak power compared to previous thulium based fiber lasers.

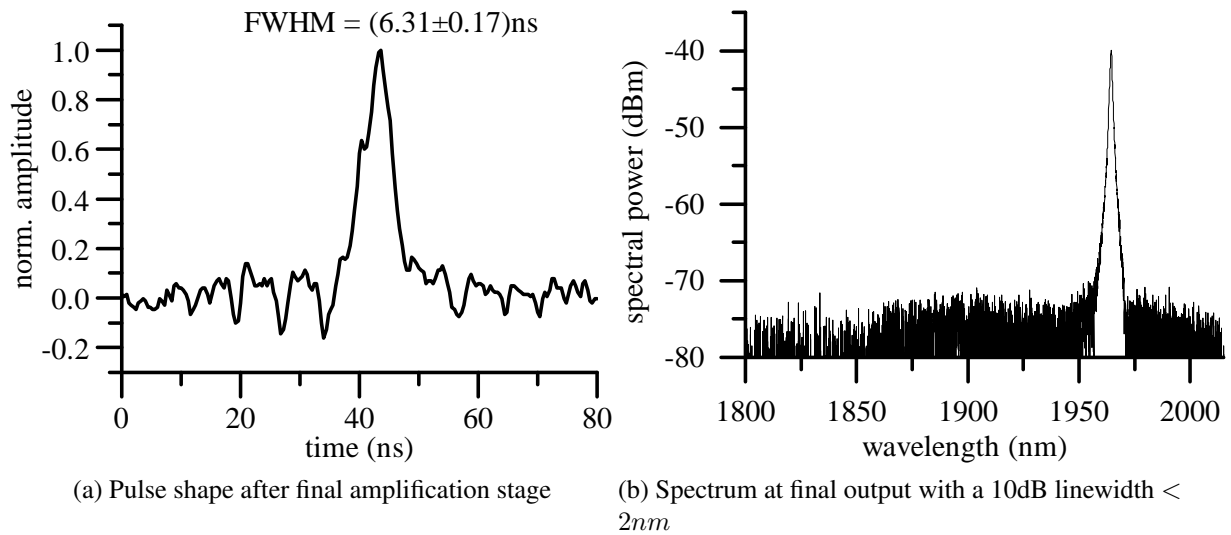


Figure 3.27: Characteristics of the final amplifier output at 7.3W average output power and 1kHz repetition rate

The pulse shape and spectrum at 1kHz repetition rate and highest output power are depicted in figure 3.27. The pulse duration and shape were not significantly changed compared to the seed input. The temporal profile of the pulse is accompanied with a modulation, which is associated with electrical noise from the high voltage driver for the pulse slicer and not the optical pulse. The spectrum shows no indication of nonlinear effects or significant ASE.

All the presented results strongly indicate, but do not prove, the calculated peak powers. In order to verify the peak powers, better characterization of the output signal is necessary. One possibility is the utilization of an energy meter for direct pulse energy measurements. Furthermore, the energy confinement in the pulses can be experimentally investigated with an EOM as pulse picker. These measurements were started and could not be completed because the rod end facet at the pump side was damaged. The damage occurred at much lower peak power of ($\approx 200kW$). As discussed in section 2.3.7 the expected damage threshold for silica at $1\mu m$ wavelength is $I_d \approx 5kW/\mu m^2$ or in terms of damage fluence $4.1 \cdot 10^{-5} J/\mu m^2$ at 8ns pulse duration. For single mode operation (MFD = $50\mu m$) the damage peak power can be estimated with equation 3.3.

$$P_d = \int I_d e^{-\frac{r^2}{2MFD^2}} dA \approx 4.9MW \quad (3.3)$$

The estimated damage peak power is approximately 5 times higher than the maximum achieved peak power in this work. However, the damage threshold has only been investigated at $1\mu m$ wavelength and is not known at $2\mu m$ wavelength. Considering the result in this work, the fluence F at 1MW peak power (peak intensity $I_0 = 1kW/\mu m^2$) and $\tau = 6ns$ pulse duration is given by equation 3.4. The result is significantly smaller than the measured damage fluence at $1\mu m$ wavelength and 8ns pulse duration.

$$F = \int I_0 e^{-\frac{2t^2}{\tau}} dt = 7.51 \cdot 10^{-6} \frac{J}{\mu m^2} \quad (3.4)$$

In conclusion the record result of MW-level peak power is within a relatively safe operation regime and damage can be avoided when the laboratory is kept clean and if the fiber end facet is well polished. Small dust particles or roughness of the fiber facet can lead to significantly lower damage thresholds and the damage at 200kW peak power is very likely the result of facet contamination.

3.6 Summary of experimental results

The experiments conducted in this work represent a thorough characterization of two novel PCF rod designs with $65\mu m$ (rodA) and $80\mu m$ (rodB) core diameters. An initial measurement was performed with rodB which showed no evidence of strong photodarkening. Subsequently the CW-lasing performance in simple cavities was investigated for both rods and maximum slope efficiencies of $\approx 24\%$ (rodA) and $\approx 28\%$ (rodB) with maximum CW output powers of $> 20W$ at very good beam quality with $M^2 < 1.3$ were achieved. Efficient cross relaxation did not occur in either rod and improvements of the fiber designs are required for further average power scaling. More detailed investigations of the CW-lasing performance of rodB, incorporating a grating as high reflectivity device in the resonator, revealed a large wavelength tuning range of 180nm between 1810nm and 1990nm.

In preparation for the actual goal of peak power scaling in a pulsed thulium based fiber laser system both rods were tested as final amplification stages in a CW -amplification MOPA setup. The master oscillator as well as the first amplification stage were shortly characterized in CW operation. It was found that self pulsation occurs in the MHz range when the oscillator was operated in CW-mode. The CW-amplification results showed slightly lower slope efficiencies for rodA compared to rodB. The slope efficiencies of both rods were lower than for CW-lasing configuration. RodA shows thermal beam degradation at relatively low pump powers. RodB, however, maintained excellent beam quality up to 40W average output power. At highest output power of 52W thermal beam degradation became significant in rodB and limited further amplification.

Thermal mode instabilities have not been observed at these average output powers, although the threshold might be lower than in ytterbium based systems due to the thermal origin of the effect. So far mode instabilities have not been reported in any thulium doped fiber amplifiers, presumably due to the lower average output powers achievable.

RodB was implemented as a final amplification stage in a pulsed MOPA configuration. A maximum average output power of 7.3W at 1kHz repetition rate and 9% slope efficiency were achieved. With at least 90% of the total power in the core and very conservatively estimating the ASE power to be $< 500mW$, the output peak power is $> 890kW$ with 6.4mJ pulse energy. The absence of energy saturation, roll off, or nonlinear temporal/spectral degradation of the pulses indicates this thulium doped PCF rod is capable of greater average power, energy and peak power scaling. Accurate simulation models need to be developed to estimate the extractable energy and to optimize pulse duration, repetition rate and pump power for future peak power scaling beyond 1MW. To prevent damage, the rod end facet needs to be equipped with an end cap.

CHAPTER 4: SIMULATIONS

The promising results in the previous chapter rise the question, if an optimization of the MOPA system could lead to even higher pulse energy and peak power. Better understanding of influential parameters, such as fiber length, doping concentration, core diameter, repetition rate, temperature and ASE generation are of critical importance to exploit the full pulse energy scaling potential of the fiber amplifier.

Multiple investigations need to be done in order to answer important questions about the characteristics of the amplifier. When does energy saturation occur? Is it possible to achieve efficient cross relaxation in thulium doped PCF? How can ASE generation be suppressed while energy extraction is maximized? An accurate model could help to answer these questions. However, high accuracy of the model for large core areas, high peak powers and low repetition rates requires the implementation of thermal effects on the laser performance and is a challenging task.

Steady state CW models have been developed in the past and were useful for investigations and optimization of thulium concentration, fiber length and pump configurations [61, 82]. More advanced models are required to simulate the transient characteristics of a thulium based fiber amplifier. This is particularly challenging because of the relatively complicated energy level structure of thulium and nonlinear processes such as cross relaxation and energy upconversion. Fang et al. presented a transient model including cross relaxation and upconversion effects [14]. However, this model did not include the full spectral information or the generation of ASE. This is of particular importance for the performance optimization (fiber length, core diameter) of an amplifier at low repetition rates ($< 10kHz$).

The modeling approach used here is mainly based on a publication by M. Eichhorn [62]. His work comprises theoretical modeling of W-level average power in thulium doped Fluoride glass

(ZBLAN) fiber amplifiers and a direct comparison between experiment and simulation. The model includes the full spectral information of the laser transition, the generation of ASE, the most important ionic levels and their decay rates, as well as the most influential cross-relaxation and up-conversion rates. The model allows calculations for CW-amplification and pulsed amplification. Moreover it has the potential to be further developed to simulate CW-lasing or Q-switched fiber lasers. In this work Eichhorn's algorithm was implemented in Matlab and used for high power simulations of a silica based, rod type PCF.

An outline of the theory for the model algorithm is presented in subsection 4.1. In subsection 4.2 the CW modeling results are discussed and compared to the experiments. In the experiments strong pump absorption, pump powers of up to 300W and the lack of efficient cross relaxation in the PCF rods lead to very high thermal loads in the fiber core and might significantly influence the amplification performance. A simple analytical model to estimate the radial temperature evolution in the fiber is introduced in subsection 4.3. The simulation model can be expanded by including temperature effects on the emission and absorption cross sections. In this respect subsection 4.4 discusses possible ways and a first attempt to improve the model to achieve more realistic modeling results. Finally the model is used for the simulation of pulsed amplification in subsection 4.5

4.1 Outline of the model

The starting point for the development of the model are the rate equations for the most important energy levels of thulium in silica and $\approx 793nm$ pump wavelength. The rate equations including the most important cross relaxation and energy upconversion processes have been discussed in subsection 2.4.3. From table 2.1 it can be noted that the non-radiative decay rate from level (3) to level (2) is very large for thulium in silica and corresponds to a decay time of approximately 35ns. Thus, in good approximation the population of level (3) is approximately 0 at all times and the en-

ergy level structure simplifies to a 3-level system. This approximation reduces the modeling effort. However, the nonlinear cross relaxation and upconversion rate equation terms are challenging and have to be included in an accurate model. The equations for the pulsed model can be retrieved by the following retardation transformation [62]:

$$\dot{z} = z \quad (4.1)$$

$$\dot{t} = t - \frac{z}{c} \quad (4.2)$$

$$\frac{\partial}{\partial \dot{t}} = \frac{\partial}{\partial t} \quad (4.3)$$

$$\frac{\partial}{\partial \dot{z}} = \frac{1}{c} \frac{\partial}{\partial t} + \frac{\partial}{\partial z} \quad (4.4)$$

The physical translation of this mathematical transformation is a change of the coordinate system to the time frame of the traveling pulse. This transformation in combination with the integration over the transverse plane of the fiber leads to the following basic rate equations of the model ($N_3 \approx 0$):

$$\begin{aligned} \frac{\partial N_4}{\partial t'} &= \frac{N_1}{hc} \sigma_a(\lambda_p) \lambda_p D_p \frac{P_p^+ + P_p^-}{\pi a^2} \\ &\quad - (R_{43} + \Gamma_4 + R_{42} + R_{41}) N_4 - k_{4212} N_4 N_1 + k_{2124} N_2^2 \end{aligned} \quad (4.5)$$

$$\begin{aligned} \frac{\partial N_2}{\partial t'} &= \frac{N_1}{hc} \sum_{j=0}^f \sigma_a(\lambda_j) \lambda_j D_s \frac{P_s^+ + P_s^-}{\pi a^2} - \frac{N_2}{hc} \sum_{j=0}^f \sigma_e(\lambda_j) \lambda_j D_s \frac{P_s^+ + P_s^-}{\pi a^2} \\ &\quad + (R_{43} + R_{42} + \Gamma_4) N_4 - (R_{21} + \Gamma_2) N_2 \\ &\quad + 2k_{4212} N_4 N_1 - (2k_{2124} + k_{2123}) N_2^2 \end{aligned} \quad (4.6)$$

$$\begin{aligned} \frac{\partial N_1}{\partial t'} &= -\frac{N_1}{hc} \sigma_a(\lambda_p) \lambda_p D_p \frac{P_p^+ + P_p^-}{\pi a^2} \\ &\quad - \frac{N_1}{hc} \sum_{j=0}^f \sigma_a(\lambda_j) \lambda_j D_s \frac{P_{s,j}^+ + P_{s,j}^-}{\pi a^2} + \frac{N_2}{hc} \sum_{j=0}^f \sigma_e(\lambda_j) \lambda_j D_s \frac{P_{s,j}^+ + P_{s,j}^-}{\pi a^2} \\ &\quad + (R_{21} + \Gamma_2) N_2 + R_{41} N_4 + k_{2123} N_2^2 - k_{4212} N_4 N_1 + k_{2124} N_2^2 \end{aligned} \quad (4.7)$$

In these equations N_l represents the l's energy level population, h is the Planck constant, c is the speed of light, λ_p is the pump wavelength, λ_j is the j's signal wavelength or ASE wavelength range with wavelength separations $d\lambda = 1nm$ and final wavelength λ_f , a is the doped core radius, $\sigma_{a,e}$ are the absorption and emission cross section, respectively, R_{jk} is the radiative decay rate from the l's to the k's energy level and Γ_l is the non-radiative decay rate for the l's level. In order to account for the double cladding design the pump absorption is determined by the overlap function D_p with the cladding area A_{cl} .

$$D_p = \frac{\pi a^2}{A_{cl}} \quad (4.8)$$

Similarly the overlap D_s of the fundamental mode (assuming Gaussian beam) with the doped core region has been taken into account.

$$D_s = 1 - e^{-\frac{a^2}{2MFD^2}} \quad (4.9)$$

The signal/ASE power $P_{s,j}$ evolution of channel j with wavelength λ_j and pump power P_p evolution for forward (+) and backward (-) propagating light can be described with [62]:

$$\frac{\partial}{\partial z'} P_p^\pm = \mp \alpha_p P_p^\pm \mp \sigma_a(\lambda_p) D_p P_p^\pm N_1 \quad (4.10)$$

$$\begin{aligned} \frac{\partial}{\partial z'} P_{s,j}^\pm &= \mp \alpha_{s,j} P_{s,j}^\pm \mp \sigma_a(\lambda_{s,j}) D_s P_{s,j}^\pm N_1 \mp \sigma_e(\lambda_j) D_s P_{s,j}^\pm N_2 \\ &\pm \sigma_e(\lambda_j) D_s M_j \frac{2hc^2}{\lambda_j^3} d\lambda_s N_2 \end{aligned} \quad (4.11)$$

The last term in equation 4.11 accounts for spontaneous emission that is assumed as stimulated emission into a vacuum noise intensity, where the factor M_j represents the number of guided modes at wavelength λ_j . For simplicity reasons the signal wavelength was assumed to be only 1nm broad and was represented by one wavelength channel. The ASE spectrum was represented by a total of 460 channels with 1nm width, ranging from 1605nm to 2165nm.

The set of rate equations needs to be solved in conjunction with the power evolution in the fiber not only in steady state, but for transient behavior. The route to success is the separation of calculations for population density evolution with time and beam power evolution in the fiber with propagation distance. The fiber is divided into a number of segments Δz (e.g. $L = 100$) and each segment is treated as a separate medium with a specific population density as a function of time. A schematic drawing of the fiber segmentation is shown in figure 4.1.

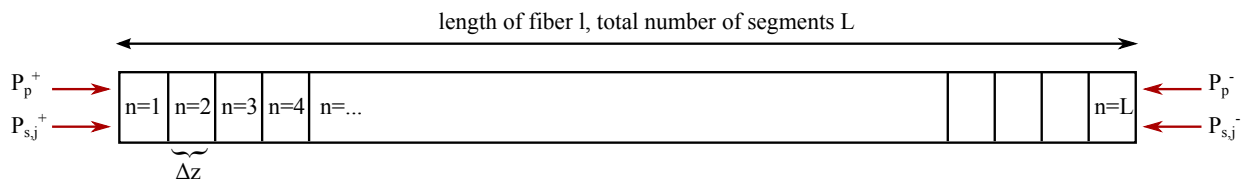


Figure 4.1: The fiber is divided into segments with width Δz and the input pump and signal powers in forward and backward direction are propagated to the left and right, respectively, through all L segments at each time step Δt .

A summary of the modeling algorithm for transient characteristics of a thulium based fiber amplifier is given in figure 4.2. The initial signal and pump powers in backward and forward direction are predefined as time dependent functions. In the following the ASE seed at the j 's wavelength in each segment is included in the term signal power or signal field. Initially ($t=0$) the total population N_{tot} is assumed to be in the ground state $N_1 = N_{tot}$. For the first time step the initial input pump and signal powers in forward direction are propagated through each segment to the opposite end of the fiber by evaluating equations 4.11 and 4.10. For a single pass amplifier with forward (rightward) seed input the signal power at the end of the fiber already yields the output power of the first time step. The backward pump and signal fields are also propagated for the first time step from the right to the left end of the fiber. It is important to note, that at this point of the calculation, the population is still completely in the ground state. As a second step the pump and signal powers in forward and backward direction, that are known for each segment and for the first time step, are used for the evaluation of the rate equations 4.7, 4.6, 4.5 to retrieve the change of the population

densities in each fiber segment. For this purpose the well known fourth order Runge Kutta method was used [83]. Now that the population densities are known after the first time step, the input signal and pump powers of the next time step can be propagated through the fiber and the procedure starts again from the beginning, where the time dependent input signal and pump powers need to be changed accordingly. The calculation is continued until a certain simulation time t_{end} is exceeded. The total simulation time is mainly determined by the input characteristics (repetition rate, peak power and pump power) and cannot be predetermined. Clearly reliable simulation results can only be achieved when the quasi-CW regime of a repetitively pulsed amplifier is reached.

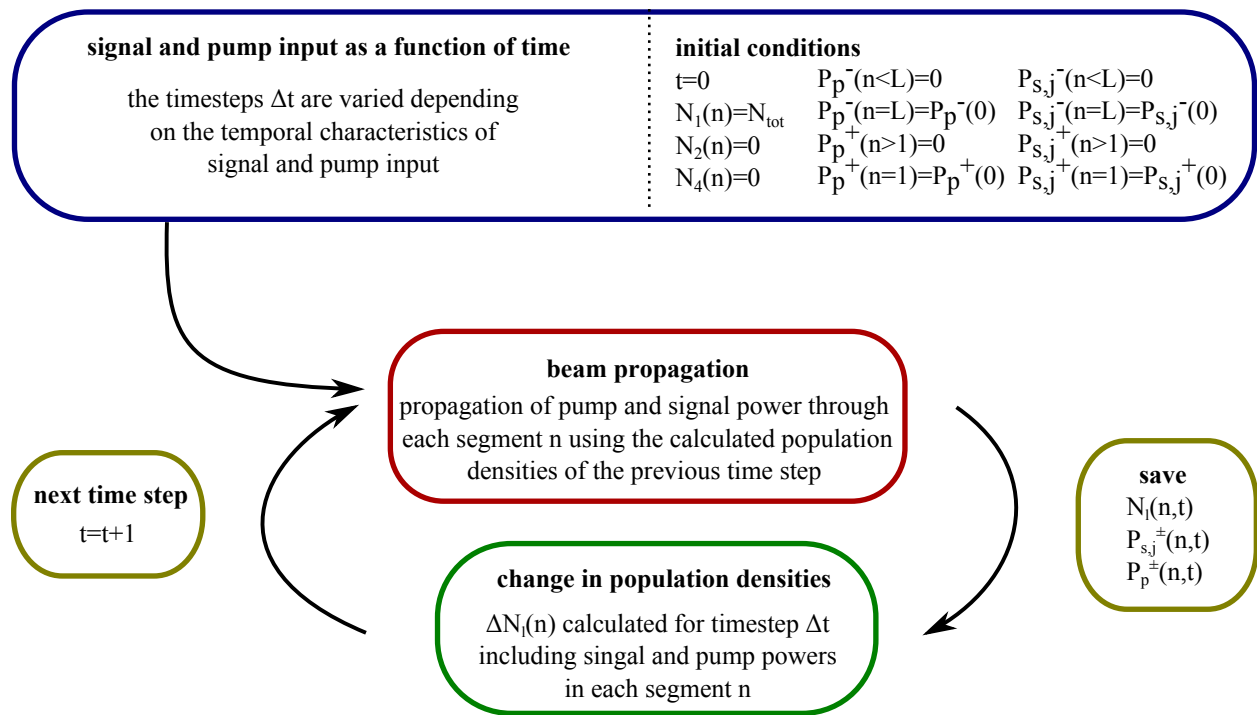


Figure 4.2: Schematic summary of the simulation algorithm allowing for transient modeling of pulsed signal and pump input including ASE generation. First the equations for forward and backward propagating pump and signal power are evaluated for each fiber segment of length Δz using equations 4.11 and 4.10. Subsequently the change of population densities is evaluated for a small time step Δt using the rate equations 4.7, 4.6, 4.5.

In order to reach the quasi-CW regime the time steps Δt need to be in the order of 0.01ns when modeling pulsed amplification with pulse durations of $\approx 6ns$. For low repetition rates in the order of 1kHz multiple ms need to be simulated before the calculation converges and millions of calculation steps were required. A simple way to reduce computational effort is to vary the time steps with respect to the input signal. Time steps in the order of the pulse duration divided by a factor 400 are sufficient at times when a pulse is actually propagating through the fiber. The time step can be chosen much larger between the pulses, roughly $0.001/\nu_{rep}$, when the pump signal is continuous and the ASE signal is relatively weak, leading to computation times of ≈ 1 hour.

4.2 Modeling CW-amplification

The simulations for CW-amplification were carried out with the specifications for rodB only. The thulium ion concentration was provided by NKT Photonics and is $2.5wt.\%$. This corresponds to an ion density of approximately $8.7 \cdot 10^{25}m^{-3}$. All important parameters for the simulations have been taken from tables 3.1 and 2.1.

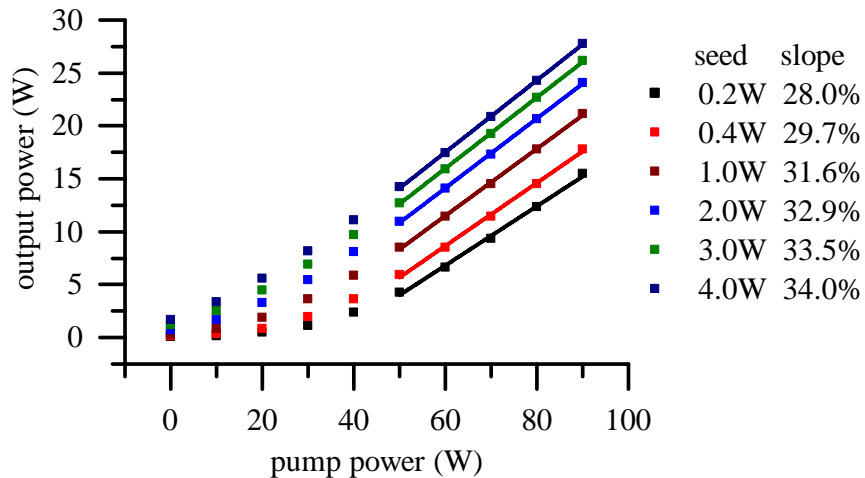
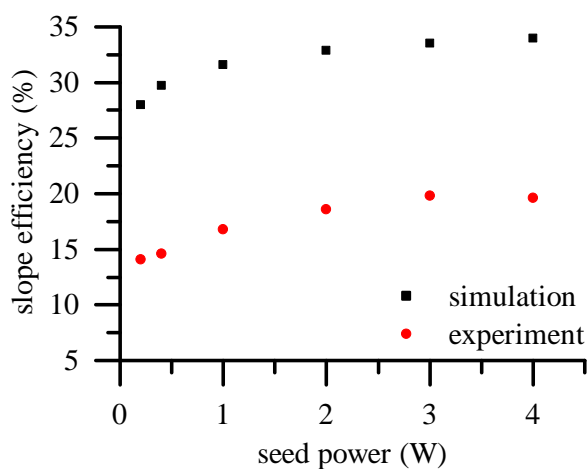
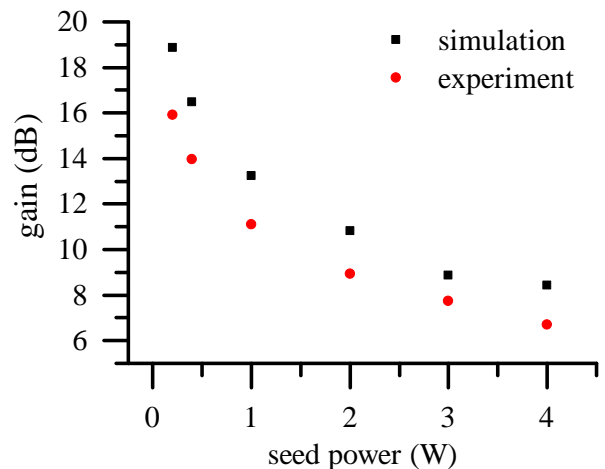


Figure 4.3: Simulated signal power evolution with pump power for various seed powers

The simulated signal power evolution with pump power for various seed powers is depicted in figure 4.3. The seed powers were chosen to match the CW-amplification experiments with rodB and a maximum of 100W pump power (compare with subsection 3.4.4). The calculated slope efficiencies are much higher than the experimental findings. A comparison between simulation and experiment is given in figure 4.4. Figure 4.4a compares the slope efficiencies for different seed powers. Qualitatively the simulation and experiment show the same behavior. Quantitatively the slope efficiencies of the simulation are roughly a factor 2 larger than in the experiments. This is also reflected in the achievable gain for various seed powers, as shown in figure 4.4b. It is worth noting that cross relaxation did not lead to efficiencies above 40% in the experiments or the simulations. Interestingly the found slope efficiencies in the order of 30% were experimentally confirmed with a flexible PCF [5] with similar glass composition. Moreover Jansen et al. published slope efficiencies above 30% in a LPF rod also with similar glass composition [75]. At this point it is unclear why rodA and rodB have lower efficiency. Clearly there must be physical mechanisms that significantly reduce efficiency and are currently not included in the model.



(a) Experimental and simulated slope efficiencies for different seed powers.



(b) Simulated and experimentally determined gain coefficients for various seed powers.

Figure 4.4: Comparison of simulated slope efficiency and gain with experimental results.

The model includes the generation of ASE in forward (co-propagating) and backward (counter-propagating) direction. Figure 4.5a shows output spectra at 90W pump power for 0.2W and 4W seed power, respectively. The spectra show that only very weak ASE is present at both seed powers. This is in good agreement with the experiments. The ASE content is increased for lower seed powers, which is related to the lower energy extraction at lower signal powers in the fiber. The signal power evolution in the fiber for both cases is depicted in figure 4.5b.

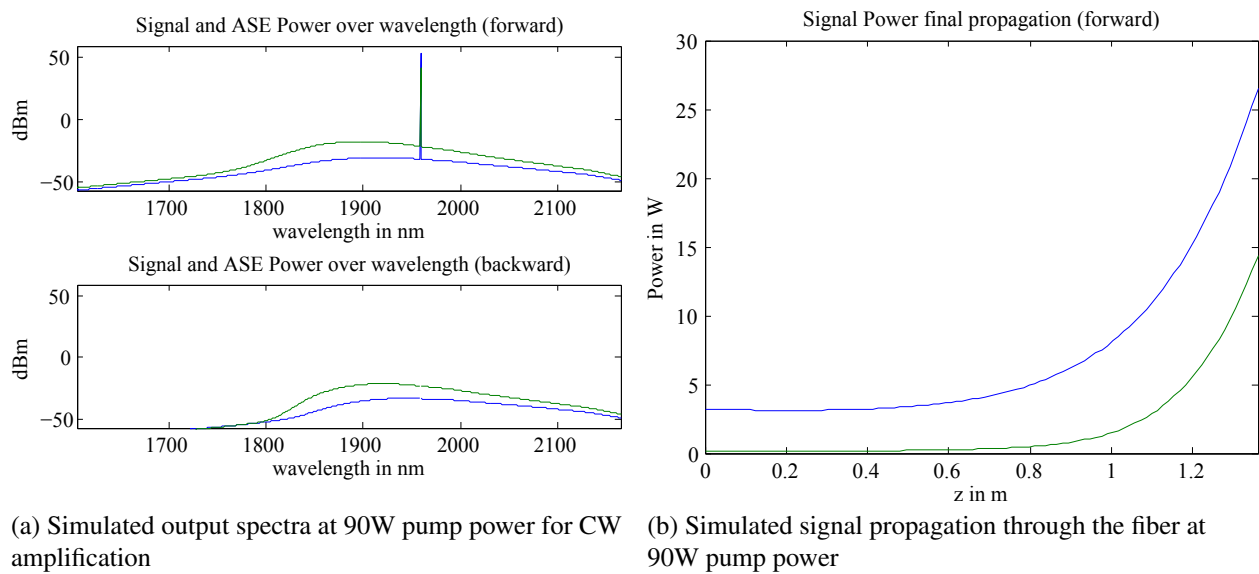


Figure 4.5: Simulated output spectra and signal propagation for 0.2W (blue) and 4W (green) seed signal at 90W pump power

Similarly the time evolution of the output signal can be viewed. This was done in figure 4.6a at 90W pump power for 0.2W and 4W seed power, respectively. The total simulation time was set to 1ms in order to safely reach the CW-regime even for relatively small seed powers. The different energy extraction of the two different seed powers manifests itself in the pump absorption along the fiber. This can be seen in figure 4.6b. The 4W seed power is depleting the excited state inversion faster than the 0.2W seed power. Consequently the ground state becomes more populated and the pump absorption is enhanced.

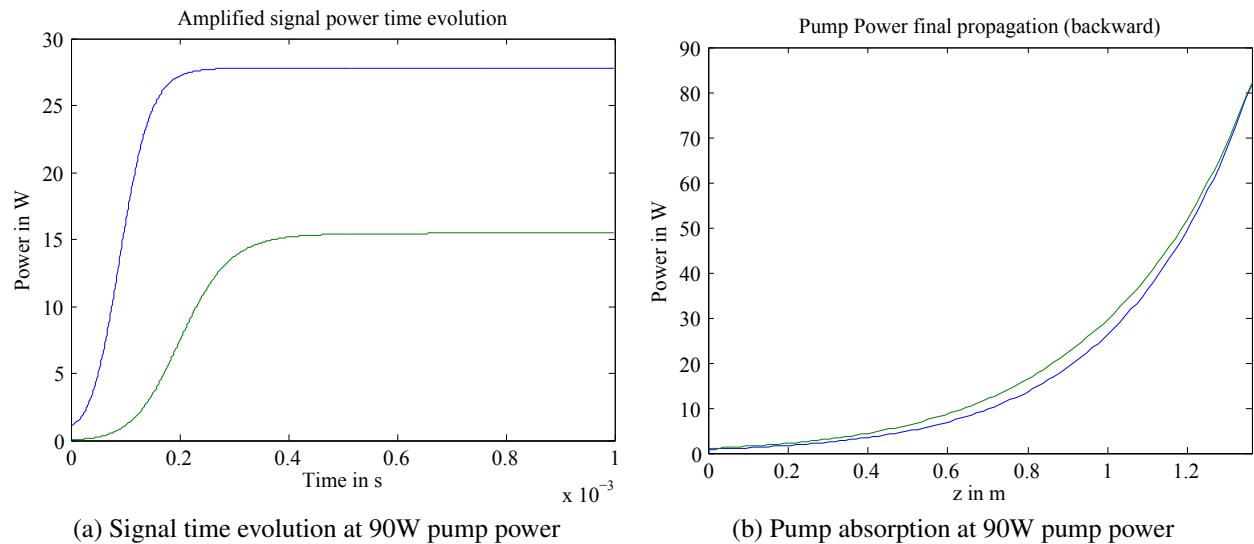


Figure 4.6: Simulated time evolution of the output signal and pump absorption along the fiber for 0.2W (blue) and 4W (green) seed signal at 90W pump power

In addition to the CW-amplification investigation the ASE generation was simulated without input signal. A total of 6 guided modes were assumed for rodB (compare with equation 4.11). The ASE powers of experiment and simulation for various pump powers are compared in figure 4.7a. Two things can be noticed from this graph. First the measured ASE content at pump powers below 70W is always larger than the simulated ASE power. Second the threshold of the simulated ASE slope occurs at higher pump power than in the experiment. However, for sufficiently large pump powers the simulated ASE slope seems larger than in the experiments and it can be expected, that the total simulated ASE power at higher pump powers ($> 80W$) is overestimated by the model. For qualitative comparison the measured ASE spectrum at 17W pump power is plotted in figure 4.7 with the simulated ASE spectrum at similar pump power. To qualitatively compare the shapes of the spectra, the simulated ASE spectrum was subtracted by 18dBm in order to match the maximum of the measured spectrum. The measured spectrum does not include the full power content of the real ASE output. The spectral peaks are in the same range. The wings of the spectrum, however,

differ. At short wavelength the measured spectrum is stronger and at long wavelength weaker than the simulated one.

In summary the CW simulation results for rodB deviate from the experimental findings. The simulated slope efficiencies exceed the measured slope efficiencies by about 40%. The calculated maximum output powers are similarly about 40% larger than in the experiments. What causes these deviations? There are multiple possible reasons. First the model does not account for temperature effects on the wave guiding properties, the emission and absorption cross section and the non radiative decay rates. Second the cross relaxation and energy upconversion rates are not known for the fiber under test. If clustering of thulium ions is present in the rod, energy upconversion might be the dominant process and could significantly reduce the slope efficiency (compare with subsection 2.4.2). Moreover the emission and absorption cross sections used in this model have not been measured for this specific rod or the glass preform. The absorption and emission cross section have been taken from the PhD thesis of T. McComb [64].

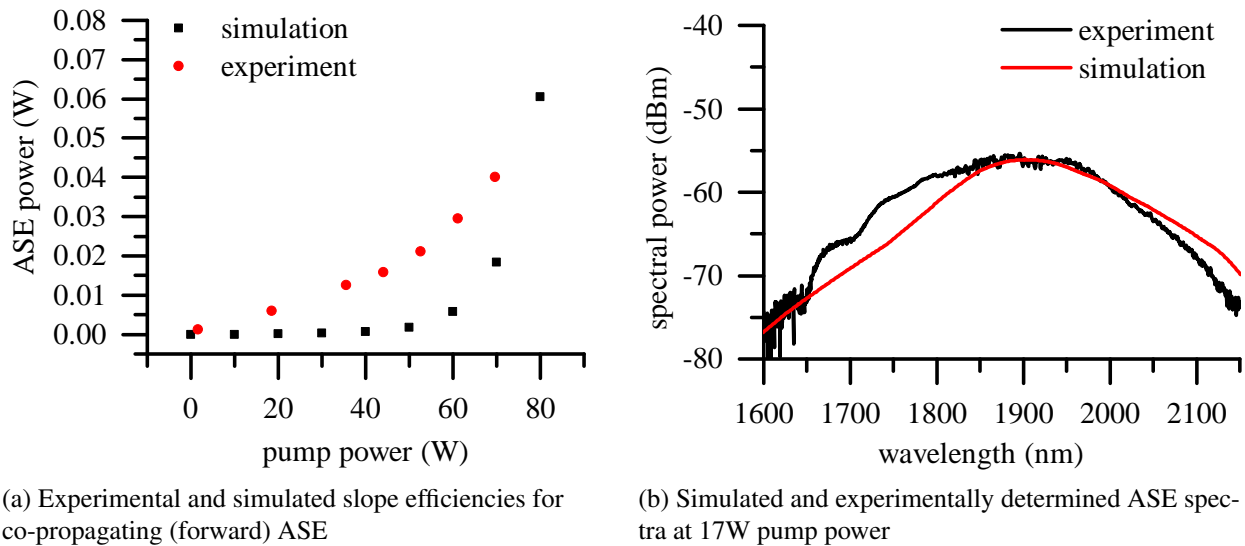


Figure 4.7: Comparison of simulated ASE slope efficiency and spectrum with experimental results

4.3 Temperature in the fiber core

As discussed in the previous subsection the simulation does not deliver satisfying results and significant deviations from the experimental findings can be observed. Consequently the model needs improvement in order to be used for optimization of the MOPA design. The absence of efficient cross relaxation in the experiments leads to a considerable heat load in the pumped fiber due to the large quantum defect. High temperatures in the core region are likely to have a detrimental effect on slope efficiency and maximum output power.

The thermal population of the excited energy manifold (level (2)) influences the effective number of available inverted ions for the stimulated emission process. Similarly the absorption is increased for high temperature, because the high phonon energy levels of the ground state (level(1)) become more populated. These processes lead to temperature dependent effective absorption and emission cross sections, that were assumed to be constant throughout the fiber. The temperature dependence of the effective emission cross section has been experimentally verified in [63] (compare subsection 2.4.4). Unfortunately the dependence has only been measured for temperatures below 300K and is currently unknown for temperatures well above 300K. Likewise the temperature dependence of the effective absorption cross section is unknown. Other influential parameters on laser and amplifier performance, like non radiative decay rates, upconversion and cross relaxation rates, might be temperature dependent as well. The temperature dependence of the above mentioned parameters needs to be experimentally investigated in order to achieve more realistic modeling results.

Thus, the fiber core temperature under pumping conditions needs to be known at each segment Δz along the fiber. In the following a simple analytic temperature model is introduced. The modeling idea is based on a publication by Limpert et al. [84]. In their work this modeling technique was applied to microstructured fibers with an air-cladding structure similar to the PCF rod design in this work.

Heat can be transported by three different mechanisms, namely conductive, radiative and convective heat flow. These three mechanisms together are used in this model to estimate radial thermal distribution of a fiber segment Δz . Although the longitudinal heat flow has been neglected for simplicity, the model is still quite accurate for core temperature calculation, because the thermal gradients in fibers are in general significantly larger in radial than in longitudinal direction. Limpert et al. have compared the results of this analytic model with more sophisticated models utilizing the finite element method and found good agreement between them.

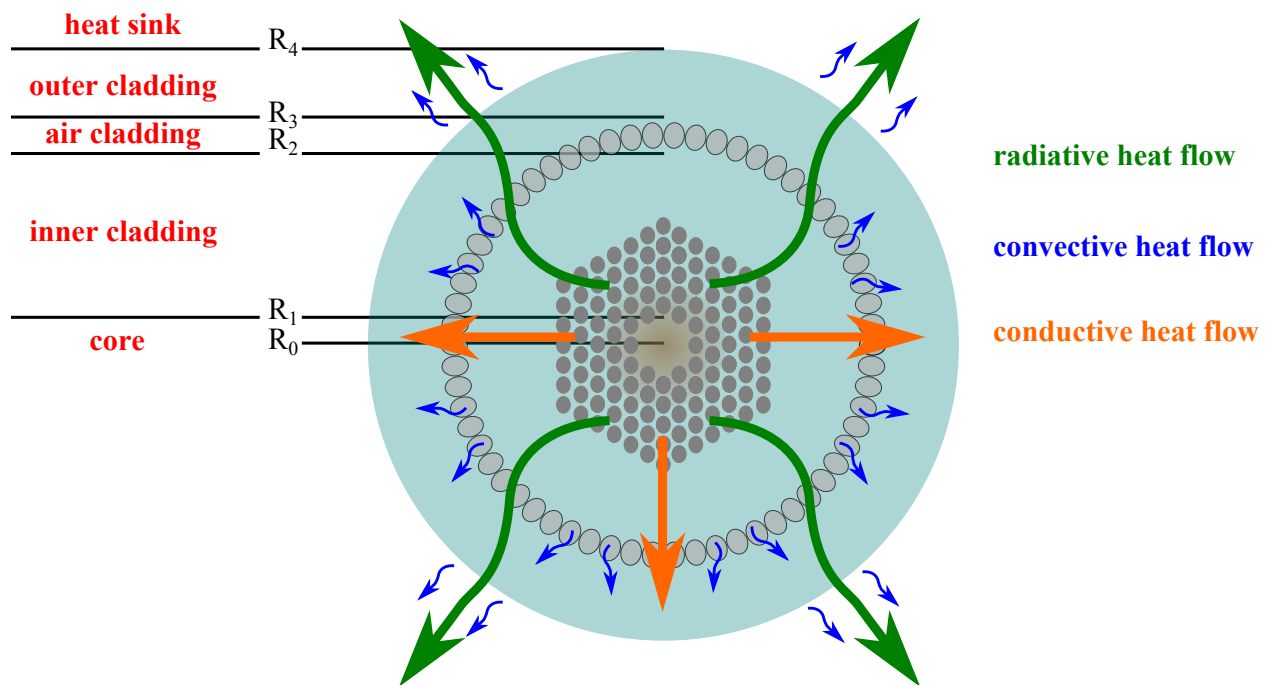


Figure 4.8: Heat flow mechanisms in an air-clad microstructured active fiber [84]

Figure 4.8 shows a microstructured fiber and the dominant heat transport mechanisms in different regions of the fiber design. Radiative heat flow is present in all regions of the fiber and the ambient. Conductive heat flow is dominant in the pure silica regions of the fiber, namely the core, the inner cladding and outer cladding. The heat transport at the air-cladding is determined by the number and size of the air holes, where heat flow is prevailed by convection, and the number

and size of the glass bridges, where heat flow is dominated by conduction. The ambience can e.g. be air, moving air or a water cooled heat sink. The convective heat flow needs to be adjusted accordingly in this region [84].

The temperature of the fiber surface T_4 , R_4 is first calculated by balancing the convective and radiative heat flow Φ_{conv} and Φ_{rad} into the ambient air at temperature T_A with the generated heat H per unit fiber length Δz . The radiative heat flow is given by the Stefan-Boltzmann law with the Stefan-Boltzmann constant $\sigma = 5.6705 \cdot 10^{-8} W/K^2 m^2$ and the emission factor $\epsilon = 0.95$ for fused silica. The convective term includes a temperature dependent parameter C_1 , that is determined by the ambient cooling conditions (e.g. air movement or water cooling) [84]. The temperature T_4 cannot be explicitly calculated. To retrieve T_4 the root of the function needs to be found numerically.

$$\begin{aligned} 0 &= \Phi_{conv} + \Phi_{rad} - \frac{H}{\Delta z} \\ &= 2\pi R_4 C_1 \left(\frac{T_4 - T_A}{2R_4} \right)^{0.25} \cdot (T_4 - T_A) + 2\pi R_4 \sigma \epsilon (T_4^4 - T_A^4) - \frac{H}{\Delta z} \end{aligned} \quad (4.12)$$

The determined temperature T_4 can then be used to calculate the temperature T_3 at the transition air-cladding to outer cladding (R_4). The dominant heat transfer process in the fiber is heat conduction. The temperature T_3 can be calculated with equation 4.13 including the heat conductivity $k = 1.37 \frac{W}{Km}$ in fused silica [84].

$$T_3 = \frac{H(R_4 - R_3)}{k\pi(R_4 + R_3)} + T_4 \quad (4.13)$$

The heat flow through the air-cladding is more difficult to describe. All three heat transfer processes need to be included, since heat convection occurs through the air in the holes and heat conduction is involved through the glass bridges connecting the inner and outer cladding. The heat conduction can be estimated by accounting for the total number of silica glass bridges $\#_{bridges} \approx 100$,

the bridge width $W_{bridge} \approx 0.1\mu m$ and the bridge length $L_{bridge} \approx 10\mu m$ (all values given for rodB). The temperature at the rim of the inner cladding can be approximated by finding the root of equation 4.14 [84].

$$\begin{aligned}
0 &= \Phi_{conv} + \Phi_{rad} + \Phi_{cond}^{airclad} - \frac{H}{\Delta z} \\
&= 2\pi R_2 C_2 \left(\frac{T_2 - T_3}{2R_2} \right)^{0.25} \cdot (T_2 - T_3) + 2\pi R_2 \sigma \epsilon (T_2^4 - T_3^4) \\
&\quad + k \cdot \frac{\#bridges \cdot W_{bridge}}{L_{bridge}} (T_2 - T_3) - \frac{H}{\Delta z}
\end{aligned} \tag{4.14}$$

Knowing the temperature T_2 at the outer rim of the inner cladding allows for the calculation of the temperature T_1 at the core to inner cladding transition R_1 by accordingly evaluating the heat conduction with equation 4.13. Similarly the temperature T_0 at the core center can be calculated. The air holes in the inner cladding have very large bridge widths and the heat flow process can be estimated with heat conduction through solid silica glass. Of course the heat load is distributed throughout the core area and the calculated peak temperature T_0 at the fiber center is not realistic. For the implementation in the simulation model of a fiber amplifier the temperature in the core can be approximated by averaging the temperature at the core center with the temperature at the core to inner cladding transition.

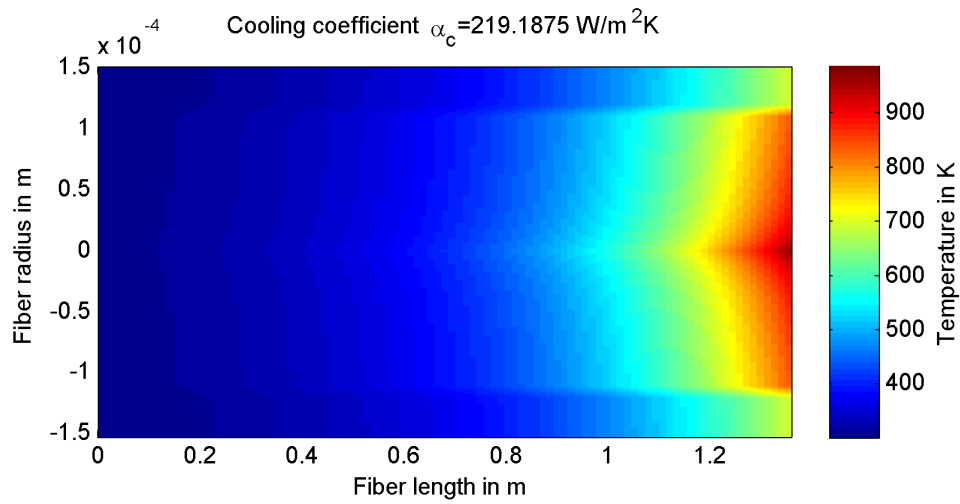
In the following the modeling results for the radial temperature distribution of rodB in CW-operation are presented. The used fiber design specifications were previously given in table 3.1. The heat load per unit length was calculated from the modeled pump absorption at 6W CW-seed power and 250W pump power. This corresponds to the experiment presented in subsection 3.4.4. In this experiment strong thermal lensing and a sudden drop of efficiency were observed for output powers $> 40W$.

Figure 4.9 shows the calculated radial temperature distribution for all segments along the fiber. The ambient cooling coefficient α_c was calculated with equation 4.15 and $C_1 = 10W^{1.75}/m^{1.75}K^{1.75}$ that is 10 times lower than $C_1 = 100/m^{1.75}K^{1.75}$ for efficient ambient water cooling [84].

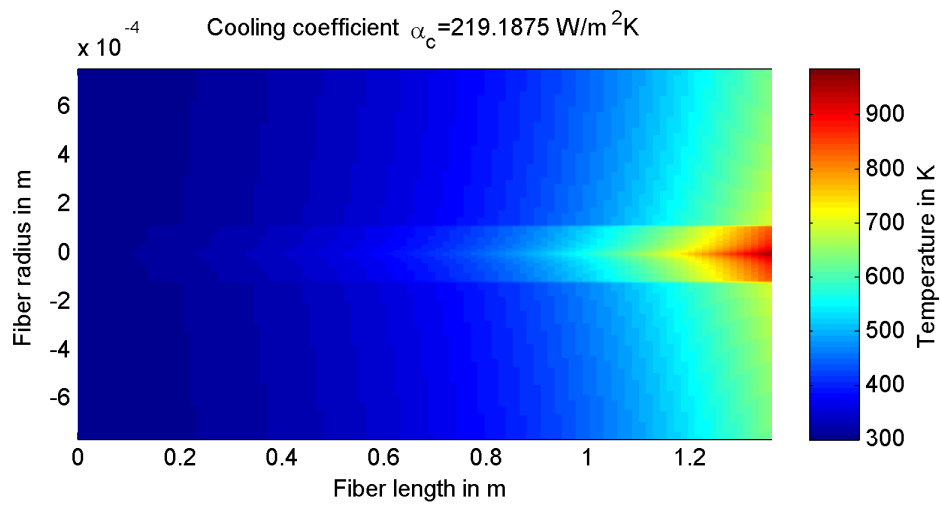
$$\alpha_c = C_1 \cdot \left(\frac{T_4 - T_A}{2R_4} \right)^{0.25} \quad (4.15)$$

For the chosen cooling coefficient of $\approx 220W/Km^2$ (e.g. forced air cooling) the average temperature in the core at the tip of the fiber approaches 950K and more than 600K fiber surface temperature. For comparison the melting point of silica glass is $\approx 2100K$. The temperature profile at the fiber tip cross section is separately depicted in figure 4.11a. Figure 4.10 shows the temperature modeling results for $C_1 = 100/m^{1.75}K^{1.75}$, a reasonable value for a water cooled ambience [84], corresponding to a cooling coefficient of $\approx 1410W/Km^2$.

It can be observed for both cooling conditions that the air cladding acts as a thermal insulation layer and prevents heat flow from the inner cladding to the outer cladding and eventually to the fiber surface. The temperature in the core is significantly reduced by $\approx 300K$ for the improved cooling conditions. In contrast the thermal gradient is not influenced by the cooling. The temperature step between core and outer cladding is approximately 250K for both cooling coefficients. Consequently the average temperature in the core will always be at least 250K higher than the ambience at this heat load at the fiber tip.

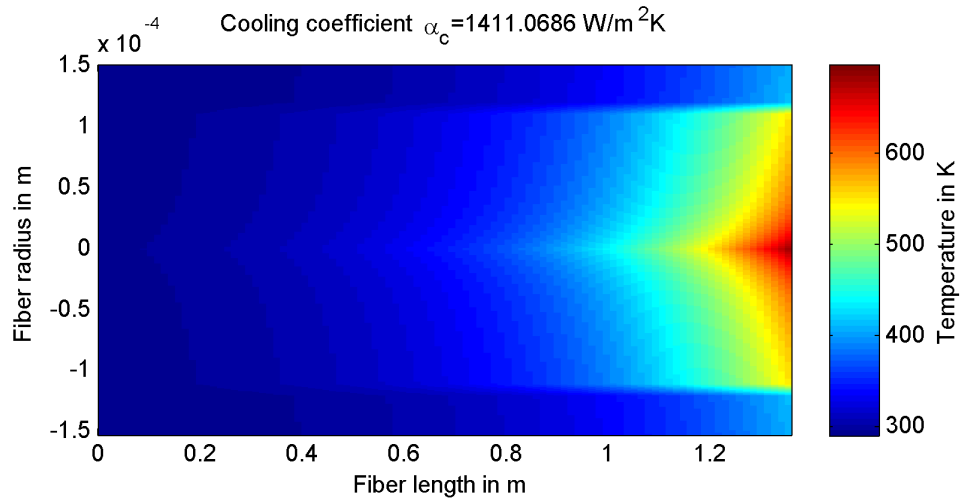


(a) Temperature at the inner cladding and core area of the fiber

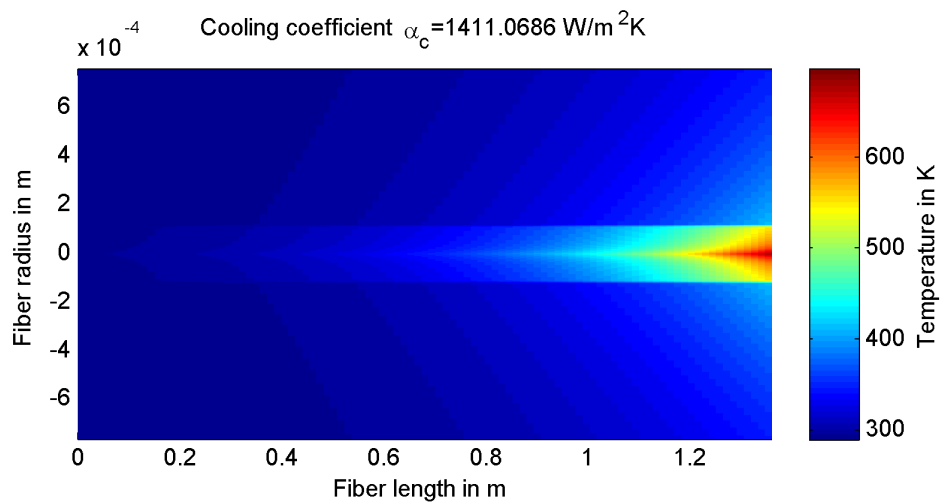


(b) Full radial temperature profile of the fiber

Figure 4.9: Radial temperature profile of rodB at 6W seed and 250W pump power. The temperature in the core reaches $\approx 1000\text{K}$ when not sufficiently cooled.

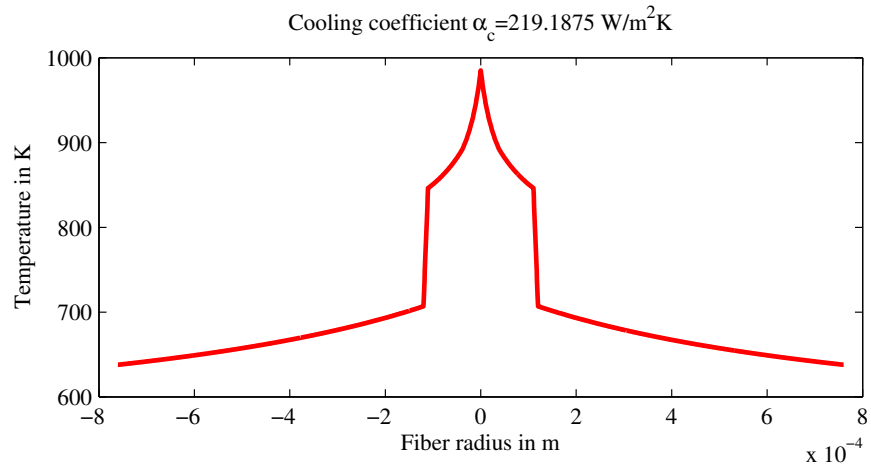


(a) Temperature at the inner cladding and core area of the fiber

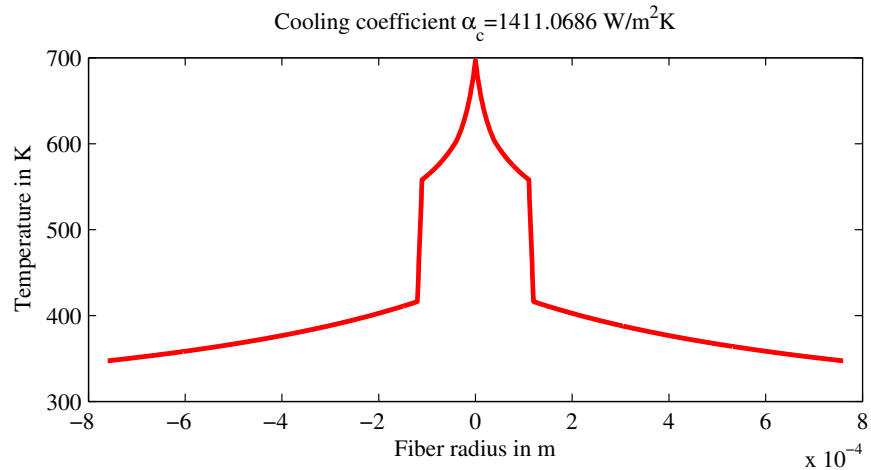


(b) Full radial temperature profile of the fiber

Figure 4.10: Radial temperature profile of rodB at 6W seed and 250W pump power. The temperature in the core is significantly decreased when the cooling conditions are improved.



(a) Radial temperature profile of the fiber tip for insufficient cooling



(b) Radial temperature profile of the fiber tip when water cooled

Figure 4.11: Radial temperature profile of the fiber tip at 6W seed and 250W pump power for two different cooling conditions.

4.4 Improved model

As discussed in the previous section the emission and absorption cross sections are temperature dependent and temperatures vary significantly for different segments in the fiber. In the following subsection a methodology is introduced, to my knowledge for the first time, that includes the

temperature dependence of the emission cross section in the previously introduced transient model for thulium based amplifiers. A common method to calculate the emission cross section from an experimentally determined absorption cross section is the so called reciprocity method [63]. The reciprocity formula (equation 4.16) allows for the calculation of the emission cross section at a given temperature if the absorption cross section is known. Unfortunately the temperature dependence of the absorption cross section in thulium doped silica has so far, to the best of my knowledge, not been investigated. Nevertheless, as a proof of principle the absorption cross section is in this work assumed to be constant for all temperatures. The reciprocity formula is [63]:

$$\sigma_e(T, \lambda) = \sigma_a(T, \lambda) \frac{Z_l}{Z_u} \exp \left[\frac{E_g - hc/\lambda}{k_B T} \right] \quad (4.16)$$

Therein, $\sigma_{a,e}$ the emission and absorption cross sections, Z_l and Z_u are host dependent partition functions, E_g is the energy difference between the lowest Stark level energy of the upper and lower manifold. The energy difference E_g for thulium doped silica is 0.69eV. The ratio of the partition functions is not known and is strongly dependent on the host material [63]. Here the ratio was determined to be $Z_l/Z_u = 4.2$ by matching the calculated emission cross section at room temperature with the emission cross section from McComb et al. that was determined by fluorescence measurement [64]. The absorption cross section used for the temperature dependent calculation of the emission cross section is similar to the one used in the unimproved model in subsection 4.2 and was taken from [64]. The calculated emission cross sections for different temperatures are depicted in figure 4.12.

The emission peak is shifted to smaller wavelength and is increased. The left wing of the emission cross section is generally increased with temperature, while the right wing is decreased with temperature. This is already an indication, that the amplification slope efficiency suffers with increasing temperature and signal wavelength $> 1800nm$. The calculated characteristics qualita-

tively match with the observations in the work of Turri et al., who investigated the temperature of the emission cross section in thulium doped silica glass below 300K [63]. This work was discussed in more detail in subsection 2.4.4. The effective emission fluorescence is not increased, because the overlap with the absorption cross section increases with shorter peak emission wavelength.

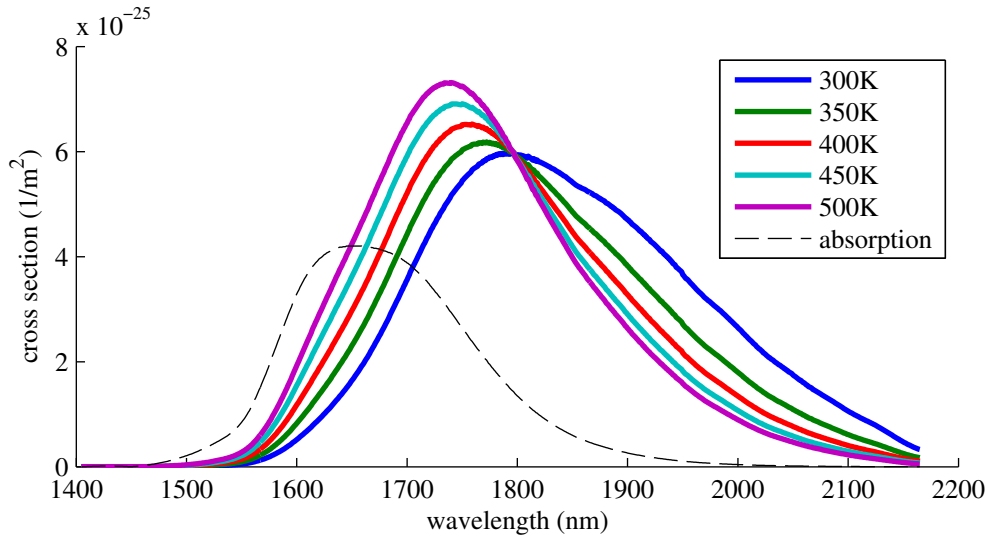


Figure 4.12: Emission cross sections at different temperatures calculated with the reciprocity method assuming a temperature independent absorption cross section.

The calculation procedure for temperature dependent emission cross sections in conjunction with the analytical temperature model can now be implemented in the amplification model. Since the pump power absorption is known throughout the fiber, the heat load per unit length can be calculated in each fiber segment with the quantum defect η .

$$H = P_{pump}^{abs} \cdot \eta \quad (4.17)$$

Subsequently the core average temperature can be simulated for each fiber segment with the model presented in subsection 4.3. The reciprocity formula is then used to calculate the emission cross

section for each fiber segment independently. In order to save simulation time, the emission cross section was only calculated every 25 time steps.

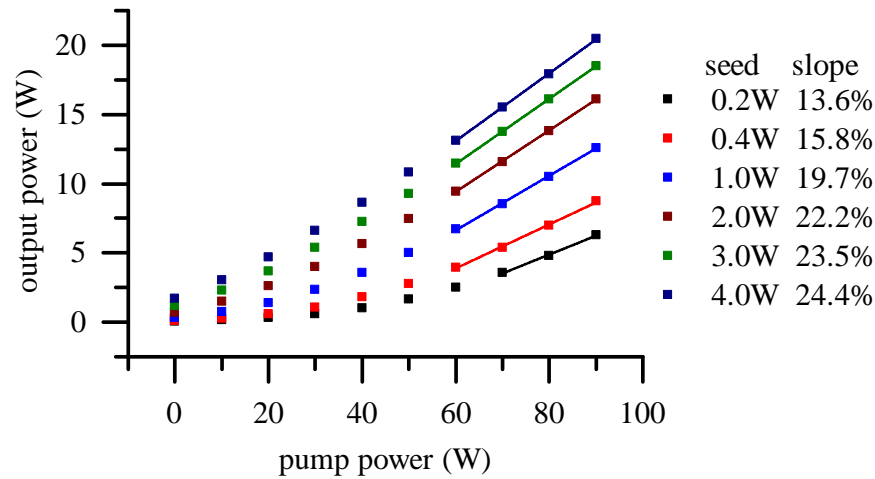
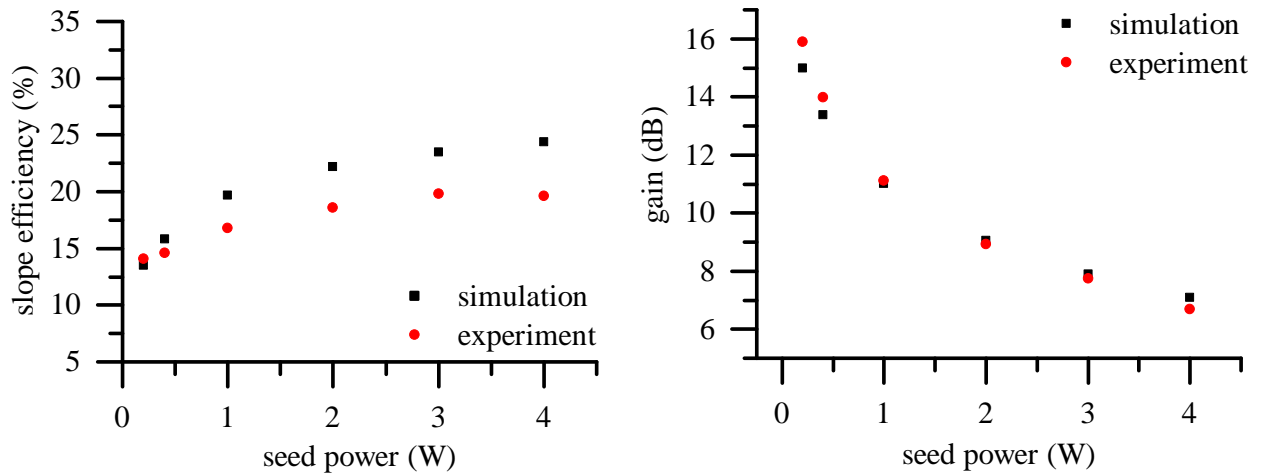


Figure 4.13: Simulated signal power evolution with pump power for various seed powers including temperature effects in the model.

The CW-amplification simulations were carried out in a similar manner to subsection 4.2 and the results are shown in figure 4.13. The simulated slope efficiencies are significantly reduced compared to the modeling results in subsection 4.2. This is due to the afore mentioned reduction of the emission cross section with temperature at wavelengths $> 1800nm$. The slope efficiencies compare better with the experimental findings, as shown in figure 4.14a, and are generally slightly too large for high seed powers. The deviation from the experiment is likely the result of the approximation, that the absorption cross section is constant with changing temperature. Moreover the possible temperature dependencies of cross relaxation and energy upconversion, as well as the non radiative decay rates have not been accounted for in this improved version of the model. Nevertheless, the calculated gain of simulation and experiment at $\approx 90W$ pump power match very well (figure 4.14b).



(a) Experimental and simulated slope efficiencies including temperature effects.

(b) Simulated and experimental gain at 90W pump power including temperature effects.

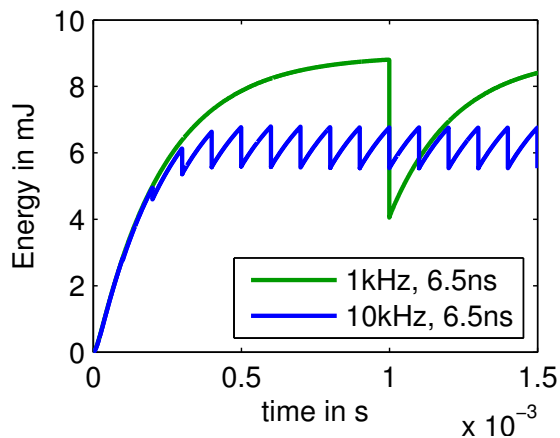
Figure 4.14: Comparison of simulated slope efficiency and gain with experimental results including temperature effects in the model.

4.5 Modeling pulsed amplification

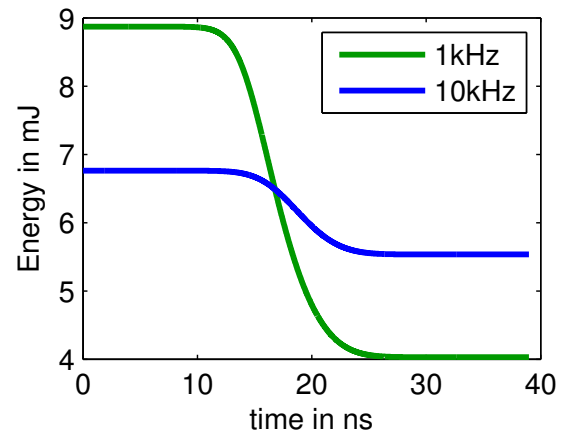
The improved model can now be used for the simulation of pulsed amplification in rodB. The simulations were carried out for the experimentally used repetition rates, pulse durations, seed powers and pump powers. These parameters and the experimental results for comparison can be found in section 3.5.

The simulation time for the pulsed amplification modeling is determined by the time required to reach the quasi-CW regime. The best indication, if the quasi CW-regime is reached or not, is the investigation of the stored energy time evolution. The stored energy in the fiber can be calculated with the known inversion in each segment of the fiber at each time step. Figures 4.15 and 4.16 show the time evolution for 1kHz/10kHz and 10kHz/20kHz at 6.5ns and 100ns respectively. The quasi-CW regime is reached, when the energy extraction with time is similarly repeated for each cycle. The energy extraction per pulse is strongly dependent on repetition rate and pulse duration.

The largest energy extraction per pulse is achieved at 1kHz repetition rate, as shown in figure 4.15b. Longer pulse durations can increase the extractable energy at a given repetition rate. This can be seen by comparing the 10kHz graphs of figures 4.15b and 4.16b at 6.5ns and 100ns, respectively. The extracted energy is increased from $\approx 1.1mJ$ at 6.5ns to $\approx 1.6mJ$ at 100ns pulse duration.

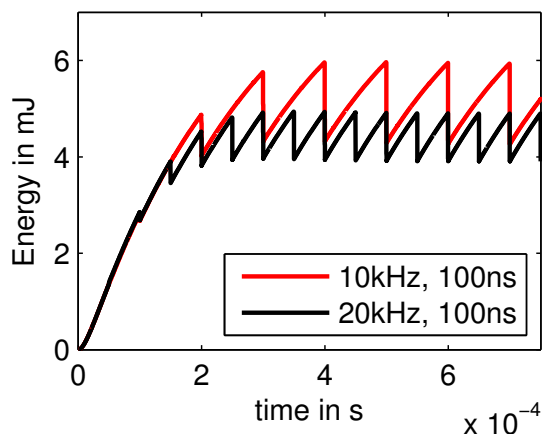


(a) Stored energy evolution with time for 1kHz and 10kHz repetition rate.

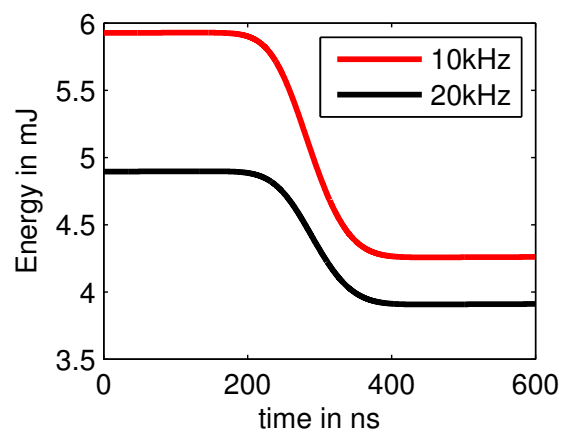


(b) Energy extraction for 6.5ns pulses

Figure 4.15: Simulated stored energy for 10kHz and 1kHz repetition rate at 100W pump power.



(a) Stored energy evolution with time for 10kHz and 20kHz repetition rate.



(b) Energy extraction for 100ns pulses

Figure 4.16: Simulated stored energy for 10kHz and 20kHz repetition rate at 100W pump power.

The simulated pulsed slope efficiencies are depicted in figure 4.17 and are too large for 10kHz and 20kHz and slightly too small for 1kHz repetition rate. Part of the differences can be explained with observed deviation from the experimental results found for the CW-simulation in figure 4.14a. The model tends to simulate relatively large efficiencies for high seed powers. Similarly in the case of pulsed simulation, the low seed power at 1kHz repetition rate leads to an underestimation of the slope efficiency and at high seed power to an overestimation of slope efficiency. The pulsed operation has only minor effects on the simulated efficiencies for high repetition rates that are reduced by an absolute of only $\approx 1\%$ compared to the CW -results. The experiments showed a more significant reduction of $\approx 2\%$. At 1kHz repetition rate the simulation reveals a more significant drop in efficiency to 7.2% from 14% in CW at similar seed average power. In comparison the experimentally determined efficiency was 9.2%.

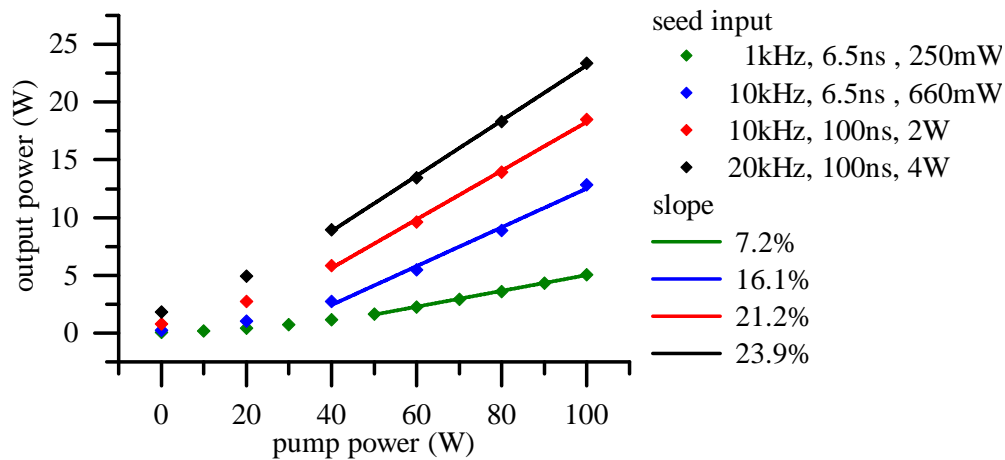
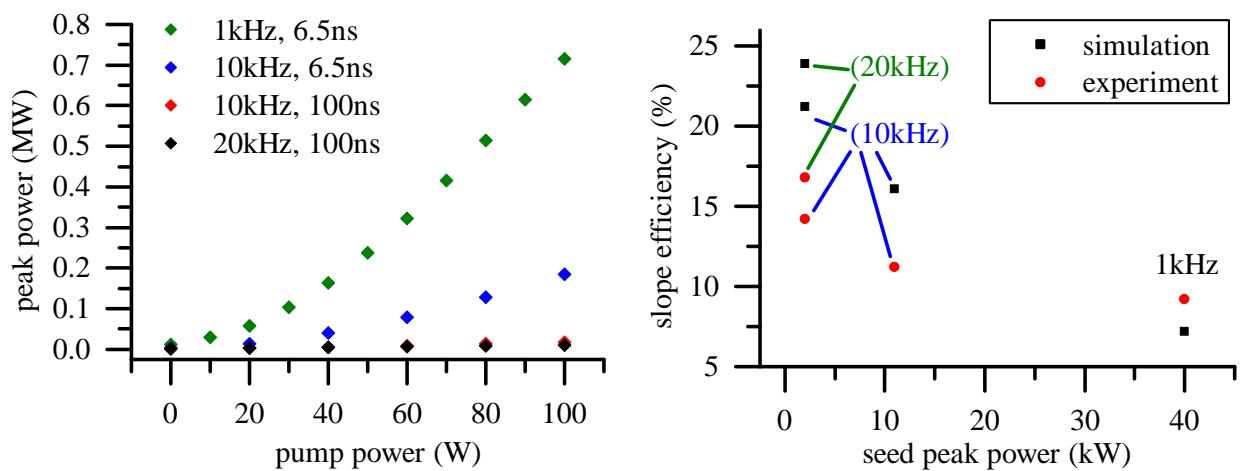


Figure 4.17: Simulated pulsed average power evolution with pump power for various seed powers, pulse repetition rates and pulse durations.

The peak power evolution with pump power for all seed inputs is depicted in figure 4.18a. The maximum peak powers simulated were $\approx 700kW$ at 1kHz and $180kW$ at 10kHz repetition rate. In comparison, the experimental results were $\approx 900kW$ at 1kHz and $\approx 150kW$ at 10kHz repetition rate and 6.5ns pulse duration. The lower simulated peak power can be ascribed to the low simulated

efficiency at 1kHz repetition rate. In figure 4.18b the simulated slope efficiencies are compared to the experiments. Overall the simulated efficiencies are too high for high repetition rates. This behavior, however, has already been observed for the simulation of CW-amplification for similar seed average powers. Generally the model supports the potential of this thulium rod for high peak power generation. Further model improvements are required in order to use this simulation tool for the optimization of the MOPA design.



(a) Simulated peak power evolution with pump power for 1kHz, 10kHz and 20kHz with 6.5ns and 100ns, respectively.

(b) Simulated and experimental slope efficiencies for different seed peak powers.

Figure 4.18: Simulated maximum peak powers and slope efficiencies

The simulated pulse shape and spectrum at 700kW peak power are depicted in figure 4.19 and are generally in good agreement with the experiments (section 3.5). The temporal pulse center is shifted and the pulse duration is slightly increased by 0.12ns compared to the input pulse. The pulse energy was determined by integration and is in agreement with the sum of extracted energy (4.15b) and the input pulse energy. The pulse spectrum shows a 50dB spectral power difference between ASE and signal wavelength. The experiment indicated that the spectral power difference between ASE and signal wavelength is at least 35dB. However, in this simulation it was assumed

that no ASE was included in the input seed signal. Thus, the model might underestimate the actual ASE content.

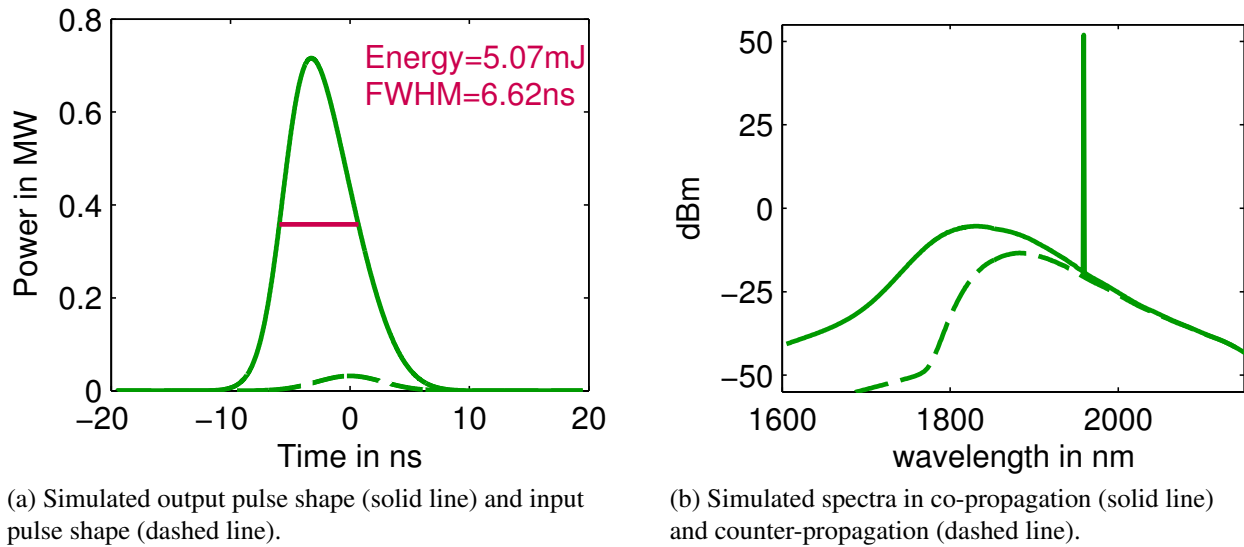


Figure 4.19: Simulated pulse shape and spectrum at 100W pump power, 1kHz and $> 700kW$ peak power.

The model for pulsed amplification is intended to provide a tool for the optimization of the MOPA design and it can be used as such for qualitative investigations of the amplifier performance. However, quantitative accuracy with excellent agreement to the experimental results has not yet been achieved. As mentioned before, the main reasons are the lack of knowledge about influential parameters in the rate equations, namely the exact cross sections, non-radiative and radiative decay rates, cross relaxation rates and their temperature dependence.

Regardless of the above mentioned obstacles a first demonstration, of how the model could be used for amplifier optimization, is provided in figure 4.20. The peak powers were simulated for pump powers well beyond 100W for three different seed inputs. The first seed input is, with 1kHz, 6.5ns and 40kW peak power, similar to the seed settings used for the experiments in section 3.5. ASE builds up drastically for pump powers beyond 120W and the energy extraction starts to

saturate. Similar behavior is observed when the input seed power is doubled. In this case peak powers $> 1\text{MW}$ were simulated for pump powers beyond 120W. However, saturation starts at similar pump power levels. The generation of ASE is efficiently reduced for larger repetition rates. Thus, for 40kW seed peak power and a repetition rate of 2kHz similar output peak powers can be achieved, while the ASE content is reduced. The main challenge is, however, to reach similar peak powers at twice the repetition rate in the preamplifier. In conclusion the repetition rate of 1kHz was appropriate for the generation of the highest peak power with the available seed power and a maximum available pump of 100W. Higher pump powers can not be used to scale the peak power in this system, if the seed peak power is not increased as well. Average power scaling with higher repetition rates is generally possible.

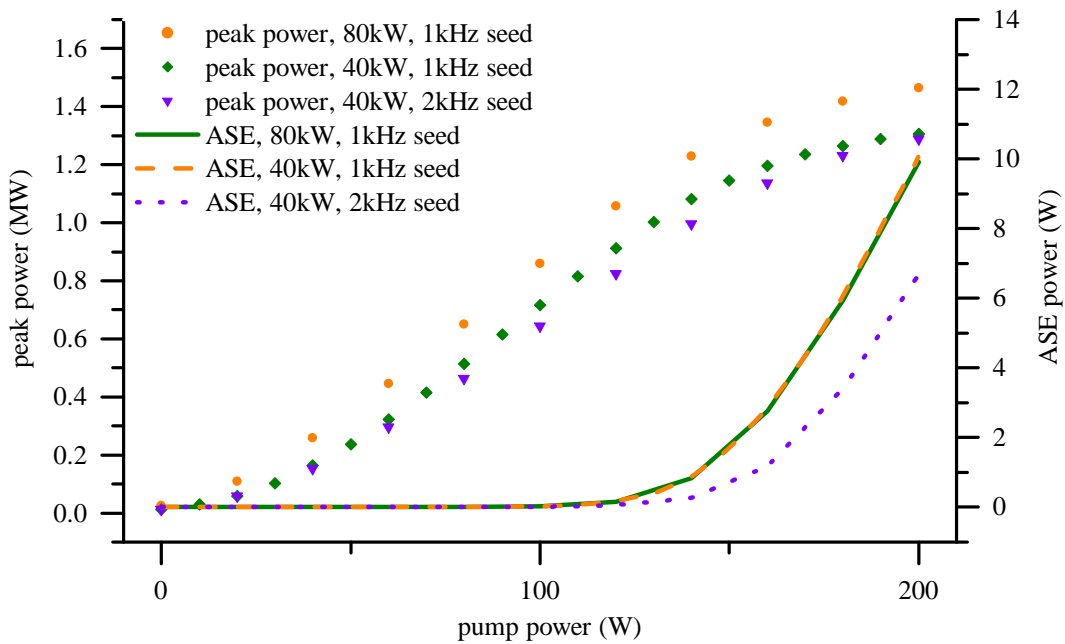


Figure 4.20: Comparison of ASE power and peak power evolution with pump power for different seed conditions.

4.6 Summary of the simulation results

In this work an algorithm for pulsed fiber amplification, first published by M. Eichhorn for thulium doped fluoride glass fibers [62], was successfully implemented in a Matlab code starting from the general rate equations for thulium doped silica fibers. The model includes the full spectral information of the laser transition as well as the generation of ASE and is capable of simulating CW-amplification and transient behavior of pulsed amplification. Cross relaxation and energy upconversion processes have been taken into account, although the exact degree of clustering in the simulated fiber is not known.

The model was first tested in CW-operation for rodB and compared to the experimental findings in section 3.4.4. The CW investigation revealed that this initial model predicts larger slope efficiencies and output powers than the experiments. Various reasons for this observation have been identified. Generally the exact emission and absorption cross sections, non-radiative and radiative decay times are not known for the simulated fiber. This and the relatively high temperatures in the fiber core due to the short absorption length and high quantum defect lead to inaccuracy in the model. Although cross relaxation processes were included in the model, the simulated slope efficiencies were significantly smaller than 40%. This indicates, that higher doping concentrations and modifications of the glass chemistry are required in order to achieve better efficiency.

The radial temperature profile along the fiber was estimated with a mostly analytical model that was first presented by J. Limpert et al. [84]. It was found that the temperatures in the core might reach $1000K$ when insufficiently cooled at pump powers in the range of 250W. It was shown that the radial temperature gradient does not change for different cooling conditions, while the absolute temperature in the core is significantly decreased with water cooling.

In order to improve the first version of the model, the temperature dependence of the emission cross section was implemented under the assumption that the absorption cross section remains the same for all temperatures. This reduced the modeled efficiencies and final output powers leading to better agreement with the experiments.

The improved model was then utilized for simulation of pulsed amplification in rodB with the same repetition rates and pulse durations used for the experiments in section 3.5. The results showed qualitative agreement with the experiments. Quantitative deviations from the experimental results are similar to the observed differences between CW-simulation and CW-amplification experiments. The pulsed operation leads to an additional drop of efficiency, especially for short pulse duration and small repetition rate.

A first demonstration, of how the model can be used for the optimization of the amplifier, was provided in the last section. The simulation revealed, that energy extraction is clearly limited by buildup of ASE for pump powers beyond 120W and 1kHz repetition rate. It was shown that an increase of repetition rate to 2kHz can reduce the amount of ASE without reducing peak powers.

CHAPTER 5: SUMMARY AND OUTLOOK

In this work the utility of novel thulium doped PCF rods for CW-lasing, CW-amplification and pulsed amplification was investigated in detail. For the first time in thulium, the rod-type PCF design has proven to be an excellent tool for the generation of high average and high peak powers.

More than 20W average power are feasible in CW-lasing configuration at 100W pump power and $< 27.8\%$ slope efficiency with excellent beam quality of $M^2 < 1.3$. The broad emission spectrum of thulium doped silica enabled very broad laser wavelength tuning from 1810nm to 1990nm. The amplification characteristics in CW operation were investigated for various seed conditions. A maximum of 52W average power was achieved at 6W seed power and 250W pump power, while slope efficiencies $< 25\%$ were observed to be lower than in CW-lasing configuration. The beam quality was excellent up to an output power of $\approx 40W$, before thermal effects lead to degradation of beam quality and drop of efficiency. Strong thermal lensing was identified as the main cause of beam degradation, while the reduction of efficiency might be related to transverse hole burning.

Pulsed amplification with the rod type PCF design was investigated for selected repetition rates and pulse durations. The experiments showed that the slope efficiency is already significantly decreased to $\approx 17\%$ at pulse repetition rates of 20kHz and 100ns pulses. The efficiency is reduced even further to $\approx 9\%$ at 1kHz repetition rate and 6.5ns pulse duration. Although the achievable average power is limited at low repetition rates and pulse durations, the extracted peak power can be maximized. In this work a pulse energy of $6.4mJ$ with a record output peak power of $> 800kW$ was generated at 6.5ns pulse duration and 1kHz repetition rate. This demonstration represents another significant milestone in the development of high power thulium based fiber laser systems. In comparison to previous achievements in the field (figure 5.1), this result represents an impressive increase of peak power by a factor of > 5 and the achievable peak power level in thulium doped

fiber lasers is now similar to the performance of ytterbium based systems.

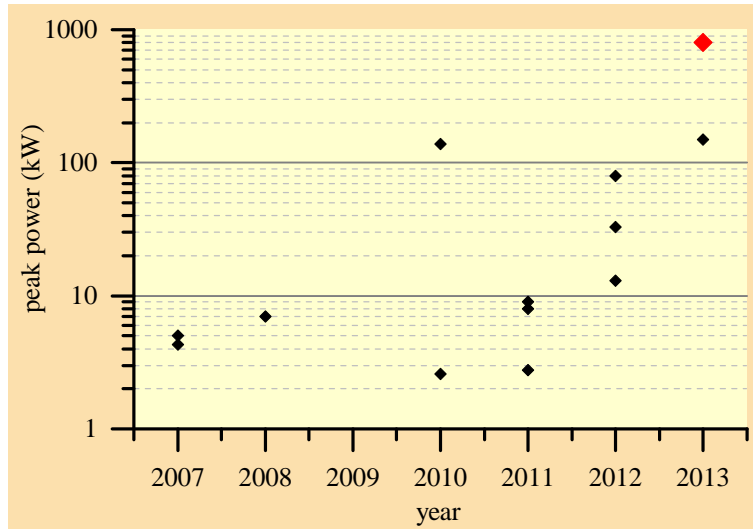


Figure 5.1: Peak power evolution over the past 6 years in thulium based fiber lasers with nanosecond pulse duration. In this work MW-level peak power was generated for the first time in thulium based fiber lasers (red marker) [6, 7, 8, 9, 10, 11, 12, 13, 14, 15, 4].

A computer program for the simulation of the transient behavior of pulsed amplification in thulium fibers has been implemented in Matlab. This model includes the full spectral information of the laser transition as well as the generation of ASE. In addition cross relaxation and energy upconversion have been taken into account.

The program was first used for the simulation of CW-amplification in the PCF rod design. Although the results were qualitatively similar to the experiments, the quantitative accuracy does not match in terms of final output power and slope efficiency. An analytic model was developed and used to describe the radial temperature evolution along the fiber. The large quantum defect in thulium causes significant heating in the core region of the PCF rod with temperatures up to 1000K at 250W pump power. The pulsed amplification model was enhanced, to my knowledge for the first time, by introducing a temperature dependent change of the emission cross section. This enhancement lead to more accurate simulation results. The remaining dissimilarity to the ex-

periments could be reduced, if more accurate input parameters, such as cross sections, decay and cross relaxation rates, were known for the modeled fiber rod. The model can be enhanced further by introducing temperature dependencies for multiple parameters. Accordingly, this requires more testing and experimental investigation of the fiber rod.

The absence of roll off and nonlinear effects in the experiments show the potential of this PCF rod design to generate even higher peak powers. Better optimization of the entire MOPA system is required to achieve this goal and the rod needs to be end-capped to prevent facet damage. The transient model can be utilized as a tool for the optimization of the whole MOPA system. Further improvements of the model are necessary and accurate, temperature dependent absorption cross section measurements are required. The optimization of fiber lengths, seed conditions and number of amplification stages are only some examples of what could be studied with the model. Moreover the model could be used to explore the option of pulsed pumping and its effect on ASE content at low repetition rates.

In conclusion this work has two major impacts, namely the feasibility of thulium fiber lasers for pulsed amplification to MW-level peak power and an improved transient model of pulsed amplification that includes temperature effects. The MW-level peak power result exemplifies the potential of thulium fiber lasers to supersede ytterbium based systems for very high peak power generation in the future.

LIST OF REFERENCES

- [1] C. C. Willis, L. Shah, M. Baudele, P. Kadwani, T. S. McComb, R. A. Sims, V. Sudesh, and M. Richardson. High-energy Q-switched Tm^{3+} -doped polarization maintaining silica fiber laser. *SPIE Proceedings*, 7580:758003, 2010.
- [2] W. Shi, E. B. Petersen, D. T. Nguyen, Z. Yao, A. Chavez-Pirson, N. Peyghambarian, and J. Yu. $220\mu J$ monolithic single-frequency Q-switched fiber laser at $2\mu m$ by using highly Tm-doped germanate fibers. *Optics Letters*, 36:3575–3577, 2011.
- [3] M. Eichhorn. Development of a high-pulse-energy Q-switched Tm-doped double-clad fluoride fiber laser and its application to the pumping of mid-IR lasers. *Optics Letters*, 32:1056–1058, 2007.
- [4] M. Eichhorn and S. D. Jackson. High-pulse-energy actively Q-switched Tm^{3+} -doped silica $2\mu m$ fiber laser pumped at $792nm$. *Optics Letters*, 32:2780–2782, 2007.
- [5] M. Eichhorn and S. D. Jackson. High-pulse-energy, actively Q-switched Tm^{3+}, Ho^{3+} -codoped silica $2\mu m$ fiber laser. *Optics Letters*, 33:1044–1046, 2008.
- [6] J. Ding, B. Samsona, A. Cartera, C. Wang, and K. Tankalaa. A Monolithic Thulium Doped Single Mode Fiber Laser with 1.5ns Pulsewidth and 8kW Peak Power. *Nufern*, 2008.
- [7] P. Kadwani, N. Modsching, A. Sims, L. Leick, J. Broeng, L. Shah, and M. Richardson. Q-switched thulium-doped photonic crystal fiber laser. *Optics Letters*, 37:1664–1666, 2012.
- [8] P. Kadwani, A. Sims, L. Leick, J. Broeng, L. Shah, and M. Richardson. 1 mJ Pulse Energies in Tm-doped Photonic Crystal Fiber. *Specialty Optical Fibers paper, Colorado*, SW2F.3, 2012.
- [9] Q. Fang, W. Shi, K. Kieu, E. Petersen, A. Chavez-Pirson, and N. Peyghambarian. High power and high energy monolithic single frequency $2\mu m$ nanosecond pulsed fiber laser by using large core Tm-doped germanate fibers: experiment and modeling. *Optics Express*, 20:16410–16420, 2012.
- [10] Y. Tang, L. Xu, Y. Yang, and J. Xu. High-power gain-switched Tm^{3+} -doped fiber laser. *Optics Express*, 18:22964–22972, 2010.
- [11] F. Stutzki, F. Jansen, C. Jauregui, J. Limpert, and A. Tünnermann. 2.4 mJ, 33 W Q-switched Tm-doped fiber laser with near diffraction-limited beam quality. *Optics Letters*, 38:97–99, 2013.
- [12] Traeger (editor). *Handbook of Lasers and Optics*. Springer, 2007.
- [13] W. Koechner. *Solid-State Laser Engineering*. Springer, 1999.

- [14] P. Russel. Photonic Crystal Fibers. *Applied Physics*, 299:358–362, 2003.
- [15] R. W. Boyd. *Nonlinear Optics 3rd edition*. AP, 2007.
- [16] A. V. Smith and B. T. Do. Bulk and surface laser damage of silica by picosecond and nanosecond pulses at 1064 nm. *Applied Optics*, 47:4812–4832, 2008.
- [17] NKT Photonics. Damage threshold of fiber facets. *Application note*, 1:1–4, 2012.
- [18] F. Jansen, F. Stutzki, H. J. Otto, T. Eidam, A. Liem, C. Jauregui, J. Limpert, and A. Tünnermann. Thermally induced waveguide changes in active fibers. *Optics Express*, 20:3997–4008, 2012.
- [19] T. Eidam, C. Wirth, C. Jauregui, F. Stutzki, F. Jansen, H. J. Otto, O. Schmidt, T. Schreiber, J. Limpert, and A. Tünnermann. Experimental observations of the threshold-like onset of mode instabilities in high power fiber amplifiers. *Optics Express*, 19:13218–13224, 2011.
- [20] S. D. Jackson. The spectroscopic and energy transfer characteristics of the rare earth ions used for silicate glass fibre lasers operating in the shortwave infrared. *Laser and Photonics Rev.*, 3:466–482, 2009.
- [21] P. Wilcox. Comprehensive model of double cladding Thulium-doped fibers pumped at 795 nm. *SPIE Photonics West LASE, San Jose*, 2009.
- [22] G. Turri, V. Sudesh, M. Richardson, M. Bass, A. Toncelli, and M. Tonelli. Temperature-dependent spectroscopic properties of Tm^{3+} in germanate, silica, and phosphate glass: A comparative study. *Journal of Applied Physics*, 103:093104, 2008.
- [23] C. Jollivet and A. Schülzgen. Mode analysis of thulium doped pcf rods. Fiberlaser group, CREOL, UCF.
- [24] C. Gaida, P. Kadwani, L. Leick, J. Broeng, L. Shah, and M. Richardson. CW-lasing and amplification in Tm^{3+} -doped photonic crystal fiber rod. *Optics Letters*, 37:4513–4515, 2012.
- [25] C. Gaida, M. Gebhardt, P. Kadwani, L. Leick, J. Broeng, L. Shah, and M. Richardson. Amplification of nanosecond pulses to megawatt peak power levels in Tm^{3+} -doped photonic crystal fiber rod. *Optics Letters*, 38:691–693, 2012.
- [26] J. Limpert, T. Schreiber, A. Liem, S. Nolte, H. Zellmer, T. Peschel, V. Guyenot, and A. Tünnermann. Thermo-optical properties of air-clad photonic crystal fiber lasers in high power operation. *Optics Express*, 11:2982–2990, 2003.
- [27] S. D. Jackson and T. A. King. Theoretical Modeling of Tm-Doped Silica Fiber Lasers. *Journal of Lightwave Technology*, 17:948–956, 1999.
- [28] T. S. McComb. *Power Scaling of Large Mode Area Thulium Fiber Lasers in various spectral and temporal Regimes*. PhD thesis, CREOL, the College of Optics and Photonics, 2009.

- [29] D. J. Richardson, J. Nilsson, and W. A. Clarkson. High power fiber lasers: current status and future perspectives. *Optical Society of America*, 27:B63–B92, 2010.
- [30] J. Limpert, A. Tünnermann, and T. Schreiber. Fiber lasers and amplifiers: an ultrafast performance evolution. *Appl. Opt.*, 49:25, 2010.
- [31] C. Brooks and F. Di Teodoro. Multimegawatt peak-power, single-transverse-mode operation of a $100\mu\text{m}$ core diameter, Yb-doped rodlike photonic crystal fiber amplifier. *Applied Physics Letters*, 89:111119, 2006.
- [32] P. Kadwani. *Pulsed Tm-fiber Laser for Mid-IR Generation*. PhD thesis, CREOL, the College of Optics and Photonics, 2013.
- [33] R. Paschotta. Encyclopedia of Laser Physics and Technology. URL: <http://www.rp-photonics.com>, Oktober 2011. Abgerufen am: 04.10.2011 17 : 15 Uhr.
- [34] H. Injeyan (editor), G. D. Goodno (editor), and F. D. Teodoro. *High Power Laser Handbook; Pulsed Fiber Lasers*. McGraw-Hill Companies, 2011.
- [35] A. Ghatak and K. Thyagarajan. *Introduction to Fiber Optics*. Cambridge University Press, 1998.
- [36] R. W. Berdine R. A. Motes. *Introduction to High-Power Fiber Lasers*. Directed Energy Professional Society, 2009.
- [37] F. Jansen, F. Stutzki, C. Jauregui, J. Limpert, and A. Tünnermann. Avoided crossings in photonic crystal fibers. *Optics Express*, 19:13578–13589, 2011.
- [38] M. E. Fermann. Single-mode excitation of multimode fibers with ultrashort pulses. *Optics Letters*, 23:52–54, 1998.
- [39] P. S. J. Russell. Photonic Crystal Fiber. *Private Papers*, 1991.
- [40] C. M. Bowden, J. P. Dowling, and H. O. Everitt. Feature on development and applications of materials exhibiting photonic bandgaps. *Optical Society of America*, 10:279–359, 1993.
- [41] J. C. Knight, T. A. Birks, P. S. J. Russell, and D. M. Atkin. All-silica single-mode optical fiber with photonic crystal cladding. *Optics Letters*, 21:1547–1549, 1996.
- [42] J. Limpert, N. Deguil-Robin, I. Manek-Hönninger, F. Salin, F. Röser, A. Liem, T. Schreiber, S. Nolte, H. Zellmer, A. Tünnermann, J. Broeng, A. Petersson, and C. Jakobsen. High-power rod-type photonic crystal fiber laser. *Optics Express*, 13:1055–1058, 2005.
- [43] L. Dong and X. Peng and J. Li. Leakage channel optical fibers with large effective area. *Optical Society of America*, 24:1689–1697, 2007.
- [44] L. Dong, T. Wu, H. A. McKay, L. Fu, J. Li, and H. G. Winful. All-Glass Large-Core Leakage Channel Fibers. *IEEE Journal of selected topics in Quantum Electronics*, 15:47–53, 2009.

- [45] J. Limpert, F. Stutzki, F. Jansen, H. J. Otto, T. Eidam, C. Jauregui, and A. Tünnermann. Yb-doped large-pitch fibres: effective single-mode operation based on higher-order mode delocalisation. *Light: Science & Applications*, npg, 1, e8:doi:10.1038/lisa.2012.8, 2012.
- [46] E. Snitzer. Double-clad, Offset Core Nd Fiber Laser. In *New Orleans, post-deadline paper PD5*, 1988.
- [47] H. Injeyan (editor), G. D. Goodno (editor), J. Limpert, and A. Tünnermann. *High Power Laser Handbook; High-Power Ultrafast Fiber Laser Systems*. McGraw-Hill Companies, 2011.
- [48] E. v. Stryland. *Nonlinear Optics*. CREOL the College of Optics and Photonics, 2012.
- [49] G. P. Agrawal. *Nonlinear Fiber Optics*. Academic Press, 2001.
- [50] Y. Namihara, M. Miyata, and N. Tanahashi. Nonlinear coefficient measurements for dispersion shifted fibres using self-phase modulation method at $1.55 \mu\text{m}$. *Electron Letters*, 30:1171–1172, 1994.
- [51] R.H. Stolen. Nonlinear in Fiber Transmission. *IEEE*, 68:1232–1236, 1980.
- [52] B. C. Stuart, M. D. Feit, S. Herman, A. M. Rubenchick, B. W. Shore, and M. D. Perry. Nanosecond-to-femtosecond laser-induced breakdown in dielectrics. *Phys. Rev.*, 53:1749–1761, 1996.
- [53] L. D. Merkle, N. Koumvakalis, and M. Bass. Laser-induced bulk damage in SiO_2 at 1.064, 0.532, and $0.355 \mu\text{m}$. *Appl. Phys.*, 55:772–775, 1984.
- [54] M. J. Soileau, W. E. Williams, N. Mansour, and E. W. Van Stryland. Laser-induced damage and the role of selffocusing. *Opt. Eng.*, 28:1133–1144, 1989.
- [55] A.C. Tien, S. Backus, H. Kapteyn, M. Murnane, and G. Mourou. Short-pulse laser damage in transparent materials as a function of pulse duration. *Phys. Rev.*, 82:3883–3886, 1999.
- [56] E. W. v. Stryland, M. J. Soileau, A. L. Smirl, and W. E. Williams. Pulse-width and focal-volume dependence of laser-induced breakdown. *Phys. Rev.*, 23:2144–2151, 1981.
- [57] B. C. Stuart, M. D. Feit, A. M. Rubenchik, B. W. Shore, and M. D. Perry. Laser-induced damage in dielectrics with nanosecond to subpicosecond pulses. *Phys. Rev.*, 74:2248–2251, 1995.
- [58] C. Jauregui, T. Eidam, H. J. Otto, F. Stutzki, F. Jansen, J. Limpert, and A. Tünnermann. Physical origin of mode instabilities in high power fiber laser systems. *Optics Express*, 20:12912–12925, 2012.
- [59] H. J. Otto, F. Jansen, F. Stutzki, C. Jauregui, J. Limpert, and A. Tünnermann. Mitigation of mode instabilities by dynamic excitation of fiber modes. In *Europhoton*, 2012.

- [60] R. Paschotta. Lifetime quenching in Yb-doped fibres. *Optic. Commun.*, 136:375, 1997.
- [61] J. J. Koponen. Measuring photodarkening from single-mode ytterbium doped silica fibers. *Optics Express*, 24:11539, 2006.
- [62] J. Jasapara. Effect of heat and H₂ gas on the photo-darkening of Yb³⁺ fibers. *Optical Fiber Communications*, 2006.
- [63] I. Manek-Hönniger. Photodarkening and photobleaching of an ytterbium-doped silica double-clad LMA fiber. *Optics Express*, 15:1606, 2007.
- [64] S. D. Jackson. Cross relaxation and energy transfer upconversion processes relevant to the functioning of 2 μm Tm³⁺-doped silica fibre lasers. *Optics Communications*, 230:197–203, 2004.
- [65] S. D. Jackson and S. Mossman. Efficiency dependence on the Tm³⁺ and Al³⁺ concentrations for Tm³⁺-doped silica double-clad fiber lasers. *Applied Optics*, 42:2702–2707, 2003.
- [66] D. A. Simpson, G. W. Baxter, S. F. Collins, W. E. K. Gibbs, W. Blanc, B. Dussardier, and G. Monnom. Energy transfer up-conversion in Tm³⁺-doped silica fiber. *Journal of Non-Crystalline Solids*, 352:136–141, 2006.
- [67] M. Eichhorn. Numerical Modeling of Tm-Doped Double-Clad Fluoride Fiber Amplifiers. *IEEE Journal of Quantum Electronics*, 41:1574–1581, 2005.
- [68] G. Rustad and K. Stenersen. Modeling of Laser-Pumped Tm and Ho Lasers Accounting for Upconversion and Ground-State depletion. *IEEE Journal of Quantum Electronics*, 32:1645–1656, 1996.
- [69] T. Ehrenreich, R. Leveille, I. Majid, K. Tankala, G. Rines, and P. Moulton. 1kW, All-glass Tm: fiber laser. *SPIE Photonics West LASE*, 2010.
- [70] J. Limpert, J. Rothhardt, S. Hädrich, S. Demmler, M. Krebs, and A. Tünnermann. Fiber Laser Pumped MHz High Repetition Rate Few-cycle OPCPA System. *FiO/LS Technical Digest, OSA*, 2012.
- [71] J. Yu et. al. Advanced 2 – μm solid-state laser for wind and CO₂ lidar applications. *SPIE Proceedings*, 2006.
- [72] V. Lemberg, D. Rozhetskin, and C. Jadczak. Medium-power Tissue Ablation using 1940 nm Thulium Fiber Laser. *Biomedical Optics, OSA Technical Digest (CD)*, paper BTuF4, 2008.
- [73] N. Modsching, P. Kadwani, A. Sims, L. Leick, J. Broeng, L. Shah, and M. Richardson. Lasing in thulium-doped polarizing photonic crystal fiber. *Optics Letters*, 36:3873–3875, 2011.
- [74] W. A. Clarkson, N. P. Barnes, P. W. Turner, J. Nilsson, and D. C. Hanna. High-power cladding-pumped Tm-doped silica fiber laser with wavelength tuning from 1860 to 2090 nm. *Optics Letters*, 27:1989–1991, 2002.

- [75] T. S. McComb, R. A. Sims, C. C. Willis, P. Kadwani, V. Sudesh, L. Shah, and M. Richardson. High-power widely tunable thulium fiber lasers. *Applied Optics*, 49:6236–6242, 2010.
- [76] F. Jansen, F. Stutzki, C. Jauregui, J. Limpert, and A. Tünnermann. High-power very large mode-area thulium-doped fiber laser. *Optics Letters*, 37:4546–4548, 2012.
- [77] C. Gaida, M. Gedhardt, P. Kadwani, L. Leick, J. Broeng, L. Shah, and M. Richardson. Peak power scaling in Tm doped fiber laser to MW-level. *SPIE Photonics West LASE*, pages 8601–107, 2013.
- [78] L. Shah, R. A. Sims, P. Kadwani, C.C. Willis, J. B. Bradford, A. Pung, M. K. Poutous, E. G. Johnson, and M. Richardson. Integrated Tm: fiber MOPA with polarized output and narrow linewidth with 100 W average power. *Optics Express*, 20:20558–20563, 2012.
- [79] G. D. Goodno, L. D. Book, and J. E. Rothenberg. Low-phase-noise, single-frequency, single-mode 608 W thulium fiber amplifier. *Optics Letters*, 34:1204–1206, 2009.
- [80] P. Kadwani, R. A. Sims, L. Leick, J. Broeng, L. Shah, and M. Richardson. High Power Operation of Tm-doped Photonic Crystal Fiber Laser Systems. *DEPS*, 2012.
- [81] O. Schmidt, J. Rothhardt, F. Röser, S. Linke, T. Schreiber, K. Rademaker, J. Limpert, S. Ermeneux, P. Yvernault, F. Salin, and A. Tünnermann. Millijoule pulse energy Q-switched short-length fiber laser. *Optics Letters*, 32:1551–1553, 2007.
- [82] F. Stutzki, F. Jansen, A. Liem, C. Jauregui, J. Limpert, and A. Tünnermann. 26 mJ, 130 W Q-switched fiber-laser system. *Optics Letters*, 37:1073–1075, 2012.
- [83] H. Lü, P. Zhou, X. Wang, and Z. Jiang. Space-propagation model of Tm-doped fiber laser. *J. Opt. Soc. Am. A*, 29:2337–2343, 2012.
- [84] W. H. Press, S. A. Teukolsky, W. T. Vetterling, and B. P. Flannery. *Numerical Recipes in C; The Art of scientific Computing 2nd Edition*. Cambridge University Press, 2002.